Efficient Numerical Techniques for Multiscale Modeling of Thermally Driven Gas Flows with Application to Thermal Sensing Atomic Force Microscopy

by Nathan D. Masters

A Thesis
Presented to
The Academic Faculty

by

Nathan D. Masters

In Partial Fulfillment
of the Requirements for the Degree
Doctor of Philosophy

Woodruff School of Mechanical Engineering
Georgia Institute of Technology
August, 2006

Efficient Numerical Techniques for Multiscale Modeling of Thermally Driven Gas Flows with Application to Thermal Sensing Atomic Force Microscopy

by Nathan D. Masters

Approved by:

Professor Wenjing Ye, Committee Chair	Professor Levent Degertekin Mechanical Engineering
Professor Wenjing Ye Mechanical Engineering, Advisor	Professor Elisa Riedo Physics
Professor William P. King Mechanical Engineering	Professor John Pelesko Mathematics (University of Delaware)
Professor Zhuomin Zhang Mechanical Engineering	

Date Approved: 28 June 2006

to Emily

ACKNOWLEDGEMENTS

I would like to thank my advisor, Dr. Wenjing Ye, for a challenging and rewarding research experience. Kyle Cavin, to whom I am deeply indebted for hours of coding, conversations, and generally going above and beyond as a volunteer researcher. I must thank those who have blazed the trail that I hope to have improved: Drs. Graeme Bird, Jing Fan, Ching Shen, Quanhua Sun, and Iain Boyd. I am so grateful to my wife who is so patient and supportive and to my boys, Riley and Jarom, who have all helped me so much and provided joy and purpose in all that I do. Finally, I must thank my Creator, for the talents, abilities, inspiration, and grace, with which I have been greatly blessed.

This work has been funded by The Woodruff School of Mechanical Engineering, Georgia Institute of Technology and the National Science Foundation.

TABLE OF CONTENTS

LIST OF TABLES

LIST OF FIGURES

LIST OF SYMBOLS OR ABBREVIATIONS

AFM	Atomic Force Microscope.
BEM	Boundary Element Method.
BGK	Bhatnagar, Gross & Krook model for the collision operator of the Boltzmann Transport Equation.
BTE	Boltzmann Transport Equation.
DSMC	Direct Simulation Monte Carlo.
FEM	Finite Element Method.
FVM	Finite Volume Method, a conservative numerical method commonly used for solving CFD problems.
IP-DSMC	Information Preserving DSMC.
MD	Molecular Dynamics. A deterministic modeling technique for simulation of molecules suitable for solids, liquids, and gases.
OSIP-DSMC	Octant Splitting Information Preserving DSMC.
PRN	Pseudo Random Number.
TSAFM	Thermal Sensing Atomic Force Microscopy.
α	Accommodation coefficient which is a measure of how much a surface affects particles that interact with it. $\alpha = 1$ is fully accommodating, or diffuse, and $\alpha = 0$ is specular.
β	Reciprocal of the most probable molecular speed in an equilibrium gas, $\beta = (2RT)^{-1/2}$.
χ	Pressure ratio $\chi = p_1/p_2$ in a thermal transpiration or Knudsen force system. Also the deflection angle, or angle between the pre- and post-collision relative velocities of a collision pair.
δ	Intermolecular spacing; Kronecker delta; Dirac delta.
Γ	Expansion used in the Chapman-Enskog distribution. Also the gamma function, $\Gamma(j) = \int_0^\infty x^{j-1} \exp(-x)\, \mathrm{d}x$.
γ	Ratio of specific heats, $\gamma = c_p/c_v$.

λ	Mean free path, or distance traveled between intermolecular collisions.
Ω	Control or computational cell volume, or more generally a computational domain. Also units of electrical resistance, Ohm.
ρ	Mass density.
ρ_e	Electrical resistivity, or resistance per unit length ($\Omega - cm$).
$\boldsymbol{c}_0$	Macroscopic flow velocity of the gas.
c_{mp}	Most probable velocity of particles within distribution at temperature T. For an equilibrium distribution $c_{mp} = \sqrt{2RT}$.
$\boldsymbol{c}'$	Thermal or peculiar velocity, velocity components relative to the stream velocity, $\boldsymbol{c}' = \boldsymbol{c} - \boldsymbol{c}_0$.
$\boldsymbol{c}'''$	Thermal velocity relative to the IP velocity $\boldsymbol{V}$, *i.e.*, $\boldsymbol{c}''' = \boldsymbol{c} - \boldsymbol{V}$.
c_v	Specific heat at constant volume.
d	Molecular diameter.
e	Internal energy associated with vibrational and rotational energy.
f_0	Equilibrium or Maxwellian distribution, $f_0(\boldsymbol{c}, \boldsymbol{x}, t) = \frac{\beta^3}{\pi^{3/2}} \exp -\beta^2 c'^2$.
f	Velocity distribution function specifying the probability of finding a particle at a given location with a given velocity.
$\boldsymbol{F}$	External or body forces.
F_N	Effective Number, *i.e.* the number of real molecules represented by each DSMC molecule.
g	Separation or air gap between heated bodies.
k_B	Boltzmann constant, $k_B = m\,R = 1.380650524 \times 10^{-23}$ J/K.
Kn	Knudsen Number is the ratio of the mean free path λ to some characteristic length L, i.e., Kn = λ/L.
L	Characteristic Length of a flow. This may be in terms of geometry (length, separation, etc.) or local gradients.
m	Molecular Mass (66.3×10^{-27} kg for Argon).

Ma	Mach Number, Ma = $\|c\|/a$, where a is the speed of sound.
n	Number density.
p_{ij}	Pressure Tensor (indicial notation).
p	Scalar pressure.
q_i	Heat flux vector (indicial notation).
R	Specific gas constant $R = \mathcal{R}/(m\mathcal{N})$.
$\mathcal{R}_u$	Uniformly distributed random fraction between 0 and 1.
$\mathcal{R}_n$	Normally distributed random fraction with mean of 0 and standard deviation of 1.
R_T	Temperature dependent electrical resistance.
T	Kinetic Temperature.
$\boldsymbol{V}$	IP velocity.
$\mathcal{V}$	Electrical potential or voltage.

SUMMARY

The modeling of Micro- and NanoElectroMechanical Systems (MEMS and NEMS) requires new computational techniques that can deal efficiently with geometric complexity and scale dependent effects that may arise. With reduced feature sizes comes increasing coupling of physical phenomena and increasingly noncontinuum behavior, often requiring models based on molecular descriptions and/or first principles. Furthermore, noncontinuum effects are often localized to small regions of (relatively) large systems—precluding the global application of microscale models due to computational expense. Multiscale modeling couples efficient continuum solvers with detailed microscale models to providing accurate and efficient models of complete systems.

This thesis presents the development of multiscale modeling techniques for nonequilibrium microscale gas phase phenomena, especially thermally driven microflows. The three necessary components for multiscale modeling are 1. an efficient and accurate microscale model, 2. a similarly capable continuum models, and 3. a coupling scheme. The direct simulation Monte Carlo (DSMC) is one of the prevalent techniques for modeling rarefied gas dynamics. However, as a probabilistic particle based method it is (computationally) orders of magnitude more expensive than continuum solvers. Furthermore, microscale flows are typically low-speed, requiring extremely large numbers of samples to reduce statistical noise. A recent enhancement to the DSMC is the Information Preserving DSMC (IP-DSMC), which seeks to accelerate the solution by preserving certain macroscopic quantities within each simulation molecule. Transport of mass, momentum, and energy depends on particle motion and collisions and certain fluxal quantities. Although the IP-DSMC has performed well on a number of problems, it has been unable to adequately model flow

fields arising from certain nonequilibrium phenomena. Much of the research of this thesis focuses on improving the performance (speed and accuracy) of the microscale model and has resulted in the Octant Splitting Information Preserving DSMC (OSIP-DSMC) method for simulating low-speed and thermally driven rarefied gas flows. The method is able to recover previously unavailable information from the preserved quantities and the microscopic velocities allowing for efficient simulation of the flow fields induced by nonequilibrium systems, including effects such as thermal transpiration. The OSIP-DSMC provides an efficient method to explore rarefied gas transport phenomena which may lead to a greater understanding of these phenomena and new concepts for how these may be utilized in practical engineering systems. Multiscale modeling will be demonstrated utilizing the OSIP-DSMC for the microscale model and a 2D BEM solver for the continuum (heat transfer) model. Coupling will utilize a modified Alternating Schwarz coupling, wherein the microscopic and continuum models overlap within the continuum region. The solution of each is used in turn to generate the boundary conditions of the other, alternating until steady state is reached and the solutions within the overlapping region are found to be compatible within some tolerance. Thermal Sensing Atomic Force Microscopy (TSAFM) provides an interesting application for the modeling techniques developed in this thesis. TSAFM relies on gas phase heat transfer between heated cantilever probes and the scanned surface to determine the scan height, and thus the surface topography. Accurate models of the heat transfer phenomena are required to correctly interpret scan data. This thesis presents results demonstrating the effect of subcontinuum heat transfer on TSAFM operation and explores the mechanical effects of the Knudsen Force on the heated cantilevers.

CHAPTER I

INTRODUCTION

The past few decades have seen tremendous interest and growth in the area of MicroElectro-Mechanical Systems (MEMS). By leveraging the mature bulk and surface micromachining technologies developed for the large scale batch fabrication of microelectronics, it has become possible to economically fabricate microscale systems composed of electrical and mechanical subsystems. MEMS devices have become common in a number of consumer and industrial applications, including air bag sensors, optical displays, and a growing assortment of pressure and chemical sensors. The push for ever-decreasing size leads naturally to nanotechnology (and NanoElectroMechanical Systems or NEMS). As with MEMS, nanofabrication techniques may be additive: building up features from molecules or atoms (bottom-up), or subtractive: where small features are formed by removing material from larger ones (top-down), or a combination of both.

1.1 The Need For Multiscale Modeling

Despite the considerable activity in the development of microsystems, commercial growth has not met expectations. One factor inhibiting growth is the limited ability to perform system level modeling. At small length scales physical effects (mechanical, thermal, electrostatic, magnetic, etc.) are often tightly coupled, requiring highly detailed multiphysics solvers. Often analysis tools based on macroscale continuum models may be applied to microscale phenomena, but this is not generally the case. At small scales, not only can there be a breakdown of the continuum assumptions, but the manifestation or importance of many physical phenomena may change, *e.g.*, gravity, may be negligible at small scales, while macroscopically insignificant forces such as electrostatic and Van der Waal's forces

become dominant. So with scaling there are changes in the coupling, magnitude, and manner of physical phenomena.

Future growth in MEMS (and especially NEMS), will require accurate and efficient tools and techniques for system level modeling and design. A major obstacle is that non-continuum effects begin to be manifest at these small scales: conservation laws are always valid, but gradients (of strain, pressure, density, temperature, etc.) may become very sharp—to the point that their scale of length approaches the order of the mean free paths, or intermolecular/interatomic spacing. As such, the constitutive laws upon which conventional continuum methods (Navier-Stokes, Hooke's Law, etc.) are based are no longer applicable and methods based on the underlying molecular (or particle nature) must be used. At even smaller length scales, the concept of gradient may become meaningless in what may be truly discontinuous media.

In many micro/nanosystems, subcontinuum regions are often adjacent to (relatively) large regions where the continuum description remains valid. Global application of particle methods would be prohibitively expensive—with even a small problem capable of exhausting the *world's* computing power. This may be compounded further by complex system geometries and the poorly characterized properties of micro/nanomaterials. This work will seek to develop accurate and efficient multiscale modeling tools applicable to the modeling and design of systems involving micro/nanoscale gas phase thermal transport.

1.2 Thermal Sensing Atomic Force Microscopy (TSAFM)

One of the motivations for this research, and its focus on rarefied gas dynamics, is the Thermal Sensing Atomic Force Microscope (TSAFM). The TSAFM is one of many scanning probe microscopy variants and is closely related to conventional Atomic Force Microscopy (AFM). The AFM has become one of the key tools for the production and characterization of nanoscale features and devices. The AFM was introduced in 1986 by researchers at IBM [14] and generally consists of a micromachined cantilever beam with a very sharp tip

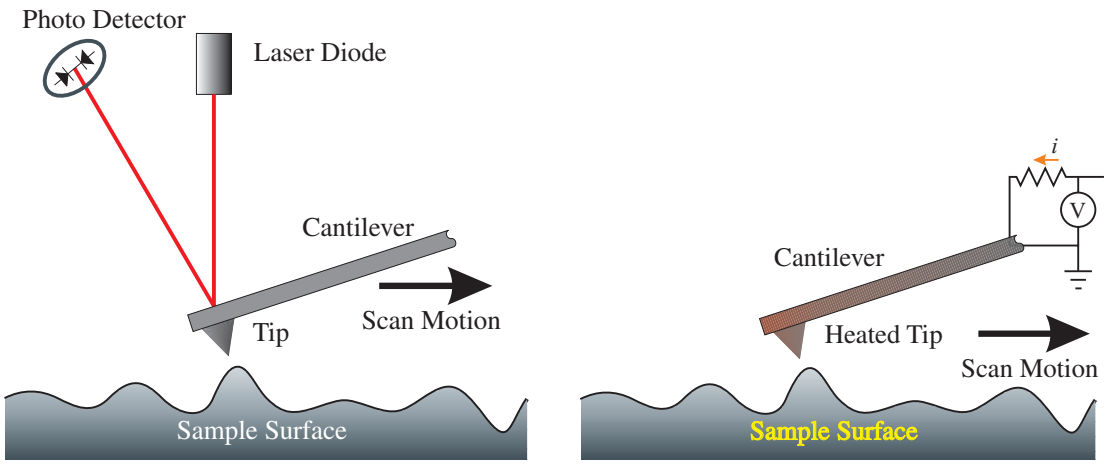

1-1(a): Atomic Force Microscope system

1-1(b): Thermal Sensing Atomic Force Microscope

Figure 1-1: Schematics of Conventional and Thermal Sensing Atomic Force Microscopy Systems

(radius of curvature on the order of 50 nm). The cantilever may be scanned, or rastered, across a sample in either contact or "tapping" mode, usually by means of a piezoelectric stage. As the tip interacts with the scanned surface topography the flexible AFM cantilever deflects. The prevalent scheme for detecting the deflection of the beam is optical; utilizing a laser emitter-detector pair [65] (see Figure 1-1(a)). Sub-nanometer three-dimensional topographic scans are possible with Atomic Force Microscopy—allowing individual atoms to be resolved (and even manipulated).

Thermal Sensing AFM builds on the principles of AFM but uses the heat transfer from a heated cantilever to sense the proximity to the substrate (see Figure 1-1(b)). As the heated cantilever is scanned across a nanofeatured surface, the gap between the cantilever and the substrate changes. If the gap becomes larger, the effective thermal resistance increases, resulting in a higher steady state temperature for a given heating power. Similarly, a smaller gap enhances heat transfer and reduces the steady state temperature. Heat generation and temperature measurement may be purely electrical and integrated in the device—eliminating the need for cumbersome optical detection of cantilever deflection

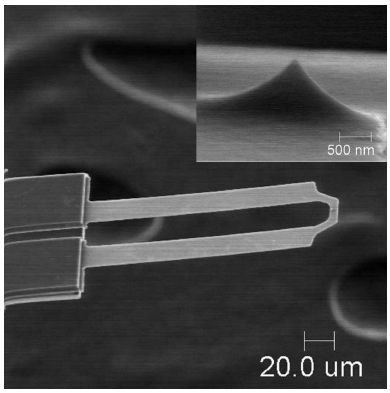

1-2(a): Scanning Electron Micrographs (SEM) of TSAFM cantilever and (inset) tips (Courtesy Dr. William King)

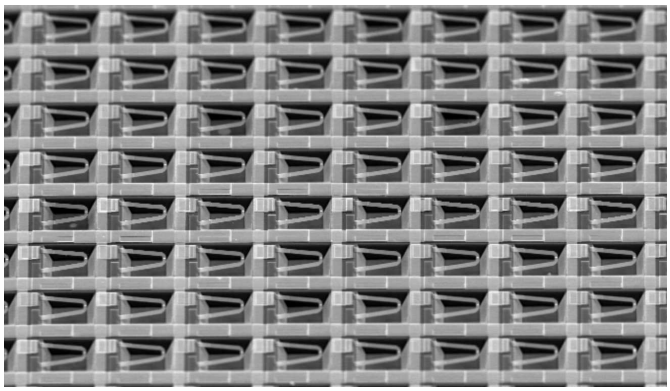

1-2(b): SEM of Millipede (TSAFM) cantilever array [46].

Figure 1-2: TSAFM Applications

and enabling the development of arrays of TSAFM cantilevers. Such arrays may provide increased scan rates and are being developed for high density data storage applications (see Figure 1-2(a) and 1-2(b)) [105, 53]. While the sharp tip is needed to establish contact with the scanned surface, previous studies have determined that the heat transfer through the tip contributes little to sensing and is only important in data writing, *i.e.*, melting and forming nano-indentations in a polymer substrate [8]. Sensing is accomplished as follows: *a*) a driving potential, V, is applied to the beam inducing a current and Joule heating in the cantilever; *b*) the system reaches steady state in terms of temperature, electrical resistance (temperature dependent), induced current, I, and heat flux (temperature and gap dependent); *c*) from the measured current, the temperature of the cantilever may be obtained, as well as the power input ($P = IV$); *d*) finally, models can be used to interpret the measured current to calculate the distance between the cantilever and the scanned surface.

The main heat transfer paths involved in TSAFM operation are illustrated in Figure 1-3: (1) solid state conduction along the cantilever, (2) gas phase conduction to the substrate, and (3) gas phase conduction to the environment.

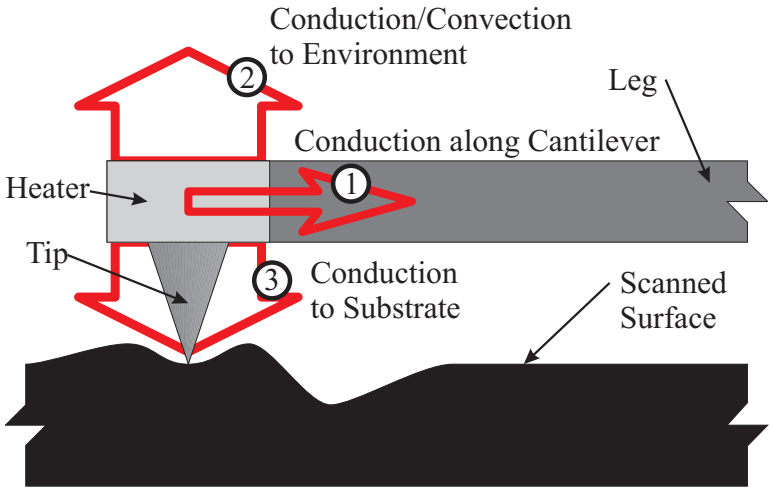

Figure 1-3: Schematic of Heat Transfer Paths in TSAFM.

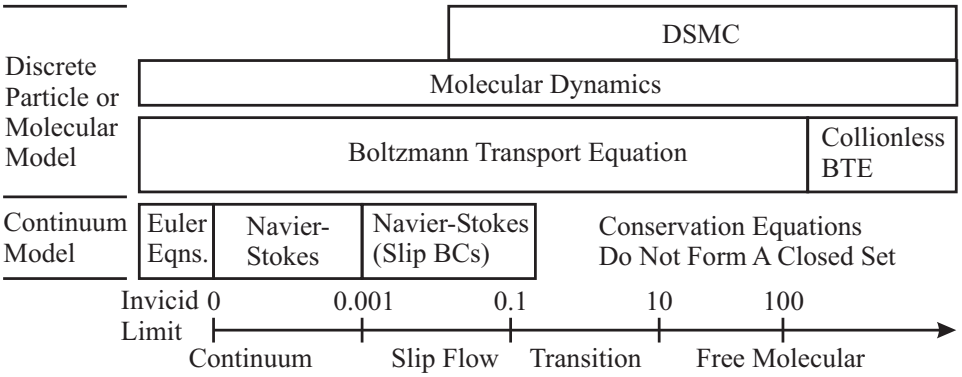

Figure 1-4: Flow regimes and applicable models as distinguished by Knudsen's Number (Kn = λ/L) [17]

As gas phase heat transfer between the cantilever and the surface is the key to the operation of the TSAFM, it is important that this be well characterized. However, the small scan height—typically less than 1 μm—may result in noncontinuum behavior. The mean free path, λ, of the working gas (air, *etc.*) at atmospheric pressure is on the order of 100 nm, resulting in a Knudsen Nnumber,Kn $>$ 0.1. As such, the flow regime of the gas phase phenomena in the region between the beam and the surface will likely be categorized as transitional or free molecular. Modeling rarefied flows requires detailed models that consider the molecular nature of the gas. However, the computational expense associated with

detailed models is significantly greater than the continuum approaches. Figure 1-4 presents a number of modeling techniques for fluid dynamics and the flow regimes in which they are suitable. The half-space above the TSAFM may be accurately modeled by a continuum (Navier-Stokes) or a molecular (MD, DSMC, BTE) model, while the region below the cantilever requires a molecular model.

Furthermore, the solid phase heat transfer within the sharp tip is another multiscale problem; the cantilever and the root of the tip may considered as a continuum, while the relatively few atoms near the end of tip cannot. As mentioned previously, solid phase heat conduction has been found to contribute little to the scanning mode and will therefore not be considered in this thesis, but further illustrates the interesting challenges of micro- and nano-scale modeling involving multiple scales and physical phenomena. Currently TSAFM scans are interpreted using continuum based models [53]. Preliminary studies, included in this thesis (see Chapter 5), have found that the TSAFM sensitivity is strongly affected by noncontinuum heat transfer phenomena [66, 67].

1.3 Goals and significance of this Research

In general, modeling techniques based on molecular models or first principles are valid at large and small scales. Practically, they are limited by computational expense to small scale simulations. On the other hand, the mature and highly efficient continuum techniques are inappropriate for any regions where noncontinuum effects may be manifest. The obvious solution then is to use the appropriate models for the appropriate regions (and regimes) of length scales. The difficulty comes in efficiently modeling the small subcontinuum regions and coupling this with the continuum to provide a valid and efficient modeling technique. The primary goals to be accomplished by this research are:

- Develop efficient numerical techniques for simulating low-speed subcontinuum gas phase flows

- Coupling the developed subcontinuum techniques with continuum techniques to address the issues discussed previously

- Apply these techniques to model the TSAFM and identify the effects of subcontinuum heat transfer, as well as other noncontinuum phenomena that may impact TSAFM operation (including the Knudsen force [59, 84, 85, 86]).

- Explore other interesting thermally driven microscale flows including Thermal transpiration which has application in microscale pumping and propulsion [4, 69, 75, 76, 104].

At the start of this research, the most significant aspect appeared to be the development of coupling techniques that could be used with existing micro- and macroscale models, based on methods reported in the literature. The Information Preserving DSMC method (see Chapter 3) was selected for microscale modeling. However, after implementing this method it soon became apparent that it was incapable of correctly modeling nonequilibrium thermally driven flows. However, the superior efficiency of the Information Preserving method and its considerable success with other noncontinuum flows make it very attractive, and therefore worthy of further investigation.

The primary significance of this work is the theoretical and practical development of an enhanced IP-DSMC technique for nonequilibrium thermally driven flows. This method, the Octant Splitting IP-DSMC (OSIP-DSMC), is capable of capturing complex thermally driven flows, including thermal creep effects. This provides an efficient method for modeling the behavior of rarefied gases in the presence of thermal loads. Furthermore, the method should be equally applicable to other nonequilibrium situations, and gracefully degenerates to correctly model lower dimensional flow problems and those without strong nonequilibrium behavior.

As an efficient and smooth method, the OSIP-DSMC may be coupled with continuum solvers. In this work, the OSIP-DSMC will be coupled with a BEM Laplace solver to

explore the behavior of the gas surrounding a heated cantilever, as in a TSAFM system. Observable in these simulations are a static pressure difference, or Knudsen force, between the top and bottom surfaces of the beam, as well as the two dimensional heat transfer through the rarefied gas. This will be compared to simplified 1D simulations

1.4 Thesis Outline

The organization for this thesis, including brief descriptions of each chapter, will be as follows:

Chapter 2: Kinetic Theory A review of the kinetic theory of gases and related numerical methods, including a review of multiscale modeling techniques

Chapter 3: Microscale Modeling A presentation of the microscale modeling techniques that will be developed and used in this research. A state of the art Information Preserving DSMC implementation will be described, and examples of the capabilities and deficiencies of the IP-DSMC presented. The theoretical and practical development of an enhanced IP-DSMC method, the Octant Splitting IP-DSMC will be presented, and shown to efficiently model a number of thermally driven flows.

Chapter 4: Macroscale Modeling A brief argument for using the Boundary Element Method as the continuum solver coupled to the OSIP-DSMC and a brief description of the BEM.

Chapter 5: Multiscale Modeling Describing the coupling of the OSIP-DSMC and the BEM using a modified Alternating Schwartz coupling. A simplified model using a macromodel for the subcontinuum heat transfer and simplified geometry is used to evaluate the sensitivity of a TSAFM system over a wide range of scan heights and operating powers. The results of a coupled OSIP-DSMC/BEM simulation of a TSAFM

cantilever are compared to the simplified results and the effect of the Knudsen Force is observed.

Chapter 6: Additional Thermally Driven Flows This chapter presents the results of OSIP-DSMC simulations of a number of additional thermally driven flows.

Chapter 7: Summary and Conclusions

CHAPTER II

KINETIC THEORY

The concept that matter is composed of discrete atoms or molecules dates to the time of the ancient Greeks. However, the proof, formal description, and general acceptance of the molecular/atomic nature of matter are products of the late 19th and 20th centuries. Science has now discovered not only molecules and atoms, but the myriad of subatomic particles—and where the "bottom" truly lies is still being explored. This discrete world is almost entirely invisible; as we experience matter and physical phenomena as local averages of underlying microscopic quantities. This chapter presents an overview of the molecular kinetic theory of gases and several related numerical approaches.

2.1 The Kinetic Theory of Gases

The kinetic theory of gases, developed in the late 19th century, largely due to the work of Maxwell and Boltzmann, seeks to describe the microscopic behavior of gases and from this to understand macroscopic thermophysical flow properties.

The basic assumptions are that: 1. molecules behave as idealized spheres with some molecular diameter, d, and mass, m (a common model is the Hard Sphere model which uses a fixed d), 2. molecules move randomly (although an ordered motion may be superimposed on the molecular chaos), 3. molecules obey classical Newtonian dynamics—ballistic motion, acceleration in response to external forces, *etc*., and 4. interactions between molecules are negligible except during collisions (near-field and quantum mechanical effects are neglected). Although science has found the true nature of atoms and molecules to be far more complex, the kinetic theory of gases admirably describes the behavior of many real

gas flows. Based on these assumptions, mathematical and numerical models describing the behavior of gases in terms of macroscopic quantities and loads may be developed.

Prior to presenting some of these models, it is important to define a number of characteristic lengths and flow regimes. The assumption that the intermolecular interactions are negligible except during collisions requires that the intermolecular spacing be significant, the average of which, δ, is related to the density, ρ, of the gas by

$$\delta = \left(\frac{\rho}{m}\right)^{1/3} = n^{1/3} \tag{2.1}$$

where the number density, $n = \rho/m$, is the number of molecules per unit volume and m is the mass of a single molecule (ρ is the conventional density, mass per unit volume). As the molecules move and interact with one another, the average distance between collisions is called the mean free path, λ. For a hard sphere gas this may be calculated as $\lambda = \left(\sqrt{2}\pi d^2 n\right)^{-1}$, or more generally as

$$\lambda = \frac{\sqrt{\pi}\mu}{2p}\left(\frac{2k_B T}{m}\right)^{1/2} \tag{2.2}$$

where k_B=1.3806505 $\times 10^{-23}$ is the Boltzmann constant and p, T, and μ are, respectively, the pressure, temperature and coefficient of viscosity of the gas.

Finally, the so-called "characteristic length", L may be defined in terms of the geometry, but often is more accurately defined in terms of the local flow gradients, *e.g.* for a density gradient,

$$L = \frac{\rho}{\mathrm{d}\rho/\,\mathrm{d}x} \tag{2.3}$$

Figure 2-1 illustrates how these may be used to identify flow regimes [17]. The ratio δ/d is a measure of the fraction of space occupied by molecules. If $\delta/d < 7$ then the gas should be considered dense, and molecules will be strongly affected by the many molecules around them. If however δ/d is large, then the molecules occupy little of the space and the gas is considered dilute. Molecules in a dilute gas are unlikely to be affected by any more than one other molecule at a time, thus collisions in a dilute gas are assumed to be binary.

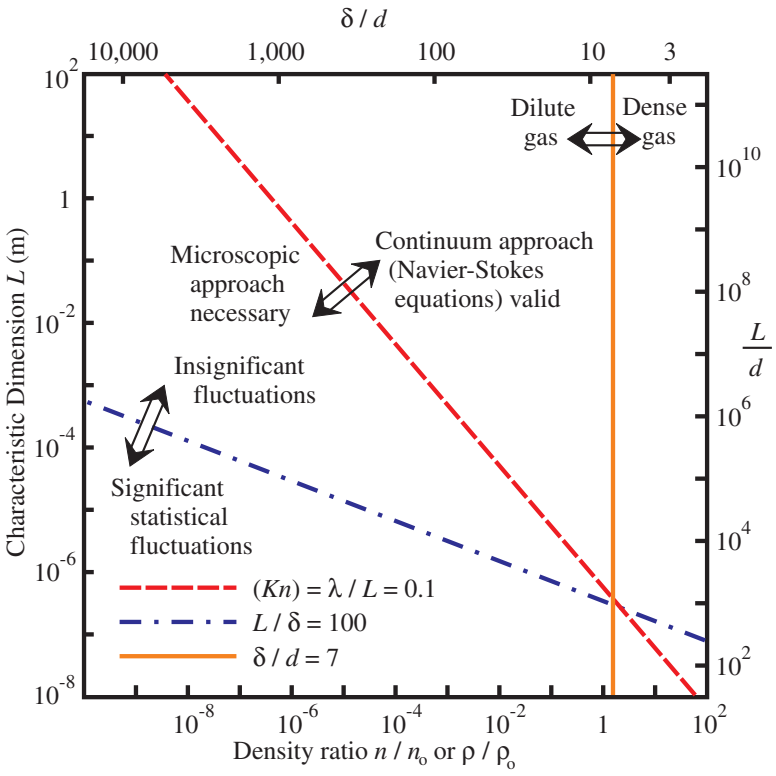

Figure 2-1: Flow Regimes [17].

The ratio of L/δ gives some sense of the number of molecules occupying a region of interest. Large L/δ, *e.g.*, $L/\delta > 100$, indicate that a sizeable number of molecules occupy the region and that statistical fluctuations may be neglected. (The approximate number of molecules corresponding to this limit is $(L/\delta)^3$ or 1×10^6).

Finally, the Knudsen number Kn is defined as the ratio of the mean free path to the characteristic length, or Kn = λ/L. For very small Kn the microscopic effects become less important, and in the limit as Kn $\rightarrow$ 0 the flow may be considered inviscid and can be described by the Euler Equations. With increasing Kn the effect of boundary interactions becomes more important on the flow until around Kn = 0.1 the continuum assumptions break down (see Section 2.2.2 for further explanation of this breakdown). For large Knudsen number (Kn > 10), intermolecular collisions are extremely rare, and boundary interactions dominate the behavior of the gas in what is termed *free molecular* flow. In intermediate

or *transition* flows (where $0.1 < \mathrm{Kn} < 10$) the influence of boundary interactions are of similar order to intermolecular interactions.

2.2 Microscopic Approaches

A large Knudsen number, and the accompanying breakdown of the continuum description, may be the result of a large mean free path, *i.e.*, a highly dilute gas, or small characteristic lengths—even in dense gases. Thus the kinetic theory of gas, and the related methods, are equally applicable to large- and small-scale systems within the appropriate flow regimes. The following will review some of the techniques that have been developed to accurately model the microscopic behavior of rarefied gases. These may be divided into two main categories: mathematical models and direct simulation models.

2.2.1 Mathematical Model: Boltzmann Equation

One of the pioneers of the kinetic theory, James Clerk Maxwell, proposed a velocity distribution function $f_0(\boldsymbol{c}, \boldsymbol{x}, t)$ to describe the behavior of an equilibrium gas. This distribution provides the probability of a particle having a given velocity at a given location and time. The general form of this Maxwellian distribution in three dimensions (neglecting spatial and transient variations) is

$$f_0(\boldsymbol{c}') = \frac{\beta^3}{\pi^{3/2}} \exp\left(-\beta^2 c'^2\right) \tag{2.4}$$

where $\beta = (2RT)^{-1/2}$ is the reciprocal of the most probable velocity c_{mp}.

In general, macroscopic quantities may be obtained from a distribution function f, by integrating to obtain the averages or moments of the distribution:

$$\overline{\boldsymbol{Q}} = \int_{-\infty}^{\infty} \boldsymbol{Q} f(\boldsymbol{c}) \, \mathrm{d}\boldsymbol{c} \tag{2.5}$$

The Boltzmann Equation expresses the change in a distribution function with respect to time and space.

$$\frac{\partial}{\partial t}(nf) + \boldsymbol{c} \cdot \frac{\partial}{\partial \boldsymbol{x}}(nf) + \boldsymbol{F} \cdot \frac{\partial}{\partial \boldsymbol{c}}(nf) = \int_{-\infty}^{\infty} \int_{0}^{4\pi} n^2 \left(f^\star f_1^\star - f f_1\right) c_r \sigma \, \mathrm{d}\Omega \, \mathrm{d}\boldsymbol{c}_1 \tag{2.6}$$

where the first term on the left hand side is associated with the time rate of change of the distribution, the second is associated with the effect of spatial gradients, and the third the effect of external forces ($\boldsymbol{F}$). The term on the right hand side is the *collision integral* or operator and is associated with changes resulting from collisions of molecules. The assumptions involved in the Boltzmann Equation are: 1. the gas is dilute, which leads to the next two assumptions, 2. that collisions are binary, and 3. assumed to be instantaneous events at a fixed location in physical space, finally 4. the molecular motion is assumed to be in a state of chaos, This final assumption allow the two particle distribution function describing the relative velocities of collision pairs to be approximated by the product of two single particle distributions. The moments of the Boltzmann Equation result in the Boltzmann Transport (or Transfer) equations for the collision invariants—quantities unchanged by collisions—of mass, momentum, and energy:

$$\frac{\partial \rho}{\partial t} + \frac{\partial}{\partial x_i}\left(\rho v_i\right) = 0 \tag{2.7}$$

$$\frac{\partial}{\partial t}\left(\rho v_j\right) + \frac{\partial}{\partial x_i}\left(\rho v_i v_j + p_{ij}\right) = \rho F_i \tag{2.8}$$

$$\frac{\partial}{\partial t}\left[\rho\left(\frac{1}{2}v^2 + e\right)\right] + \frac{\partial}{\partial x_i}\left[\rho v_i\left(\frac{1}{2}v^2 + e\right) + p_{ij}v_j + q_i\right] = \rho F_i v_i \tag{2.9}$$

where $v_i = \overline{c_i}$ is the macroscopic velocity component, p_{ij} is the pressure tensor, q_i is the heat flux vector and e represents internal energy modes (vibrational and rotational). These equations, also known as the conservation equations, could also have been deduced from first principles.

Direct evaluation of the Boltzmann equation for simulating rarefied flows requires considerable computing power and is possible only for simple flows and geometries as it requires the formulation and evaluation of the time and spatial evolution of the distribution function and the collision integral terms [17, 93]. Direct approaches have usually utilized Monte Carlo integration techniques to evaluate the collision integral. Simplifying methods, including the BGK, or BKW (Bhatnagar, Gross & Krook [12], and Welander [109]) model for the collision operator allowed simpler solution of the Boltzmann Equation. Other

methods, including the H and S models serve a similar purpose [93]. The BGK model for a distribution f takes the form of

$$\frac{\partial f}{\partial t} + \boldsymbol{c} \cdot \frac{\partial}{\partial \boldsymbol{x}}(f) + \boldsymbol{F} \cdot \frac{\partial}{\partial \boldsymbol{c}}(f) = A_c \rho (f_e - f) \tag{2.10}$$

where A_c is a constant such that $A_c\rho$ provides the collision frequency, independent of $\boldsymbol{c}$, and f_e is a local Maxwellian with ρ, $\boldsymbol{c}_0$, and T derived from f as its parameters. Recent work by Sone, Ohwada, Aoki, and others have demonstrated efficient methods utilizing the Boltzmann Transport Equations and have applied these to a number of interesting 2D flows [97, 98, 6, 7]. In many cases the linearized Boltzmann equation is used in conjunction with the simplified collision model [98, 93]. Other methods based on the Boltzmann Equation include the Lattice Boltzmann which utilizes a lattice on which particle distributions are allowed to travel and interact at nodes. The BGK model is often used for the collision, or relaxation, operations. Most Lattice Boltzmann implementations are based on the Chapman-Enskog expansion and are able to recover the behavior of the Navier-Stokes equations, while providing a flexible and efficient discretization and solution method [63].

2.2.2 Navier-Stokes Equations

Before leaving the mathematical models it is important to present the Chapman Enskog distribution and discuss its significance. The Chapman-Enskog distribution is an expansion of the Maxwell distribution and represents a slight perturbation from equilibrium. This may be expressed simply as

$$f = f_0 \Gamma = f_0 (1 + \Phi_1) \tag{2.11}$$

where $\Gamma = (1 + \Phi_1)$ is the perturbation expansion, or more precisely

$$f = f_0 \left(1 - \frac{4K\beta^2}{5nk_B} \left(\beta^2 c'^2 - 5/2 \right) \boldsymbol{c}' \cdot \frac{\partial \ln T}{\partial \boldsymbol{r}} - \frac{4\mu\beta^4}{\rho} \boldsymbol{c}'^0 \boldsymbol{c}' : \frac{\partial \boldsymbol{c}_0}{\partial \boldsymbol{r}} \right) \tag{2.12}$$

The Chapman-Enskog distribution may be manipulated to yield the following relationships relating the shear stresses and heat fluxes to the macroscopic quantities:

$$\tau_{ij} = \mu \left(\frac{\partial v_i}{\partial x_j} + \frac{\partial v_j}{\partial x_i} \right) - \frac{2}{3} \delta_{ij} \mu \frac{\partial v_k}{\partial x_k} \tag{2.13}$$

and

$$q_i = -K\frac{\partial T}{\partial x_i} \tag{2.14}$$

which may be substituted into the conservation equations, Equations (2.7)-(2.9) producing a closed set of equations for continuum fluid dynamics—the Navier-Stokes equations [17, 24]. Thus the applicability of the Navier-Stokes equations is subject to the same limits as the Chapman-Enskog distribution, namely that the gradients, $\frac{\partial T}{\partial x_i}$ and $\frac{\partial \mathbf{c}_0}{\partial \boldsymbol{x}}$, on which the perturbation is based be small. Conventionally this limit is expressed in terms of the Knudsen Number and requires that Kn < 0.1 for the Chapman-Enskog and the Navier-Stokes equations to be valid. The validity of the Navier-Stokes equations may be extended slightly to near-continuum flows by the addition of "slip" boundary conditions. The Burnett equations, a more complicated extension of the Chapman-Enskog distribution, may also extend the validity of the Navier-Stokes equations.In any case, the Navier-Stokes equations are the basis of most continuum computational fluid dynamics simulation techniques, utilizing a variety of numerical discretization and solution methods, including finite element (FEM) and finite volume (FVM)methods.

2.2.3 Direct Simulation: Molecular Dynamics

Due to the difficulties involved in evaluating the mathematical models, a number of physically based, or direct simulation, models have also been proposed. The first of these is the Molecular Dynamics method, or MD. Molecular Dynamics simulates a set of molecules, subject to a number of rules that describe the behavior of the molecules and their interactions each other, boundary conditions, and body forces. For example, one simple model would consist of a hard sphere gas obeying Newtonian physics and could equally describe a simple gas—or a game of billiards.

The set of simulation molecules must be generated with some set of initial conditions: positions, velocities, *etc*., based on macroscopic quantities and random numbers. The simulation then proceeds by moving the particles and evaluating their interactions based on

the prescribed set of rules. For a hard sphere gas, intermolecular interactions occur only when the particle trajectories intersect. Molecular Dynamics may also be applied to dense gases, liquids, and solids by using more elaborate models that evaluate intermolecular potentials (*e.g.*, Lenard-Jones potential). Although the initial state is randomly generated, the subsequent operation of a Molecular Dynamics simulation is entirely deterministic.

The principal difficulty in applying the MD to rarefied gas dynamics is the extreme computational expense. Consider that within one cubic micrometer of air at standard temperature and pressure there are over 25 million molecules. This allows only very small quantities of gas to be modeled—usually insufficient for macroscopic significance. However, the MD is extremely useful in modeling dense media, where smaller samples may indeed yield important insight.

2.2.4 Direct Simulation Monte Carlo

Dr. Graeme A. Bird proposed the direct simulation Monte Carlo method (DSMC) in 1963 as an efficient means of modeling high-speed, high-altitude aerodynamic flows [16, 17]. Over the years the method has been improved and is now used routinely for macroscopic and microscopic simulations [18, 80]. Furthermore, it has been proven to be a solution of the Boltzmann transport equation (BTE) [9, 73], and has been used to model complex gas flows involving single and multiple species of monatomic and polyatomic gases [17, 80, 18], and recently dense gases [39] and even granular media [71].

The method relies on two main assumptions: 1. The gas is dilute and 2. the gas is in a state of molecular chaos. The first condition requires that the intermolecular spacing δ is much larger than the effective diameter d of the molecule, *i.e.*, $\delta \gg d$. As previously discussed, this leads to the assumption that the intermolecular collisions are all binary (or that the number involving more than two particles are extremely insignificant). The second condition allows collisions to be treated as a function of the product of two single particle

distributions ($f(\boldsymbol{x}_1, \boldsymbol{c}_1)f(\boldsymbol{x}_2, \boldsymbol{c}_2)$), rather than the more complex—and often intractable—two particle distribution ($f(\boldsymbol{x}_1, \boldsymbol{c}_1\boldsymbol{x}_2, \boldsymbol{c}_2)$). This then provides a workable means of determining the average number of collision pairs. If the probable number of collisions may be determined *a priori* and the molecules are in a state of molecular chaos, then collisions may be treated probabilistically. Therefore, instead of tracking particle trajectories (or evaluating or potential interaction), the motion and collisions may be decoupled. This allows for a small set of simulation molecules to be used: each representing a much larger number of real molecules and whose pre- and post-collision behavior reflects the statistical behavior of the real molecules. The description of the DSMC method included in this chapter is drawn primarily from Bird's classic text on the subject [17].

The basic operation of the DSMC is as follows (also refer to the flowchart in Figure 2-2):

1. Simulation molecules are initialized with spatial distributions and velocities based on the macroscopic density, temperature, and velocity of the initial conditions
2. New molecules are inserted at inlets of open systems
3. Molecules are moved based on an Euler step ($\boldsymbol{x}^{(t+\Delta t)} = \boldsymbol{x}^{(t)} + \Delta t\boldsymbol{v}$), with time step Δt
4. Molecules are sorted into computational cells and subcells
5. The number of candidate collision pairs from each cell is determined and these are selected (using subcells to increase likelihood of collision pairs being near neighbors). Collision is evaluated and (if the collision occurred) the post-collision behavior is calculated.
6. Macroscopic quantities are sampled from molecules

Although the DSMC is far more efficient than Molecular Dynamics for rarefied flow simulations, it remains quite intensive. This is due to the still considerable number of

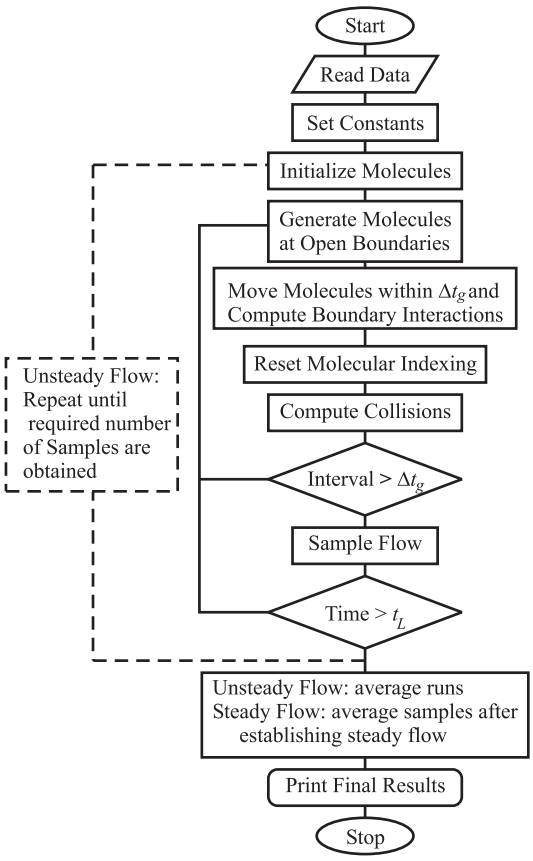

Figure 2-2: Flowchart of DSMC steps

simulations particles necessary for accurate modeling and the large number of samples required to obtain statistically valid results. Low-speed flows present additional challenges as the thermal velocities of the simulation molecules are much greater than the stream velocities of interest. This causes significant statistical fluctuations in sampling and requires large numbers of samples to obtain valid results. As such the computational expense of a DSMC simulation for low-speed flows may be orders of magnitude greater than a comparable high-speed flow simulation. Recently, a number of enhancements have been made to improve the efficiency of the DSMC by reducing statistical scatter. One such method is the Information Preserving DSMC, which will be discussed and extended in Chapter 3.

2.2.5 Microscopic Sampling

In a mathematical model of a gas, conventional macroscopic quantities may be obtained from the distribution function by evaluating the moments of the distribution; see Eq. (2.5). However, in particle methods, as in the real gas, the molecules, and their distributions are discrete and conventional averages are used. The formulation for the various macroscopic quantities in terms of microscopic quantities are presented in Table 2-1 [17], where microscopic averaging of a quantity $\boldsymbol{Q}$ is defined as:

$$\overline{\boldsymbol{Q}} = \frac{1}{N} \sum_{i=1}^{N} \boldsymbol{Q} \tag{2.15}$$

These are equally applicable to real, DSMC, and MD molecules with the exception that each DSMC molecule represents a large number of real molecules, necessitating the inclusion of the *effective number*, F_N, in the definition of the density and any terms involving the density, thus $\rho = \sum F_N m_i/\Omega$. In continuum models, the microstates are never directly assessed, but the relationships between the various macroscopic quantities are based on the constitutive laws; see Equations (2.13)-(2.14).

2.2.6 Gravity and Thermally Driven Flows

Throughout this study the effect of gravity will be neglected. This is a common assumption in microscale simulation and gas dynamics and may be justified by considering that the force of gravity scales with the volume, whereas most other forces of interest are due to surface effects (pressure, shear, electrostatic force, *etc*.). At small scales surface effects tend to dominate, as the surface to volume ratio increases. Consequently, in this thesis the term "thermally driven flow" never refers to buoyancy driven natural convection, but rather to flows driven by thermal stresses. Omitting gravity not only simplifies the analysis, but serves to isolate the phenomena of interest.

The kinetic theory of gases provides a theoretical understanding of the nature of gases, especially under rarefied conditions. A number of methods have been developed to model

Table 2-1: Microscopic Sampling Definitions

Quantity	Equation
Number Density	$n = N/\Omega \approx F_N N/\Omega$
Density	$\rho = \sum m_i/\Omega = nm \approx F_N Nm/\Omega$
Stream Velocity	$c_{0i} = \overline{c_i}$
Thermal or "Peculiar" Velocity	$c'_i = c_i - c_{0i}$
Translational Temperature	$3RT_{tr}/2 = \overline{c'^2}/2 = \left(\overline{c^2} - c_0^2\right)$
Pressure Tensor	$p_{ij} = nm\overline{c'_i c'_j} = \rho\left(\overline{c_i c_j} - c_0^2\right)/2$
Scalar Pressure	$p = nm\overline{c'^2}/3 = \rho\left(\overline{c^2} - c_0^2\right)/3$
Shear Stress	$\tau_{ij} = \left(nm\overline{c'_i c'_j} - \delta_{ij}p\right)$
Heat Flux (ε_{int} is the non-translational energy associated with internal degrees of freedom)	$q_i = \frac{1}{2}nm\overline{c'^2 c'_i} + n\overline{\varepsilon_{int} c'_i}$ $= \frac{1}{2}\left(\rho\left(\overline{c^2 c_i} - \overline{c^2 c_i}\right) - 2p_{ij}c_i\right) + n\left(\overline{\varepsilon_{int} c_i} - \overline{\varepsilon_{int}} c_{0i}\right)$

real gases based on the kinetic theory. The DSMC is perhaps the most flexible and widely used for modeling a range of complex micro- and macroscale systems—from the space shuttle to micro thrusters. Coupling the DSMC with a continuum model is complicated by large statistical scatter, which is exacerbated at extremely small length scales and low speeds. The following chapter will discuss enhancements to the DSMC to reduce this scatter, including the IP-DSMC and a significant contribution of this research, the Octant Splitting IP-DSMC.

2.3 Multiscale Techniques

The need for accuracy and efficiency in the modeling of systems that span various length scales and flow regimes leads logically to multiscale modeling, wherein various models are used only where they are appropriate for the scale and physics and coupled in some manner to form a global model. The commercial and technical possibilities of micro- and

nanoelectromechanical systems have motivated considerable research addressing the multiscale simulation and design challenges inherent in such systems. Various methods have been presented for modeling the behavior of solids, liquids, and gases, including: concurrent coupling of length scales of Rudd and Broughton [89], the Quasicontinuum method of Shenoy *et al*. [95], and multiscale modeling of laser ablation (coupling MD and DSMC for solid, liquid and gas phase modeling) [117, 118]. Some more general frameworks for multiscale modeling have also been proposed *e.g.*, the Equation Free Multiscale Method of Kevrekidis and associates [51] and the Heterogeneous Multiscale Method of E and Engquist [30]. The following will review a number of the proposed methods and coupling schemes and suitable for rarefied gas dynamics and identify the method that will be explored in this thesis.

2.4 Coupling Criteria

In many cases where multiscale modeling is undertaken, the individual modeling techniques are mature: Finite Element, Finite Difference, *etc*. for continuum and Molecular Dynamics or DSMC for noncontinuum modeling. As such, the coupling scheme is often the primary focus. A necessary condition for any coupling scheme is that the models to be coupled be consistent within the coupling region. This of course requires that coupling be performed in a *continuum* region (or near-continuum with appropriate "slip" conditions). It then remains to: *a*) select (or develop) appropriate and efficient models for the micro- and macroscopic phenomena of interest; *b*) identify what quantities are to be matched and where; *c*) provide a means for the sampling of macroscopic quantities and the generation of microscopic distributions.

In general, molecular models involve very small timescales, large numbers of molecules, and—due to the statistical and/or stochastic nature—large sample sets. Techniques to improve the efficiency while maintaining accuracy of the microscale models have received considerable attention in the literature and will be the subject of Chapter 3.

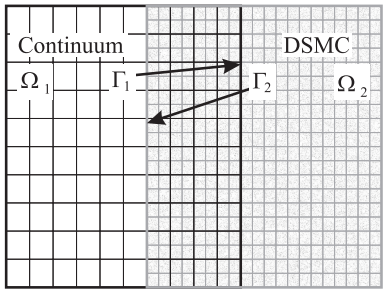

2-3(a): Schwarz Coupling

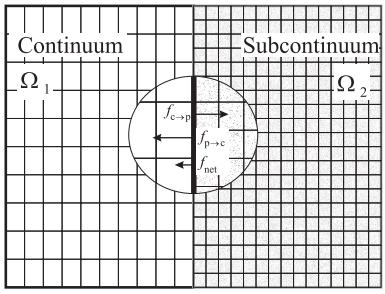

2-3(b): Marshak Condition

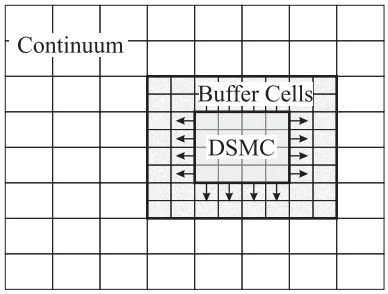

2-3(c): AMAR Coupling

Figure 2-3: Coupling schemes

Although quite expensive, macroscopic quantities such as temperature, pressure, and velocity can be sampled directly from the microscale models. The return path is more difficult: particles to be inserted into the microscale model must be generated from some (perhaps unknown) distribution functions to reflect the macroscopic properties of the continuum model. Some techniques have been developed based on the BGK solution of the Boltzmann Transport Equation coupled with a Navier-Stokes Finite Difference discretization which avoid the need to generate particles, but still require an approximation not only of the particle distributions, but of the collision operator [78].

A variety of coupling schemes have been proposed, either specifically for multiscale modeling, or as derivatives of conventional domain decomposition schemes (wherein the domain is *decomposed* into smaller regions for improved computational efficiency and/or parallelism, usually involving the same modeling technique for all sub-domains). The following review will present a number of multiscale modeling efforts in rarefied dynamics.

One method that is quite intuitive, and has seen considerable attention, and success is the Alternating Schwarz Coupling (or simply Schwarz Coupling). Generally this method utilizes overlapping regions, Ω_1 and Ω_2 that correspond to the continuum and subcontinuum models (see Figure 2-3(a)). Coupling is accomplished by 1. solving each region, *e.g.*, Ω_1, subject to the boundary conditions on Γ_1, 2. applying this solution to the overlapped portion of the boundary, Γ_2, of the second region, Ω_2, 3. and repeating steps 1 and 2 for each region in turn, until the solutions on the boundary of the overlapped region, $\Omega_1 \cap \Omega_2$, converge. In the case of incompressible and/or steady flows, there is a unique solution within the overlapping region, thus ensuring that all quantities, gradients, and fluxes at the interface are correct.

Schwarz coupling was first applied to gas phase multiscale modeling by Aktas and Aluru as a means of coupling the Finite Cloud Method (FCM) and DSMC to model fluid flow through microfilters [1, 2]. They point out that Schwarz coupling can be accomplished with non-overlapping boundaries and Neumann (or Robin) boundary conditions, but this was not done to avoid estimating derivatives of flow quantities.

In the implementation of Aktas and Aluru, particle velocities were selected from the Maxwellian distribution. In a similar study utilizing Schwarz coupling for multiscale DSMC-Navier Stokes simulations, Wijesinghe and Hadjiconstantiou point out the importance of selecting the correct microscopic distribution function, which for most nonequilibrium continuum/near-continuum flows will be the Chapman-Enskog distribution [111, 112]. Sampling particle velocities from the Chapman-Enskog distribution is slightly more expensive than using the Maxwellian, but not prohibitive (see Section 5-10) [37]. They also present an extension of the Schwarz coupling method to unsteady flow, wherein the solution found for a given point in time is used as the initial state for the next time step and treating each time step as a quasi-steady state [112].

Hash and Hassan compared a number of different coupling schemes for Navier-Stokes and Monte Carlo simulations including: 1. the Marshak condition, 2. the extrapolation of

flow properties, 3. the extrapolation of net fluxes, and 4. the use of asymptotic values of the solution of the linear kinetic half-space problem. Of these schemes, the second was found to have excessive error, and the last is similar to the Marshak condition but is only necessary for problems with severe translational non-equilibrium. Of the remaining methods, the Marshak condition was determined to be preferable—offering consistent performance and accuracy [45]. The Marshak condition requires the conservation of fluxes at the interfaces. Flux conservation is accomplished by calculating the half-fluxes and equating their sum to the net flux (obtained from the continuum solution). The half flux leaving the DSMC region is a simple sum of the quantities transported by particles leaving the DSMC region. The half flux entering the DSMC region from the continuum region can be calculated based on the chosen distribution (Chapman-Enskog). The result is a set of equations that can be solved to obtain the boundary condition properties to be applied in the following iteration step (see Figure 2-3(b)) [45].

A similar scheme has been utilized by Sun *et al*. [102] to couple DSMC and finite volume method models in a time stepping solver (*i.e.*, the fluxal quantities are integrated to obtain the temperature, pressure, *etc*. for the next step). Although they suggest the Marshak (non-overlapping) conditions as a possibility, they determine that generating particles at the interface may lead to instability and inaccuracy in high speed flows or in flows which result in cells with few particles. As an alternative, they suggest an overlapping method with buffer and reservoir cells. At each DSMC time step, particles are generated in the reservoir cells. The buffer cells improve the quality of the generated particles by allowing them to interact with each other, and particles that have recently left the DSMC simulation domain, prior to entering the DSMC simulation. Only the particles that are within the main DSMC cells contribute to the solution. The fluxal quantities of the DSMC replace those of the continuum finite volume method (FVM) cells in the solution. The continuum solutions for the temperature, velocity, density (or pressure) and heat flux at the locations of the reservoir cells are used to generate particles from the Chapman-Enskog distribution (see

Section 5-10). As a further enhancement, an Information Preserving DSMC method (see Chapter 3) is used to reduce the statistical scatter and computational expense that would otherwise dominate low-speed flows (as are common in MEMS and NEMS flows)(see [32, 22, 100, 108]).

Garcia, *et al*. [38] and Wijesinghe, *et al*. [110] describe an adaptive mesh and algorithmic refinement (AMAR) method which automatically refines the continuum (FVM) analysis mesh and when necessary switches to a DSMC solver. In this method each successive refinement overlays the coarser mesh it replaces and its fluxal quantities (that will be used for time stepping, similar to the method of Sun *et al*.). When non-continuum conditions are detected (*i.e.*, mesh refinement reaches a specified limit) within a region, DSMC cells are generated with particle distributions influenced by the overlaying continuum solution. Buffer cells are used to generate particles at each DSMC time step with distributions based on an interpolation of the solutions of the current and next continuum time steps. After iterating the DSMC solution for enough microscale time steps to equal the continuum time step of the overlaying continuum grid, the DSMC solution then replaces the continuum solution in the affected region. The accuracy of the coupling is further enhanced by "refluxing," wherein the fluxal quantities due to particles leaving or entering the DSMC region (from the buffer cells) are used to calculate corrections for the continuum elements adjacent to the DSMC region.

Similar efforts utilizing flux matching schemes are presented by O'Connell and Thompson (MD-continuum solution for fluid systems) [77]; Flekkøy (general hybrid model using Navier-Stokes and Lennard-Jones MD for combined particle and continuum dynamics) [34]; Delgado-Buscalioni and Coveney (whose work follows Flekkøy but extended to unsteady flows and emphasizes the need for coupling to depend on fluxes and not merely matching boundary) [28]; and Bourgat *et al*. [20] and Le Tallec and Mallinger [57] who couple Navier-Stokes and Boltzmann solvers for modeling the reentry of high altitude vehicles via half fluxes (they also suggest friction as a coupling method).

2.4.1 Discussion

The above methods may be classified as flux matching or state matching, the former (Marshak condition, etc.) explicitly conserve fluxal quantities of mass, momentum, and energy, while the latter (*e.g.*, Schwarz coupling) can only ensure fluxal conservation after convergence. Whether the method needs to be explicitly flux conserving appears to be problem dependent. Wijesinghe and Hadjiconstantinou discuss the applicability of different coupling schemes to different classes of problems and note that flux matching schemes are often implemented in unsteady solvers but then used to solve steady state problems, an approach that is usually less efficient than a steady solver using state matching. They feel that the choice of coupling scheme should depend on the flow physics—avoiding the expense of a flux matching unsteady solver if it is not needed—and not, as they put it, "researcher bias". However, the balance of computational and development costs may be best achieved by a scheme that is generally applicable to steady and unsteady flows.

2.5 Approach

For rarefied gas dynamics, the obvious choice, in terms of accuracy and flexibility, is the direct simulation Monte Carlo. As the targeted applications of this thesis are low-speed—specifically thermally driven flow—it is assumed that the flow velocities within continuum regions of the domain are very small. In the absence of bulk flow, it may be possible to avoid the complexity of a full Navier-Stokes model, and focus instead on conduction as the dominant heat transfer mechanism. This allows a Laplace solver to be used for the continuum modeling. As such, this thesis will explore the applicability of the Boundary Element Method (BEM) for modeling the continuum heat transfer in the gas. The interest for this is based on the efficiency of the BEM and its ability to simulate infinite and semi-infinite domains and its efficiency in coupling with DSMC. Based on these assumptions, it seems logical to use a state matching scheme, specifically the Alternating Schwarz

Coupling, with modifications to ensure that particles are generated from the appropriate (Chapman-Enskog) distribution.

Although low-speed flows seem to have simplified the treatment of continuum modeling and coupling, they present a significant challenge for microscale modeling. As such, the IP-DSMC will be used for the non-continuum gas phase dynamics. Initially it was thought that this method would adequately describe the noncontinuum behavior of thermally driven flows, but, as will be shown in Chapter 3, in its present form it is incapable of capturing many of the phenomena of interest to this research. Chapter 3 will present not only a detailed description of the IP-DSMC, but the derivation of an enhanced model for detailed analysis of thermally driven flows.

CHAPTER III

MICROSCALE MODELING

This chapter presents the motivation and theoretical description of the Information Preserving DSMC as well as GT-DSMC, a parallel object oriented implimentation of the method. A number of different flows will be studied to explore the capabilities of the IP-DSMC leading to the formulation of further enhancements that greatly extend the method.

3.1 Low-Speed Flows

Particle methods, such as the DSMC are, in general, accurate for rarefied flows at both the macroscale and microscale. However, these simulations require considerable computational effort, frequently involving many millions of simulation molecules. The computational effort depends not only on problem size, but on the flow conditions. As shown in Figure 2-1, microscale flows may involve significant statistical fluctuations due to the small number of particles contained within the computational domain. Furthermore, low-speed flows are quite common—from stationary to 10's of m/s—particularly when thermally driven. Microscale systems involving high-speed flows do exist, including micro-turbines [35] and read-write heads on standard hard drives [3, 25] and the method developed here are equally applicable. Low-speed flows present additional challenges in DSMC modeling as a very large number of samples must be taken to obtain statistically significant averages of the macroscopic quantities. This may be quantified: first consider that simulation (and real) molecules have velocities on the order of the average thermal speed $\overline{c'} = \sqrt{8RT/\pi}$ (for Argon at room temperature $\overline{c'} \approx 400$ m/s), where R is the species specific gas constant. Hadjiconstantinou, *et al*. provide a formulation for determining the number of samples, M, necessary to obtain valid statistical samples to a given degree of

precision [42]. For the macroscopic velocity this may be calculated as

$$M = \frac{1}{\gamma A_c^2 N_0 M a^2 E_u^2} \tag{3.1}$$

where A_c is the acoustic number ($A_c = 1$ for a dilute gas), γ is the specific heat ratio, N_0 is the number of particles in the cell, Ma $= |c|/a$is the Mach number ($a = \sqrt{\gamma k_B T_0/m}$) and E_u is the desired fractional error. Keeping a fixed number of molecules and number of samples, the fractional error in the density would be approximately

$$E_\rho = \frac{1}{\sqrt{M N_0}} \frac{1}{A_c} \tag{3.2}$$

and for temperature

$$E_T = \frac{1}{\sqrt{M N_0}} \sqrt{\frac{k_B}{c_V}} \tag{3.3}$$

(For an ideal gas $c_v = 3\,k_B/2$.) Based on these equations, if a maximum error of 1% were desired from a simulation of Argon at 423 K flowing at 10 m/s using an average of 100 simulation particles per computational cell, then 88,000 independent samples would be required. Errors in density, temperature, and pressure would be 3.3%, 2.8%, and 4.3%, respectively. If now the stream velocity, $\boldsymbol{c}_0$, were 1 m/s, 8×10^6 samples are needed to achieve the same resolution for the velocity (The increased number of samples does however reduce the error for the other quantities to below 1%). Thermally driven flows may have even lower speeds, requiring a prohibitive number of samples. Low-speed flows also complicate the treatment of open boundaries which may require special treatment for inlets and outlets [74, 88, 114, 115, 116].

3.2 Information Preserving DSMC

A number of techniques have been proposed to address the computational expense associated with DSMC simulation of low-speed flows [82, 83], but one of the most successful is the Information Preserving DSMC (IP-DSMC) [31]. In this method, certain macroscopic

quantities are "preserved" along with the microscopic velocities used in the DSMC simulations. These preserved quantities are then transported by particle movement and modified by boundary interactions, particle collisions, and fluxal modifications.

The initial implementations of the IP-DSMC preserved only the macroscopic velocity and explicitly assumed isothermal flow conditions [31, 22]. Since then, a number of models have been suggested to extend the method to non-isothermal flows by using modified collision diameters [32] and additional energy terms [21, 100]. For flows with greater non-linearities, the IP-DSMC was further enhanced by using kinetic fluxes for the mass, momentum, and energy fluxes, but results were not entirely satisfactory [94, 107]. However, many of these innovations have been somewhat *ad hoc* in their formulations, although attempts at a formal theory have been made [99, 100].

3.2.1 Preservation of Macroscopic Quantities

At a minimum, a scheme such as the IP-DSMC must satisfactorily reflect the macroscopic state corresponding to the ensemble of the microscopic states of the underlying real molecules. The DSMC satisfies this by using a small set of simulation molecules, each of which is a representative molecule of a larger set of real molecules (see Figure 3-1(c)) that have been "grouped" in some fashion (see Figure 3-1(b)). Thus the DSMC molecule is the single representative of a larger group, but has no information regarding the ensemble other than the number of molecules it represents. Throughout the simulation, each simulation molecule obeys the same physics that the real molecules are assumed to obey, although collisions are determined in a probabilistic manner. The IP-DSMC constitutes an attempt to capture and preserve the information present in the larger set of "real" molecules that are *ignorantly* represented by the DSMC molecule (see Figure 3-1(d)). In other words, a DSMC molecule carries only information regarding its own position and velocity, whereas the IP-DSMC supplements this with information regarding the average behavior of the ensemble. Although the true microscopic states of the individual "real" molecules are not

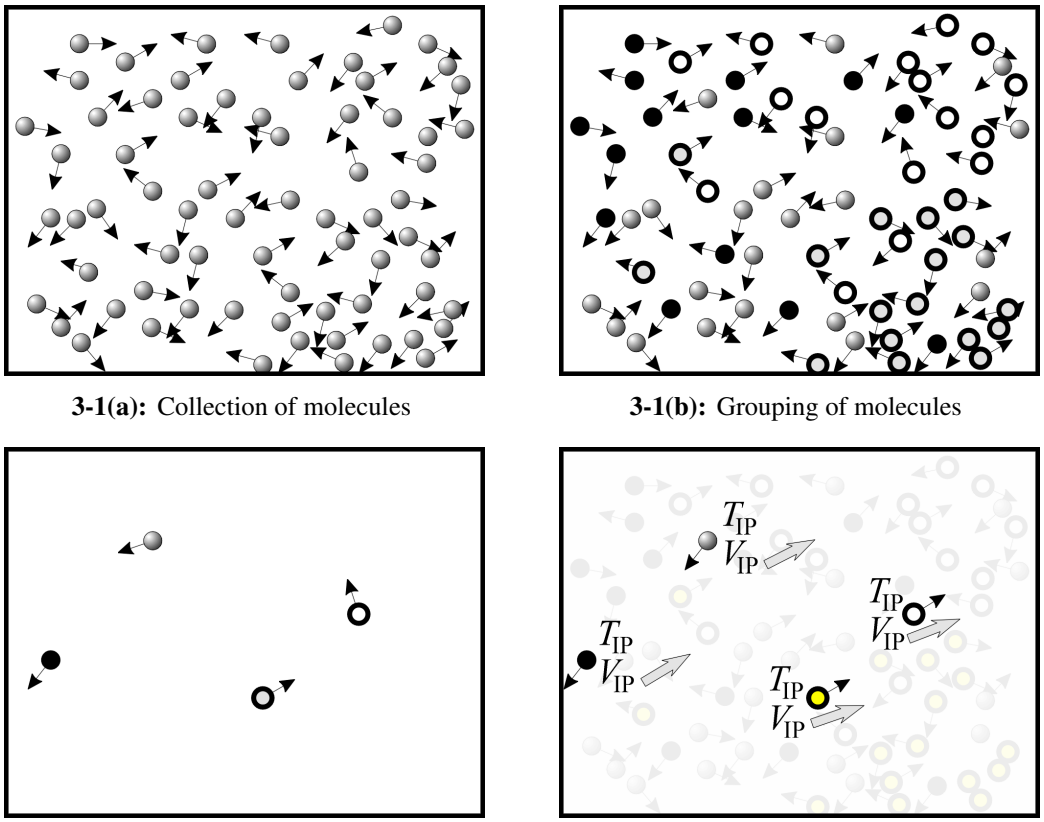

3-1(a): Collection of molecules

3-1(b): Grouping of molecules

3-1(c): Representative (DSMC) molecules (black) and the groups of real molecules they represents

3-1(d): Preserved average quantities (velocity, temperature, *etc*.) of the real molecules represented by simulation molecules

Figure 3-1: Theoretical interpretation of DSMC and IP-DSMC simulation molecules

accessible, the macroscopic flow quantities are, and may be used to initialize the IP molecules. As the molecules move (with the DSMC velocity) they transport these quantities, propagating them by both movement and collisions.

The accuracy of the method will depend heavily on the choice of preserved quantities and the manner in which they are updated. As previously noted, the "microscopic average" for sampling a macroscopic quantity $\boldsymbol{Q}$ from the microscopic is

$$\overline{\boldsymbol{Q}} = \frac{1}{N_\mu} \sum_{i=1}^{N_\mu} \boldsymbol{Q}_i \tag{3.4}$$

where N_μ is the total number of real molecules in a control volume. Consider now that these are grouped into N sets of N_μ/N molecules, the quantities for each of these groups

could be sampled by a "local average":

$$\{\boldsymbol{Q}\} = \frac{N}{N_\mu} \sum_{i=1}^{N_\mu/N} \boldsymbol{Q}_i \tag{3.5}$$

Now the "group average" samples the local averages, hopefully recovering the same quantity as the microscopic average.

$$\langle \boldsymbol{Q} \rangle = \frac{1}{N} \sum_{i=1}^{N} \boldsymbol{Q}_i \tag{3.6}$$

The first preserved quantity of interest, as illustrated by the preceding error analysis, is velocity. The microscopic average yields the expected result

$$\overline{\boldsymbol{c}} = \frac{1}{N_\mu} \sum_{i=1}^{N_\mu} \boldsymbol{c}_i = \boldsymbol{c}_0 \tag{3.7}$$

If we now define the IP velocity $\boldsymbol{V}_i$ to be the preserved average of the group of real molecules represented by the i-th particle.

$$\boldsymbol{V}_i \equiv \{\boldsymbol{c}_j\} = \frac{N}{N_\mu} \sum_{j=1}^{N_\mu/N} \boldsymbol{c}_j \tag{3.8}$$

Sampling the IP Velocities, we find that if the individual IP Velocities do indeed represent the local averages, then it is possible to recover the true stream velocity.

$$\langle \boldsymbol{V}_i \rangle = \frac{1}{N} \sum_{i=1}^{N} \boldsymbol{V}_i = \frac{1}{N} \sum_{i=1}^{N} \left[\frac{N}{N_\mu} \sum_{j=1}^{N_\mu/N} \boldsymbol{c}_j \right] = \frac{1}{N_\mu} \sum_{i=1}^{N} \sum_{j=1}^{N_\mu/N} \boldsymbol{c}_j = \frac{1}{N_\mu} \sum_{i=1}^{N_\mu} \boldsymbol{c}_i = \boldsymbol{c}_0 \tag{3.9}$$

This was the basis of the early IP-DSMC [31, 22], but used alone requires that isothermal flow conditions be assumed. If temperature is now considered, the microscopic average yields

$$\frac{3}{2} R\, T_{tr} = \frac{1}{2} \overline{c'^2} = \frac{1}{2} \left(\overline{c^2} - c_0^2 \right) \tag{3.10}$$

where $\boldsymbol{c}' \equiv \boldsymbol{c} - \boldsymbol{c}_0$. Likewise, the IP temperature may be defined in terms of the local average as

$$\begin{aligned} \frac{3}{2} R\, T_{IP,i} &\equiv \frac{1}{2}\{c'''^2\} && (3.11) \\ &= \frac{1}{2}\{(\boldsymbol{c} - \boldsymbol{V}_i)^2\} \\ &= \frac{1}{2}\{c^2 - 2c \cdot V + V^2\} \\ &= \frac{1}{2}\left(\{c^2\} - 2\{c\} \cdot V + V^2\right) \\ &= \frac{1}{2}\left(\{c^2\} - V^2\right)) && (3.12) \end{aligned}$$

where $\boldsymbol{c}''' \equiv \boldsymbol{c} - \boldsymbol{V}$ is the thermal velocity relative to the IP velocity and the following equations demonstrate that temperature can indeed be preserved correctly by this choice of preserved quantities ($\boldsymbol{V}$, T_{IP}).

$$\begin{aligned} \frac{3}{2} R\, T_{IP} &= \frac{3}{2} R \langle T_{IP,i} \rangle + \frac{1}{2}\langle V'^2 \rangle && (3.13) \\ &= \frac{1}{2}\langle \{c^2\} - V^2 \rangle + \frac{1}{2}\langle (\boldsymbol{V} - \boldsymbol{c}_0)^2 \rangle \\ &= \frac{1}{2}\langle \{c^2\} - V^2 + V^2 - 2\boldsymbol{V} \cdot \boldsymbol{c}_0 + c_0^2 \rangle \\ &= \frac{1}{2}\langle \{c^2\} \rangle - c_0^2 \\ &= \frac{1}{2}\left(\overline{c^2} - c_0^2\right) && (3.14) \end{aligned}$$

or

$$T_{IP} = \frac{1}{3R}\left(\overline{c^2} - c_0^2\right) = \frac{1}{3R}\overline{c'^2} \qquad (3.15)$$

The microscopic definition of scalar pressure is

$$p = \frac{1}{3}\rho\left(\overline{c_x'^2 + c_y'^2 + c_z'^2}\right) = \frac{1}{3}\rho\overline{c'^2} \qquad (3.16)$$

which, as expected, is related to the temperature (Ideal Gas law), and shows that the scalar pressure may be preserved correctly by this set of preserved quantities.

$$P_{ip} = \rho_{IP} R\, T_{IP} \qquad (3.17)$$

Thus far, the preserved quantities—including the preserved density ρ_{IP} which will be discussed later—are all collision invariants, meaning that when two (or more) particles are involved in a collision, the mass, center of mass momentum, and energy are conserved, *i.e.*,

$$\sum_{i=1}^{N} m_i^\star = \sum m_i \tag{3.18}$$

$$\frac{1}{N}\sum_{i=1}^{N} m_i^\star \boldsymbol{c}_i^\star = \frac{1}{N}\sum_{i=1}^{N} m_i \boldsymbol{c}_i \tag{3.19}$$

$$\frac{1}{N}\sum_{i=1}^{N}\left[\frac{1}{2}m_i^\star {c_i^\star}^2 + \varepsilon^\star\right] = \frac{1}{N}\sum_{i=1}^{N}\left[\frac{1}{2}m_i {c_i}^2 + \varepsilon\right] \tag{3.20}$$

where the superscript * indicates post-collision quantities and ε represents the internal energy (rotational or vibrational—for a monatomic gas $\varepsilon \equiv 0$). If the preserved quantities can be limited to collision invariants this will greatly simplify the requirements for the collision and transport models. However, for complete modeling of flow conditions, the pressure (or stress) tensor and the heat flux are needed.

The stress or pressure tensor is defined as

$$\boldsymbol{\sigma} = \rho\overline{\boldsymbol{c}'\boldsymbol{c}'} = \rho\overline{\boldsymbol{c}\boldsymbol{c}} - \rho\overline{\boldsymbol{c}_0'\boldsymbol{c}_0'} \tag{3.21}$$

$$= \rho\begin{bmatrix} \overline{c_x'c_x'} & \overline{c_x'c_y'} & \overline{c_x'c_z'} \\ \overline{c_y'c_x'} & \overline{c_y'c_y'} & \overline{c_y'c_z'} \\ \overline{c_z'c_x'} & \overline{c_z'c_y'} & \overline{c_z'c_z'} \end{bmatrix} = \rho\begin{bmatrix} \overline{c_xc_x} & \overline{c_xc_y} & \overline{c_xc_z} \\ \overline{c_yc_x} & \overline{c_yc_y} & \overline{c_yc_z} \\ \overline{c_zc_x} & \overline{c_zc_y} & \overline{c_zc_z} \end{bmatrix} - \rho\begin{bmatrix} \overline{c_{0x}c_{0x}} & \overline{c_{0x}c_{0y}} & \overline{c_{0x}c_{0z}} \\ \overline{c_{0y}c_{0x}} & \overline{c_{0y}c_{0y}} & \overline{c_{0y}c_{0z}} \\ \overline{c_{0z}c_{0x}} & \overline{c_{0z}c_{0y}} & \overline{c_{0z}c_{0z}} \end{bmatrix} \tag{3.22}$$

Looking at a single term $\overline{c_i'c_j'} = \overline{c_ic_j} - c_{0i}c_{0j}$, one may observe that the second term on the right hand side is readily available in terms of the preserved quantities ($c_{0i}c_{0j} = \langle V_i\rangle\langle V_j\rangle$). However, the remaining term cannot be recovered from direct sampling of the preserved velocity and temperature. Consequently, the viscous shear ($\boldsymbol{\tau} \equiv \tau_{ij} = -\left(\rho\overline{c_i'c_j'} - \delta_{ij}p\right)$) is not preserved either.

The heat flux is defined as

$$
\begin{aligned}
q_i &= \frac{1}{2}\rho\overline{c'^2 c_i'} + n\overline{\varepsilon_{int} u'} && (3.23)\\
&= \frac{1}{2}\rho\overline{(\boldsymbol{c}-\boldsymbol{c}_0)^2 (c_i - c_{0i})}\\
&= \frac{1}{2}\rho\overline{\left(c_j c_j - 2c_j c_{0j} + c_{0j}c_{0j}\right)(c_i - c_{0i})}\\
&= \frac{1}{2}\rho\left(\overline{c_j c_j c_i - 2c_j c_{0j} c_i + c_{0j}c_{0j}c_i - c_j c_j c_{0i} + 2c_j c_{0j} c_{0i} - c_{0j}c_{0j}c_{0i}}\right)\\
&= \frac{1}{2}\rho\left[\overline{c_j c_j c_i} - \overline{c_j c_j} c_{0i} - 2\left(\overline{c_i c_j} c_{0j} - c_{0i}\overline{c_j} c_{0j}\right) + c_{0j}c_{0j}\left(\overline{c_i} - c_{0i}\right)\right]\\
&= \frac{1}{2}\left[\rho\left(\overline{c^2 c_i} - \overline{c^2} c_{0i}\right) - 2p_{ij}c_{0j}\right] && (3.24)
\end{aligned}
$$

where ε_{int} represents the internal energy of the molecules ($\varepsilon_{int} \equiv 0$ for monatomic gases). $c_{0i}\overline{c^2}$ is preserved by a combination of the preserved velocity and temperature. The remaining terms cannot be expressed in terms of the current set of preserved quantities, requiring the currently unavailable pressure tensor and an additional term $\overline{c^2 c_i}$. Although these quantities are not available via direct sampling, they are both transport quantities, *i.e.*, the pressure tensor represents the average momentum flux and the heat flux represents the average energy flux. More specifically, p_{ij} is j-th component of momentum transported in the i-th dimension per unit area, and q_i is the energy transported in the i-th dimension per unit area. As such it may be possible to recover this information from a combination of the preserved data and the transport formulation which will be addressed in the following section.

3.2.2 Transport

In addition to correctly representing the macroscopic state, the IP-DSMC must also correctly represent the transport of mass, momentum, and energy. A number of attempts, some more formal than others, have been made to develop a correct set of transport equations for the IP-DSMC, and thus a means of updating the preserved quantities of density, velocity and temperature as the flow progresses. One formulation relied on an "additional" energy (or temperature) carried by each particle[99, 100] to reflect the discrepancy between the average energy of a particle within a stationary distribution ($E = 3\,k_B\,T/2$) and the average

energy of a particle from such a distribution that crosses an interface ($E = 2\,k_B\,T$). In this method, particles leaving a cell "borrowed" a certain amount of thermal energy from the particles remaining in the cell. This "additional energy" was then carried and eventually added to the particle's temperature. Momentum updates were based, in an *ad hoc* fashion, on the macroscopic pressure gradient obtained from sampling the IP data. This method demonstrated considerable success for a number of cases, including high-speed and thermal Couette flow, and flow around a micro-airfoil [100, 99]. Later works sought to extend the method to non-equilibrium systems by utilizing kinetic flux equations [94, 108].

Recently Sun and Boyd [101] presented a formulation for the transport of preserved quantities derived from the Boltzmann Transport Equation (BTE). The Boltzmann transport equation states that the time rate of change of a quantity $\boldsymbol{Q}$ may be expressed in terms of the gradient of the transport of the quantity and the effect of collisions on the quantity, *i.e.*,

$$\frac{\partial}{\partial t}\overline{\boldsymbol{Q}} + \nabla \cdot \left(\overline{\boldsymbol{c}\boldsymbol{Q}}\right) = \Delta\left[\boldsymbol{Q}\right] \tag{3.25}$$

where $\Delta\left[\overline{\boldsymbol{Q}}\right]$ is the collision integral (or operator) for the transported quantity and $\Delta\left[\overline{\boldsymbol{Q}}\right] \equiv 0$ for collision invariants. Applying the BTE to the collision invariants of mass, momentum, and energy one obtains:

$$\frac{\partial}{\partial t}\left(nm\right) + \nabla \cdot \left(nm\overline{\boldsymbol{c}}\right) = \Delta\left[nm\right] \tag{3.26}$$

$$\frac{\partial}{\partial t}\left(nm\overline{\boldsymbol{c}}\right) + \nabla \cdot \left(nm\overline{\boldsymbol{c}\boldsymbol{c}}\right) = \Delta\left[nm\overline{\boldsymbol{c}}\right] \tag{3.27}$$

$$\frac{\partial}{\partial t}\left(\frac{1}{2}nm\overline{c^2}\right) + \nabla \cdot \left(\frac{1}{2}nm\overline{\boldsymbol{c}c^2}\right) = \Delta\left[\frac{1}{2}nm\overline{c^2}\right] \tag{3.28}$$

$$\tag{3.29}$$

From the transport equations Sun and Boyd derived a set of so-called "Correlation Coefficients" for momentum and energy transport [101]. Beginning with mass transport, the derivations are as follows:

$$\frac{\partial}{\partial t}\left(\rho\right) = -\nabla \cdot \left(\rho\overline{\boldsymbol{c}}\right) + \Delta\left[\rho\right] \tag{3.30}$$

which may be expressed in terms of the preserved velocity $\overline{\boldsymbol{V}} = \overline{\boldsymbol{c}} = \boldsymbol{c}_0$

$$\frac{\partial}{\partial t}(\rho) = -\nabla \cdot \left(\rho \overline{\boldsymbol{V}}\right) + \text{collision} \tag{3.31}$$

As the mass transport depends only on the average cell velocity, it can be preserved as a cell quantity.

The transport equation for momentum is

$$\frac{\partial}{\partial t}(\rho \overline{\boldsymbol{c}}) = -\nabla \cdot (\rho \overline{\boldsymbol{c}\boldsymbol{c}}) + \Delta\left[\rho \overline{\boldsymbol{c}}\right] \tag{3.32}$$

Sun and Boyd then made the following substitution $\overline{\boldsymbol{c}\boldsymbol{c}} = \overline{(\boldsymbol{c}''' + \boldsymbol{V})(\boldsymbol{c}' + \boldsymbol{c}_0)}$ and simplified to obtain

$$\frac{\partial}{\partial t}\left(\rho \overline{\boldsymbol{V}}\right) + \nabla \cdot \left(\rho \overline{\boldsymbol{V}\boldsymbol{c}}\right) = -\nabla \cdot \left(\rho \overline{\boldsymbol{c}'''\boldsymbol{c}'}\right) + \Delta\left[\rho \overline{\boldsymbol{c}}\right] \tag{3.33}$$

or, after recognizing that the movement of the particles with the microscopic (DMSC) velocities accounts for the quantity $\overline{\boldsymbol{V}\boldsymbol{c}}$,

$$\frac{\partial}{\partial t}\left(\rho \overline{\boldsymbol{V}}\right) + \text{movement} = -\nabla \cdot \left(\rho \overline{\boldsymbol{c}'''\boldsymbol{c}'}\right) + \text{collision} \tag{3.34}$$

From the cited work, it appears that $\overline{\boldsymbol{c}\boldsymbol{c}}$ may be replaced by either $\overline{\boldsymbol{c}'''\boldsymbol{c}'} + \overline{\boldsymbol{V}\boldsymbol{c}}$ or $\overline{\boldsymbol{c}'\boldsymbol{c}'''} + \overline{\boldsymbol{c}\boldsymbol{V}}$. However, during the present work, it has become apparent that the order is important and that the choice made by Sun and Boyd is incorrect. The correct formulation should be

$$\frac{\partial}{\partial t}\left(\rho \overline{\boldsymbol{V}}\right) + \nabla \cdot \left(\rho \overline{\boldsymbol{c}\boldsymbol{V}}\right) = -\nabla \cdot \left(\rho \overline{\boldsymbol{c}'\boldsymbol{c}'''}\right) + \Delta\left[\rho \overline{\boldsymbol{c}}\right] \tag{3.35}$$

and

$$\frac{\partial}{\partial t}\left(\rho \overline{\boldsymbol{V}}\right) + \text{movement} = -\nabla \cdot \left(\rho \overline{\boldsymbol{c}'\boldsymbol{c}'''}\right) + \text{collision} \tag{3.36}$$

The physical interpretation of this is that the transport of any preserved quantities in the i-th dimension due to the particle motion depends on the microscopic or DSMC velocity c_i. Thus, the movement term must be $\overline{c_i V_j}$ and for consistency the remaining term will be $\overline{c_i' c_j'''}$.

Finally the transport equation for energy (assuming a monatomic gas) is

$$\frac{\partial}{\partial t}\left(\frac{1}{2}\rho \overline{c^2}\right) = -\nabla \cdot \left(\frac{1}{2}\rho \overline{\boldsymbol{c}c^2}\right) + \Delta\left[\frac{1}{2}\rho \overline{c^2}\right] \tag{3.37}$$

From Eq. (3.12) $\overline{c^2} = \overline{V^2 + 3\,R\,T}$, which may be used to obtain

$$\frac{\partial}{\partial t}\left(\frac{1}{2}\rho\,\overline{(V^2 + 3\,R\,T)}\right) + \nabla\cdot\left(\frac{1}{2}\rho\overline{\boldsymbol{c}\,(V^2 + 3\,R\,T)}\right) = \nabla\cdot\left(\frac{1}{2}\rho\overline{\boldsymbol{c}'\,(V^2 + 3\,R\,T - c^2)}\right) + \Delta\left[\frac{1}{2}\rho\overline{c^2}\right] \tag{3.38}$$

or

$$\frac{\partial}{\partial t}\left(\frac{1}{2}\rho\,\overline{(V^2 + 3\,R\,T)}\right) + \text{movement} = \nabla\cdot\left(\frac{1}{2}\rho\overline{\boldsymbol{c}'\,(V^2 + 3\,R\,T - c^2)}\right) + \text{collision} \tag{3.39}$$

The collision terms are retained only as a reminder that collisions are part of the method. Likewise, the "movement" terms are treated by the movement of the simulation molecules. In both the momentum and energy transport equations, the remaining terms on the RHS are the correlation coefficients. Sun and Boyd proposed two models to evaluate the correlation coefficients: The Local Thermal Equilibrium (LTE) and the Flux Splitting methods. Both of these are based on the assumption that the real molecules represented by each simulation molecule follow some distribution as a function of the preserved temperatures and velocities and that actual distribution of the cell may be described in terms of these separate distributions. The distribution for each simulation molecule may be integrated to obtain the average quantities necessary for the correlation coefficients. The LTE model assumes that each molecule is in local thermal equilibrium, *i.e.*, that it can be described by an equilibrium (Maxwellian) distribution

$$f_{LTE} = \frac{\beta^3}{\pi^{3/2}} e^{-\beta^2(\boldsymbol{c}-\boldsymbol{V})^2} \tag{3.40}$$

where $\boldsymbol{V}$ is the preserved velocity of the current molecule, and $\beta = (2\,R\,T)^{-1/2}$ is a function of the preserved temperature of the molecule (β is the inverse of the most probable velocity *i.e.*, $\beta = 1/c_{mp}$). In practice, Sun and Boyd found the LTE method to be inadequate for modeling even 1D thermal Couette flow.

The Flux Splitting method seeks to include certain non-equilibrium characteristics of the flow. Instead of treating each molecule as an equilibrium distribution, the molecules

and their correlation coefficients are split based on their microscopic (DSMC) velocities, treating each particle as a half-Maxwellian in the splitting direction. Upon further analysis of the Flux Splitting method Sun and Boyd recognized that the earlier "Additional Energy" method [100, 99] is a special case of the Flux Splitting method. The splitting of the correlation coefficients splits the flux in each dimension into positive or negative flux with respect to some splitting velocity (usually the stream velocity, $\boldsymbol{c}_0$). The correlation coefficients for each molecule are then evaluated over the velocity half-space designated by the splitting direction. The correlation coefficients for all the particles in each splitting group are then averaged over the particles in each group and these split averages are added together to form the complete correlation coefficients:

$$\overline{\boldsymbol{Q}_k} = \frac{\sum_i \delta\left(c_{i,k} > a_k\right) \iiint_{c_k > a_k} \boldsymbol{Q}_k f_{LTE,i}\, \mathrm{d}\boldsymbol{c}}{\sum_i \delta\left(c_{i,k} > a_k\right)} + \frac{\sum_i \delta\left(c_{i,k} < a_k\right) \iiint_{c_k < a_k} \boldsymbol{Q}_k f_{LTE,i}\, \mathrm{d}\boldsymbol{c}}{\sum_i \delta\left(c_{i,k} < a_k\right)} \tag{3.41}$$

Equations 3.42 and 3.43 summarize the Flux Splitting correlation coefficients for momentum and energy flux, respectively, where "$\overset{k}{\pm}$" represents a change of sign dependent on the splitting direction: positive for $c_k > a_k$ and negative for $c_k < a_k$. Similarly, "$\overset{k}{\mp}$" represents the opposite relationship ($\left(\overset{k}{\mp}\right) = -\left(\overset{k}{\pm}\right)$). The limits of integration are from $(-\infty \to \infty)$ for the non-splitting directions (perpendicular to the splitting direction) and from $(a_k \to \infty)$ for positive splitting $(c_k > a_k)$ and from $(-\infty \to a_k)$ for negative splitting.

$$\begin{aligned}
\overline{c'_k\, c'''_j} &= \frac{\beta^3}{\pi^{3/2}} \iiint_{c_k \gtrless a_k} \left(c_k - c_{0k}\right)\left(c_j - V_k\right) e^{-\beta^2 (\boldsymbol{c}-\boldsymbol{V})^2}\, \mathrm{d}\boldsymbol{c} \\
&= \begin{cases} \frac{\left(1 \overset{k}{\pm} \mathrm{erf}(\beta\,(V_k - a_k))\right)}{4\beta^2} \overset{k}{\mp} \frac{\left(c_{0j} - a_j\right) e^{-\beta^2 (V_k - a_k)^2}}{2\sqrt{\pi}\beta}, & j = k \\ 0, & j \neq k \end{cases}
\end{aligned} \tag{3.42}$$

$$\begin{aligned}
\overline{\left(V^2 + 3\,R\,T - c^2\right) c'_k|} &= \frac{\beta^3}{\pi^{3/2}} \iiint_{c_k \gtrless a_k} \left(V^2 + 3\,R\,T - c^2\right)\left(c_k - c_{0k}\right) e^{-\beta^2 (\boldsymbol{c}-\boldsymbol{V})^2}\, \mathrm{d}\boldsymbol{c} \\
&= -R\,T\,V_k \left(1 \pm \mathrm{erf}\left(\beta\,\left(V_k - a_k\right)\right)\right) \overset{k}{\mp} \frac{e^{-\beta^2 (V_k - a_k)^2}}{2\sqrt{\pi}\beta} \left[R\,T - \left(V_k + a_k\right)\left(c_{0k} - a_k\right)\right]
\end{aligned} \tag{3.43}$$

Sun and Boyd do not discuss sampling techniques for shear and heat flux in the cited work, but earlier studies do present "particle counting" techniques, wherein the momentum and energy of simulation particles are sampled when crossing cell interfaces [99]. These take the form of:

$$\tau_{ij} = \frac{\sum m\left(V_{x,i}^{in} - V_{x,j}^{ex}\right)}{\Delta t \Delta A} \tag{3.44}$$

$$q_i = \frac{\sum\left(\frac{1}{2}mV_i^2 + \frac{3}{2}k\left(T_i + T_{a,i}\right)^{in} - \left(\frac{1}{2}mV_j^2 + \frac{3}{2}k\left(T_j + T_{a,j}\right)\right)^{ex}\right)}{\Delta t \Delta A} \tag{3.45}$$

where $T_{a,i}$ and $T_{a,j}$ are the *additional temperatures* for the particles, the superscripts *in* and *ex* refer to particles entering and exiting the cell, Δt is the time step, and ΔA is the area of the cell face.

However, one may observe that the correlation coefficients may be used as part of the sampling technique. Consider the definition of the pressure tensor given in Table 2-1:

$$\boldsymbol{\sigma} = \rho\overline{\boldsymbol{c}\boldsymbol{c}} - \rho\boldsymbol{c}_0'\boldsymbol{c}_0' \tag{3.46}$$

and from Eq. (3.35)

$$\rho\overline{\boldsymbol{c}\boldsymbol{c}} = \rho\overline{\boldsymbol{c}\boldsymbol{V}} + \rho\overline{\boldsymbol{c}'\boldsymbol{c}'''} \tag{3.47}$$

Thus the complete pressure tensor may be reconstructed by sampling the mixed (DSMC and IP-DSMC) quantity

$$\overline{\boldsymbol{c}\boldsymbol{V}} = \frac{1}{N}\sum \boldsymbol{c}\boldsymbol{V} \tag{3.48}$$

and combining this with the correlation coefficient, yielding

$$\boldsymbol{\sigma} = \rho\overline{\boldsymbol{c}\boldsymbol{V}} + \rho\overline{\boldsymbol{c}'\boldsymbol{c}'''} - \rho\boldsymbol{c}_0'\boldsymbol{c}_0' \tag{3.49}$$

The averages shown here are over all the particles in each computational cell in a given time step and may then be accumulated to form the time ensemble averages of the macroscopic quantities. The erroneous form of the momentum correlation coefficient ($\overline{\boldsymbol{c}'''\boldsymbol{c}'}$) was identified during the formulation of this sampling technique.

In a similar manner, the heat flux may be constructed from sampled quantities, the correlation coefficients, and the now complete pressure tensor

$$q_i = \frac{1}{2}\left[\rho\left(\overline{c_i c^2} - c_{0i}\overline{c^2}\right) - 2p_{ij}c_{0j}\right] \tag{3.50}$$

$$= \frac{\rho\left[\left(\overline{c\left(V^2+3RT\right)} - \overline{c'\left(V^2+3RT-c^2\right)}\right) - c_{0i}\overline{\left(V^2+3RT\right)}\right]}{2} - p_{ij}c_{0j} \tag{3.51}$$

where

$$\overline{c\left(V^2+3RT\right)} = \frac{1}{N}\sum \boldsymbol{c}\left(V^2+3RT\right) \tag{3.52}$$

and

$$\overline{\left(V^2+3RT\right)} = \frac{1}{N}\sum \left(V^2+3RT\right) \tag{3.53}$$

Thus all of the usual macroscopic quantities have either been preserved directly or recovered by sampling mixed DSMC/IP-DSMC and correlation coefficient quantities. There are a number of implicit assumptions that should be noted:

- Preserving the scalar temperature, T_{IP}, assumes that the velocity distributions of the particles represented by the IP molecule are isotropic, *i.e.*, $T_x = T_y = T_z$
- The Maxwellian distributions, albeit split into half-spaces, are consistent with the previous assumption
- Each IP particle represents an equilibrium distribution, but the individual particles are not necessarily in equilibrium with each other. Furthermore, the velocity distribution of the cell cannot, in general, be described by the Maxwellian distribution.

3.2.3 Modification Step: Finite Volume Method

Most IP-DSMC methods have utilized a Finite Volume Method update scheme to apply the effects of transport quantities, *e.g.*, early models applied the effect of pressure gradients to accelerate the molecules [22, 94, 100]. The Finite Volume Method provides a conservative integral form of the (differential) transport equations. The FVM formulation for a

differential equation of the form

$$\frac{\partial}{\partial t}(\boldsymbol{Q}) = -\nabla \cdot (\boldsymbol{F}(\boldsymbol{x}, \boldsymbol{c}, t)) \tag{3.54}$$

may be derived by integrating both sides of the equation over the control volume Ω.

$$\int_{\Omega} \frac{\partial}{\partial t}(\boldsymbol{Q})\, \mathrm{d}\Omega = -\int_{\Omega} \nabla \cdot (\boldsymbol{F}(\boldsymbol{x}, \boldsymbol{c}, t))\, \mathrm{d}\Omega \tag{3.55}$$

Recognizing that $\partial \boldsymbol{Q}/\partial t$ is independent of the volume integration and applying Green's theorem to the RHS:

$$\frac{\partial}{\partial t}(\boldsymbol{Q}) \int_{\Omega} \mathrm{d}\Omega = -\oint_{S} (\boldsymbol{F}(\boldsymbol{x}, \boldsymbol{c}, t)) \cdot \boldsymbol{n}\, \mathrm{d}S \tag{3.56}$$

$$\frac{\partial}{\partial t}(\boldsymbol{Q}) = -\frac{1}{\Omega} \oint_{S} (\boldsymbol{F}(\boldsymbol{x}, \boldsymbol{c}, t)) \cdot \boldsymbol{n}\, \mathrm{d}S \tag{3.57}$$

Discretizing the LHS, and multiplying both sides by Δt, one obtains the general FVM formulation in terms of the surface integral on the RHS:

$$\frac{\Delta \boldsymbol{Q}}{\Delta t} = -\frac{1}{\Omega} \oint_{S} (\boldsymbol{F}(\boldsymbol{x}, \boldsymbol{c}, t)) \cdot \boldsymbol{n}\, \mathrm{d}S \tag{3.58}$$

$$\Delta \boldsymbol{Q} = -\frac{\Delta t}{\Omega} \oint_{S} (\boldsymbol{F}(\boldsymbol{x}, \boldsymbol{c}, t)) \cdot \boldsymbol{n}\, \mathrm{d}S \tag{3.59}$$

For the Cartesian rectilinear cells used in this study, the RHS may be expressed in terms of the surface areas of the cell faces and their outward normals (in lower dimensions the cells still have an effective volume and surfaces), yielding:

$$\Delta \boldsymbol{Q} = -\frac{\Delta t}{\Omega} \left[\sum_{i=1}^{D} (\boldsymbol{F}(\boldsymbol{x}, \boldsymbol{c}, t)|_{+} - \boldsymbol{F}(\boldsymbol{x}, \boldsymbol{v}, t)|_{-})_i\, S_i \right] \tag{3.60}$$

where D is the dimensionality of the simulation, S_i is the surface area of the cell face in the i-th dimension, and the remaining terms represent the value of the function $\boldsymbol{F}(\boldsymbol{x}, \boldsymbol{v}, t)$ at the top and bottom surfaces (+ and −) with respect to the i-th dimension. We can now discretize the LHS in time, assume that the modification is uniformly applied, *i.e.*, $\Delta\overline{\boldsymbol{Q}} = \Delta \boldsymbol{Q}_i$ for each

particle, and apply this to the transport coefficients:

$$\rho^{t+\Delta t} - \rho^t = -\frac{\Delta t}{\Omega}\left[\sum_{i=1}^{D}\left(\left(\rho\,\overline{V}_i\right)|_+ - \left(\rho\,\overline{V}_i\right)|_-\right)_i S_i\right] \tag{3.61}$$

$$(\rho \boldsymbol{V})^{t+\Delta t} - (\rho \boldsymbol{V})^t = -\frac{\Delta t}{\Omega}\left[\sum_{i=1}^{D}\left(\left(\rho\,\overline{c_i'''\boldsymbol{c}'}\right)|_+ - \left(\rho\overline{c_i'''\boldsymbol{c}'}\right)|_-\right)_i S_i\right] \tag{3.62}$$

$$\left(\frac{\rho\left(V^2+3RT\right)}{2}\right)^{t+\Delta t} - \left(\frac{\rho\left(V^2+3RT\right)}{2}\right)^{t} = \frac{\Delta t}{\Omega}\left[\sum_{i=1}^{D}\left\{\begin{array}{l}\left(\frac{1}{2}\rho\,\overline{\left(V^2+3RT-c^2\right)c_i'}\right)|_+ \\ \qquad -\left(\frac{1}{2}\rho\overline{\left(V^2+3RT-c^2\right)c_i'}\right)|_-\end{array}\right\}_i S_i\right] \tag{3.63}$$

As the IP quantities are all sampled at the cell centroid, some sort of interpolation scheme is needed to approximate the quantities at the cell interfaces. A QUICK (Quadratic Upstream Interpolation for Convective Kinematics) scheme is used for the interpolations for mass transport. This technique, borrowed from conventional FVM practice, avoids non-physical oscillations, or *wiggles*, that may arise from simpler schemes, *e.g.*, Central Difference [58]. QUICK uses a three point quadratic interpolation with the points chosen based on the stream (flow velocity) direction. In the following formula, the quantities for the downstream and the two upstream cells are identified by the subscripts "D", "U", and "UU", respectively. Thus at each face, the flow direction is used to determine which cells are upstream and downstream, and the interpolation is

$$Q = \frac{1}{8}\left(-Q_{UU} + 6Q_U + 3Q_D\right) \tag{3.64}$$

A further enhancement, which insures that the quantities used in the interpolation are monotonic, is the UMIST (Upstream Monotonic Interpolation for Scalar Transport) scheme [60] which contains the QUICK update but reverts to a purely upstream update

if the quantities are not monotonic. This is the scheme currently implemented in the GT-DSMC.

$$r = \frac{\rho_U - \rho_{UU}}{\rho_D - \rho_U} \tag{3.65}$$

$$\rho_{face} = \begin{cases} \rho_U + (\rho_D - \rho_U)\min\left(r, \left(\frac{1}{8} + \frac{3}{8}r\right), \left(\frac{3}{8} + \frac{1}{8}r\right), 1\right) & \text{if monotone} \\ \rho_U & \text{otherwise} \end{cases} \tag{3.66}$$

$$V_{face} = \frac{V_U + V_D}{2} \tag{3.67}$$

Where the min function may also be expressed as a function of r

$$\min\left(r, \left(\frac{1}{8} + \frac{3}{8}r\right), \left(\frac{3}{8} + \frac{1}{8}r\right), 1\right) = \begin{cases} r & \text{if } 0 < r \leq 0.2 \\ \frac{1}{8} + \frac{3}{8}r & \text{if } 0.2 < r \leq 0.5 \\ \frac{3}{8} + \frac{1}{8}r & \text{if } 0.5 < r \leq 5 \\ 1 & \text{if } r > 5 \end{cases} \tag{3.68}$$

3.2.4 Particle Modification

The result of the Finite Volume Method is a modification $\Delta\boldsymbol{Q} = \boldsymbol{Q}_{t+\Delta t} - \boldsymbol{Q}_t$, for the preserved quantities of density, velocity, and temperature, where the $\Delta\boldsymbol{Q}$ comes from the right hand sides of Equations (3.61)-(3.63). The density is preserved and updated on a cell basis:

$$\rho_{t+\Delta t} = \rho_t + \Delta\rho \tag{3.69}$$

The others quantities are applied to each particle. In practice, the ideal updates in Equations (3.62) and (3.63) may lead to numerical instability and non-physical values due to statistical fluctuations. Consequently, a modified form that replaces the densities ρ^t and

$\rho^{t+\Delta t}$ with the mass represented by the particles in the cell is used, thus.

$$(\boldsymbol{V})^{t+\Delta t} = (\boldsymbol{V})^{t} - \frac{\Delta t}{NF_N m}\left[\sum_{i=1}^{D}\left(\left(\rho\,\overline{c_i'''\boldsymbol{c}'}\right)|_{+} - \left(\rho\overline{c_i'''\boldsymbol{c}'}\right)|_{-}\right)_i S_i\right] \tag{3.70}$$

$$(T)^{t=\Delta t} = (T)^{t} + \frac{1}{3R}\left(\left(V^2\right)^{t} - \left(V^2\right)^{t+\Delta t}\right) \tag{3.71}$$

$$+\frac{2\Delta t}{3RNF_N m}\left[\sum_{i=1}^{D}\left\{\begin{array}{l}\left(\frac{1}{2}\rho\,\overline{\left(V^2+3RT-c^2\right)c_i'}\right)|_{+} \\ \qquad -\left(\frac{1}{2}\rho\overline{\left(V^2+3RT-c^2\right)c_i'}\right)|_{-}\end{array}\right\}_i S_i\right]$$

The first step then is to update the density of the cell, followed by the velocities of each particle in the cell. This new velocity is then used along with the FVM to update the temperature in Eq. (3.72), balancing kinetic and thermal energy. During these updates, it is possible (especially in highly rarefied flows) for the momentum modification to be quite large. This may result in a negative preserved temperature—which is physically and numerically inadmissible. In order to correct such cases, the updates must be checked for validity. If the resulting temperature is negative, then the first step is to convert some of the kinetic energy of the particle into thermal energy. This *thermalization* is accomplished by setting the particle velocity to some fraction of its current value *i.e.*, $\boldsymbol{V}^{\star} = \alpha\boldsymbol{V}$. The kinetic energy associated with this can then be converted to thermal energy:

$$T^{\star}_{t+\Delta t} = T_{t+\Delta t} + \frac{1}{3R}\left(V^2 - V^{\star 2}\right) \tag{3.72}$$

The total momentum of the cell must be preserved, therefore the velocity that is thermalized must be distributed to all of the particles, requiring an additional update step, as follows:

$$(\boldsymbol{V})^{C} = \boldsymbol{V}_{t+\Delta t} + \frac{1}{N}\boldsymbol{V}^{\star} \tag{3.73}$$

$$(T)^{C} = (T)^{t+\Delta t} + \frac{1}{3R}\left(\left(V^2\right)^{t+\Delta t} - \left(V^2\right)^{C}\right) \tag{3.74}$$

where the superscript C indicates the corrected values. This may need to be repeated, if subsequent corrections fail, but usually not more than 20 times. In some cases, particularly in modeling free molecular flows, particles may develop large preserved velocities,

relative to the average cell velocity, and consequently have low preserved temperatures (in effect, the IP-DSMC is reverting to the DSMC). In such cases, it may be advantageous to thermalize all the particles within a cell. Such conditions may be detected by comparing the average preserved temperature of the particles within a cell ($T = \overline{T_i}$) to the preserved temperature of the cell, which includes the peculiar kinetic energy $T_c = \overline{T_i} + 1/3R(\overline{V_i^2} - \overline{V}^2)$. A cutoff of $T_c/T > 1.005$

3.2.5 Collision Model

The transport of real and preserved quantities also depends on intermolecular interactions or collisions. A number of *ad hoc* IP collision models of post-collision interchange of preserved quantities have been proposed in the literature, all relying on the DSMC for the selection of the collision pairs. The earliest collision model (for isothermal flows) simply conserved the center of mass IP momentum [31, 32]

$$\boldsymbol{V}_1'' = \frac{\boldsymbol{V}_1' + \boldsymbol{V}_2'}{2} \tag{3.75}$$

$$\boldsymbol{V}_2'' = \frac{\boldsymbol{V}_1' + \boldsymbol{V}_2'}{2} \tag{3.76}$$

This leads to quickly convergent velocity fields, but was inadequate for non-isothermal flows—as this model converts all relative velocity components to thermal energy. One proposed solution was to modify the collision cross-sections used in the DSMC simulations [32]. This required modifying the underlying DSMC as well, which is undesirable. Sun proposed a phenomenological collision model, which converts a portion of the relative kinetic energy into thermal energy, based on a number of fitted parameters and the deflection angle, χ of the DSMC molecules [99, 100] (post-collision quantities are indicated by

superscript $\star$):

$$\boldsymbol{V}_1^\star = \frac{1+C_\mu\cos\chi}{2}\boldsymbol{V}_1 + \frac{1-C_\mu\cos\chi}{2}\boldsymbol{V}_2 \tag{3.77}$$

$$\boldsymbol{V}_2^\star = \frac{1-C_\mu\cos\chi}{2}\boldsymbol{V}_1 + \frac{1+C_\mu\cos\chi}{2}\boldsymbol{V}_2 \tag{3.78}$$

$$T_1^\star = \frac{1+C_\kappa\cos\chi}{2}T_1 + \frac{1-C_\kappa\cos\chi}{2}T_2 + \frac{\left(1-C_\mu^2\cos^2\chi\right)}{4\xi R}\|\boldsymbol{V}_1-\boldsymbol{V}_2\|^2 \tag{3.79}$$

$$T_2^\star = \frac{1-C_\kappa\cos\chi}{2}T_1 + \frac{1+C_\kappa\cos\chi}{2}T_2 + \frac{\left(1-C_\mu^2\cos^2\chi\right)}{4\xi R}\|\boldsymbol{V}_1-\boldsymbol{V}_2\|^2 \tag{3.80}$$

where ξ is the number of degrees of freedom for the gas species (3 for monatomic gas), C_μ and C_κ are parameters chosen to provide the best results for simulations of 1D high-speed and thermal Couette flow, respectively. The deflection angle is calculated from the DSMC velocities as

$$\cos\chi = \frac{\boldsymbol{c}_r\cdot\boldsymbol{c}_r^\star}{\|\boldsymbol{c}_r\|\|\boldsymbol{c}_r^\star\|} = \frac{(\boldsymbol{c}_1-\boldsymbol{c}_2)\cdot\left(\boldsymbol{c}_1^\star-\boldsymbol{c}_2^\star\right)}{\|\boldsymbol{c}_1-\boldsymbol{c}_2\|\|\boldsymbol{c}_1^\star-\boldsymbol{c}_2^\star\|} \tag{3.81}$$

Improvements to the collision models would do much for the acceptance of the IP-DSMC. However, Sun's model, presented in Eqs. (3.78)-Eq. (3.81), has performed well in this author's experience and will used in this study. For Argon gas, the collision parameters are $C_\mu = -0.18$, and $C_\kappa = 1.28$.

3.2.6 Treatment of Boundary Conditions

Boundary conditions require special treatment in the IP-DSMC. In the DSMC solid boundaries may be treated quite simply by resetting the velocity of the particle to reflect the accommodation coefficient (α), temperature (T_w), and velocity ($\boldsymbol{V}_w$) of the surface, thus

$$\boldsymbol{c}^\star = \alpha\boldsymbol{c}^d + (1-\alpha)\,\boldsymbol{c}^s \tag{3.82}$$

where the superscripts $\star$, d, and s refer to the assigned post-collision velocity, diffuse velocity, and specular velocity, and α is the accommodation coefficient of the surface ($\alpha = 1$ is fully diffuse and $\alpha = 0$ is specular).

Alternatively, one may use an acceptance rejection scheme, wherein a uniform random number, $\mathcal{R}_u$ is selected for each interacting particle and compared to the accommodation coefficient. If $\mathcal{R}_u > \alpha$ then the particle-wall interaction is treated as specular, otherwise the velocity is assigned as a diffuse interaction. This study will only consider fully-accommodating and specular walls although the numerical tools developed as part of this research are capable of more general conditions, implementing the first method for treating partially accommodating boundaries.

If specular or partially accommodating walls are used, the specular velocity is identical to the incident velocity except the velocity component normal to the surface is reversed and the diffuse velocity is sampled from a half-Maxwellian such that the normal component of velocity is

$$c_\perp = \sqrt{2RT_w}\sqrt{-\log\left(1-\mathcal{R}_u\right)} + V_{w,\perp} \tag{3.83}$$

and the tangential components are

$$c_\parallel = \sqrt{RT}\mathcal{R}_n + V_{w,\parallel} \tag{3.84}$$

where $\mathcal{R}_n$ is a normally distributed random variable.

The preserved temperature and velocity are set equal to the boundary quantities as follows

$$\boldsymbol{V}^\star = \alpha \boldsymbol{V_w} + (1-\alpha)\,\boldsymbol{V}^s \tag{3.85}$$

$$T^\star = \alpha T_w + (1-\alpha) T^s \tag{3.86}$$

where T^s is the temperature of the particle prior to the interaction.

However, the boundary also plays a rôle in the FVM updates. In order to maintain numerical stability, the correlation coefficients at the boundary should be extrapolated from the interior, rather than calculated directly from the wall properties. Currently a three point linear extrapolation is used:

$$\boldsymbol{Q}_w = \frac{1}{3}\left(4\boldsymbol{Q}_0 + \boldsymbol{Q}_1 - 2\boldsymbol{Q}_2\right) \tag{3.87}$$

where the subscripts 0, 1, and 2 of the quantity $\boldsymbol{Q}$ designate the first, second, and third cells adjacent to the wall w, *i.e.*, W | 0 | 1 | 2. Although they do not directly contribute to the updates, the boundaries continue to directly affect the flow via the particle interactions. In the case of specular walls ($\alpha = 0$) the tangential components of momentum correlation coefficients and the energy transfer correlation coefficients vanish. The normal component of the momentum correlation coefficient should be set equal to the negative of the normal component in the adjacent cell,

Open boundary conditions require the generation of particles. The simplest form of an open boundary condition is a period case, wherein particles leaving one side of the simulation are reinserted at the other side with no changes to their properties, only their position. Inlet and outlet boundary conditions are also common, especially in high-speed flows, where the stream velocity is larger than the thermal velocity. In such flows, it may be assumed that the number of molecules migrating against the flow to either exit by the inlet or enter by the outlet are negligible. As such the flow conditions, temperature, velocity, and pressure, may be used to assign the number of particles introduced at the inlet and their velocities (sampled from either a Maxwellian or Chapman-Enskog distribution). The number of new molecules introduced at the inlet of a high-speed flow may be calculated as follows

$$N = p/(k_B T) A V_{in} \Delta t \tag{3.88}$$

where A is the area of the inlet, V_{in} is the velocity at the inlet, and Δt is the time step. Particles leaving the simulation at the outlet are removed from the simulation (this treats the outlet as a vacuum).

More complicated are pressure boundary conditions for low-speed flows. In these flows, molecules are likely to migrate against the bulk flow. As such, molecules are allowed to exit via the inlet, and a certain number of molecules must be introduced at the outlet. A number of different techniques have been proposed to approximate the number and properties of these "back flow" molecules [74, 33, 22, 114, 100], however the IP treatment greatly

simplifies the issue by reducing the statistical scatter. The outlet velocity and temperature may then be used with a prescribed outlet pressure to calculate the number of molecules to be injected into the system, as in Eq. (3.88). The DSMC properties of these inserted molecules may then be assigned as before, using the outlet pressure, temperature, and velocity (the last two being sampled from the interior IP quantities). The IP quantities of all inserted particles (at the inlet and outlet) are set equal to these quantities. For these boundaries, and especially when the system is to be coupled, reservoir cells are used. In each time particles are generated to populate the cell, approximating the current density of the cell (as prescribed or sampled from the interior). Any particles that leave the cell during the time step are allowed to enter the computational domain, otherwise particles are removed from the simulation. This removes the complexity (and possible error) of approximating *a priori* the number of particles crossing the interface, as this will no longer follow the simple relationship used for high-speed flows in Eq. (3.88). Although a Maxwellian distribution may be used for the generation of particles, the consensus in the literature is that a Chapman-Enskog distribution should be used, and is used for the open boundary conditions used in this study. The details of this will be presented in Section 5-10.

As with solid boundaries, the correlation coefficients need to be extrapolated to the boundaries, with the exception that the exterior pressure is used to calculate the density if the flow is directed into the domain, and the extrapolated pressure used if the flow is directed out of the domain. This allows the boundary to serve as either an inlet or outlet (in a similar way the density used in generating particles should also reflect the flow direction).

3.2.7 Summary of IP-DSMC Operation

At this time there are no known stability criteria for the IP-DSMC, although there are some recommendations based on practical experience. Although the underlying DSMC method is inherently stable, the finite volume method update used in the IP-DSMC can introduce instability. As mentioned previously, an upstream method is required for the

density update to avoid non-physical "wiggles" in the solution. Although not physically admissible, such behavior is a valid numerical solution. Catastrophic instabilities may arise if any particle is assigned a negative temperature, which is both physically and numerically inadmissible. Often this may be ameliorated by "thermalizing" the particles velocity or by borrowing thermal energy from other particles. It appears that negative temperatures arise when particles are assigned velocities much higher than the stream velocity. This occurs most in highly rarefied flows—especially in the free molecular regime. In these cases, it appears that the fluctuations in the number and properties of particles in adjacent cells leads to steep gradients of the correlation coefficients. The momentum update based on these may then impart a large acceleration. Over many time steps particles may reach high velocities (on the order of the DSMC velocities). At best this will cause the IP-DSMC to perform little better than the DSMC, and at worst will lead to negative temperatures. By using a larger number of particles in the IP-DSMC than would be require for a conventional DSMC simulation (*e.g.* 100 or so as suggested by Sun [99]) these fluctuations can be reduced, improving stability.

Another issue affecting stability is the representation of the density in the momentum and energy updates. As previously mentioned the mathematically correct densities (of the current and previous time step) should be replaced by the density corresponding to the number of particles within the cell. For many transitional flows either method has been observed to function in a stable manner, however for near-continuum flows small perturbations may be amplified in an unstable manner as they propagate through the simulation. The IP-DSMC theory would greatly benefit from a careful study of stability, using both practical and mathematical analysis to develop a stability criteria for the IP method. Future work should also consider the method of averaging the correlation coefficients, as the current technique tends to have difficulty with highly rarefied flows.

The cells sizes and time steps used in the IP-DSMC should follow the selection criteria for the DSMC, namely that cells should be smaller than the mean free path (nominally $\lambda/3$)

and time steps should be selected to ensure that an average particle will require multiple time steps to traverse a cell [43]. One reason for this is that in order for the IP method to work, a fully functional DSMC simulation is required. If the DSMC does not accurately model the flow, then good results from the IP-DSMC cannot be expected At times computational expense may necessitate larger cell sizes, but these may blur some of the flow features. In this study the time step is selected such that a particle moving at the most probable velocity (of an equilibrium distribution at the average temperature of the simulation) will require five time steps to traverse a cell. One additional consideration is that samples should be statistically significant. Due to the small time steps over which particles move and the relatively few collisions occurring during this time (for many flows), sampling should only be performed periodically. Most of the simulations in this study sample every 12 time steps.

The basic steps in the IP-DSMC method, and the underlying DSMC are:

1. Initialize particles (DSMC: position and velocity), (IP-DSMSC: temperature, velocity)

2. Move particles (with DSMC velocity), evaluate boundary interactions (DSMC and IP-DSMC)

3. Insert particles at open boundaries (DSMC and IP-DSMC), use IP quantities in determining number of particles and their properties

4. Sort particles into cells and subcells (DSMC)

5. Select collision pairs and evaluate collisions (DSMC and IP-DSMC)

6. Evaluate correlation coefficients (IP-DSMC)

7. Modify preserved information based on FVM and correlation coefficients (IP-DSMC)

8. Sample DSMC and IP-DSMC data

Steps 2–6 are repeated for each timestep, while 6 will be preformed periodically to build up time ensemble samples.

3.3 GT-DSMC

The current research utilizes GT-DSMC, an object oriented parallel DSMC/IP-DSMC simulation code developed by the author and associates in C++. GT-DSMC uses uniform rectilinear Cartesian cells to simplify the implementation and focus on the issues involved in Information Preservation techniques and multiscale modeling. This is compatible with the simple, and largely rectilinear, micro- and nano-scale geometries targeted by this research. The methods developed during this research and implemented in GT-DSMC can be applied to more general cell discretizations including unstructured meshes.

Care has been taken to maintain portability and the code has been developed and executed on MS Windows and Linux workstations and SGI supercomputers. On the latter two platforms, OpenMP has been used to parallelize the operation for Symmetric Multi-Processor (SMP) architectures. Figure 3-2 presents a screen capture showing the main user interface. The graphical user interface utilizes FLTK (`www.fltk.org`), a cross platform GUI toolkit, and provides an easy means of setting simulation parameters and output options, as well as allowing pausing of simulations. Alternatively a command line interface is also provided and is used for interactive and non-interactive command line execution.

The BOOST serialization library (`www.boost.org`) has been used to store the runtime state for restarting simulations, allowing for simulations to be stopped and continued at a later time, or restarted in the event of system crashes. This is particularly useful on the Georgia Tech HPC SGI systems, as these limit simulation times to 24 CPU hours—requiring simulations to be restarted frequently.

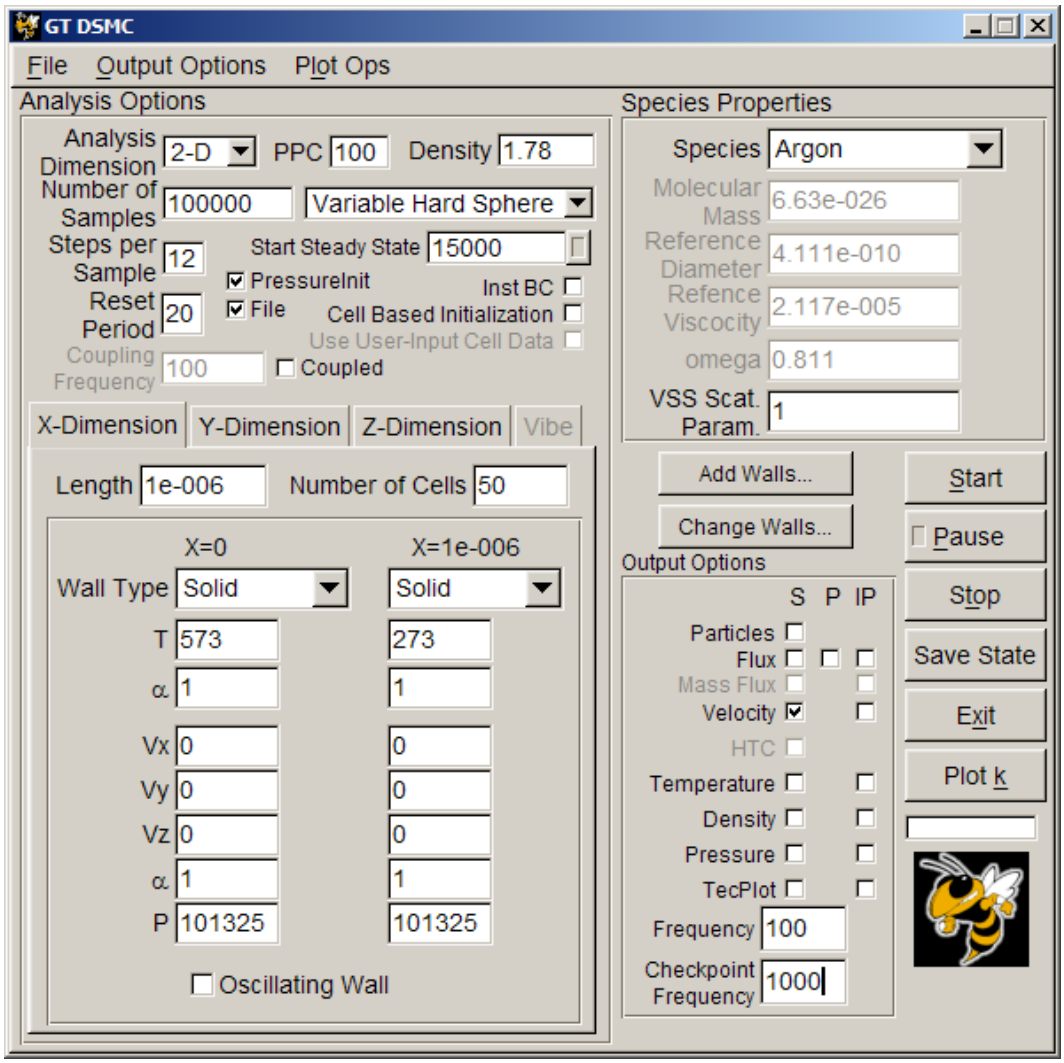

Figure 3-2: Screen capture of GT-DSMC graphics user interface (GUI)

In terms of object orientation, the fundamental physical entities: particles and boundaries, as well as computational cells are implemented as classes. Each particle is instantiated as a class with methods that modify or query the particle's properties. Likewise, cells contain buffered lists of particles that can be operated on and sampled. These buffered lists avoid constant allocation-deallocation of memory as particles are passed between cells, and in the parallel processing, between processors.

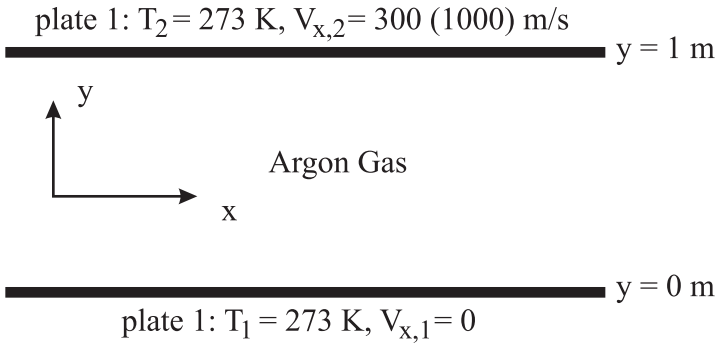

Figure 3-3: Schematic for High Speed Couette Flows

Finally, a source of random numbers, or at least a source of good pseudo-random numbers (PRN), is required to perform any stochastic simulation. GT-DSMC utilizes the Mersenne Twister MT 19937 algorithm designed by Matsumoto and Nishimura. This algorithm provides for fast generation of high quality pseudo-random numbers with a period of $2^{19937} - 1$ and high dimensional equidistribution, and is considered the current state of the art for PRN generation [68]. The specific C++ MT library was developed by Richard J. Wagner and is available at `http://www-personal.engin.umich.edu/~wagnerr/MersenneTwister.html`.

3.4 Validation of the IP-DSMC Method

Sun and Boyd have demonstrated that the Flux Splitting IP-DSMC performs well for shock front and thermal Couette flow problems [101]. Furthermore, as a superset of the Additional Energy method, it should perform well on any problem for which that method was successful [100, 99], including high speed Couette flow. The following simulations serve as a validation of the current implementation of the Flux Splitting IP-DSMC—comparing the IP-DSMC to published results and to the underlying DSMC—and explore the capabilities of the method.

3.4.1 High-Speed Couette Flow

The Couette flow problem consists of a flow between two parallel (or coaxial) surfaces as shown in Figure 3-3. Two velocity differences will be considered: $\Delta V = 300$ m/s and 1000 m/s, with Argon gas at an initial temperature of 273 K and pressure of 0.5277 Pa, which corresponds to a number density of 1.4×10^{20}. These simulations will be compared to Bird's DSMC simulations [17]. The simulation domain is divided into 100 cells (with 10 subcells per cell for the selection of collision pairs).

Figures 3-4–3-11 present the results of these simulations, and one may observe very good agreement between the DSMC, IP-DSMC, and reference solutions. The reduced scatter in the GT-DSMC data is due in part to a larger number particles per cell than used by Bird—and hence a larger samples set. Furthermore, the number of samples was large to provide a good comparison between the current implementation of the DSMC and the IP-DSMC directly. In all cases, the IP-DSMC provides smooth results at far fewer samples (usually a few thousand) than required by the DSMC. Figure 3-11 presents plots not available in Bird's text, but he does mention that the maximum temperature was 438 K. Finally, The shear stress profiles may be observed to be consistent with each other (DSMC and IP-DSMC).

3.4.2 Thermal Couette Flow

One of the simplest nonequilibrium flows is thermal Couette flow, consisting again of two parallel plates, except with a temperature, rather than a velocity, differential. Similar DSMC simulations, based on a Hard Sphere model will be used later in this thesis to develop a simplified model of the TSAFM system. Sun and Boyd presented results of thermal Couette flow simulations based on the DSMC and the Flux Splitting IP-DSMC spanning a wide range of flow conditions, Kn = $0.01 \rightarrow 100$ with $T_1 = 373$ K and $T_2 = 173$ K [101] that will be used for comparison.

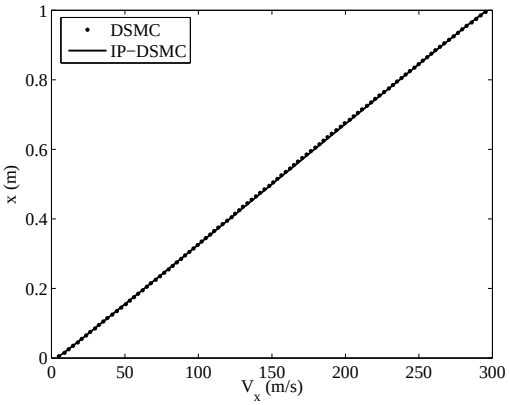

3-4(a): GT-DSMC

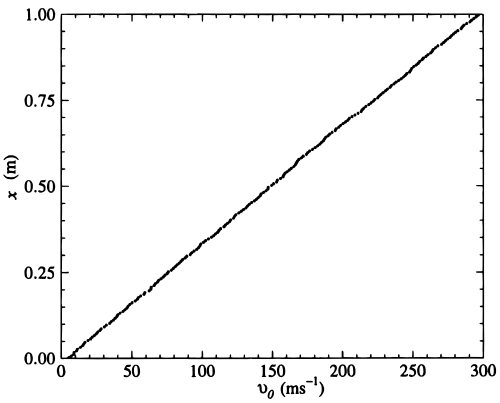

3-4(b): Bird

Figure 3-4: High-Speed Couette Flow (300 m/s): Velocity Profile

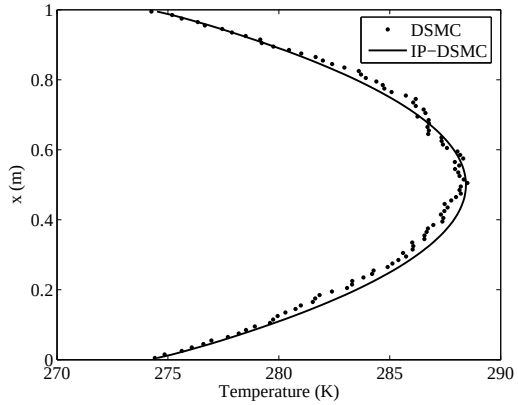

3-5(a): GT-DSMC

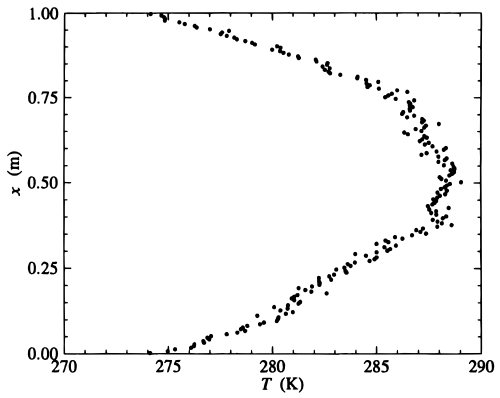

3-5(b): Bird

Figure 3-5: High-Speed Couette Flow (300 m/s): Temperature Distribution

The simulation domain is divided into 100 cells, except for the dense (Kn = 0.01) simulation, where 300 cells are required to have adequately sized cells. Again excellent agreement is observed for the temperature distributions. The heat flux is compared to DSMC and Additional Energy IP-DSMC simulations from and earlier paper by Sun and Boyd [100]. (The large scatter visible in the DSMC solution of the Kn = 0.01 illustrates the challenges involved modeling in low speed with the DSMC, as the Kn = 0.01 simulation has three times as many particles, a smaller mean free path, and therefore a smaller timestep, so time

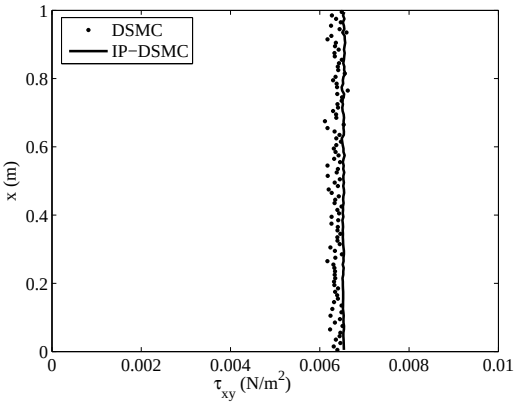

3-6(a): GT-DSMC

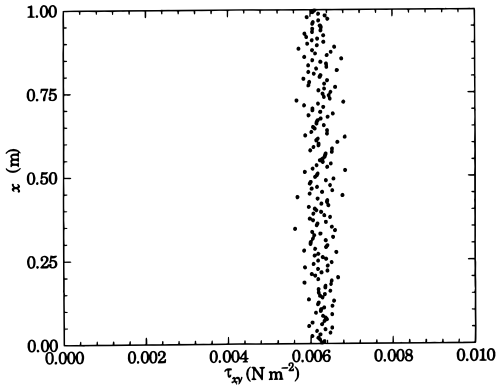

3-6(b): Bird

Figure 3-6: High-Speed Couette Flow (300 m/s): Shear Profile

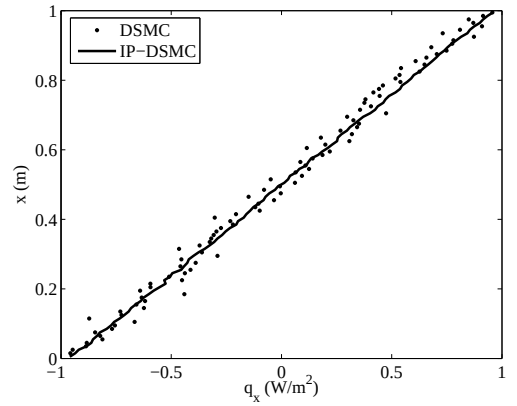

3-7(a): GT-DSMC

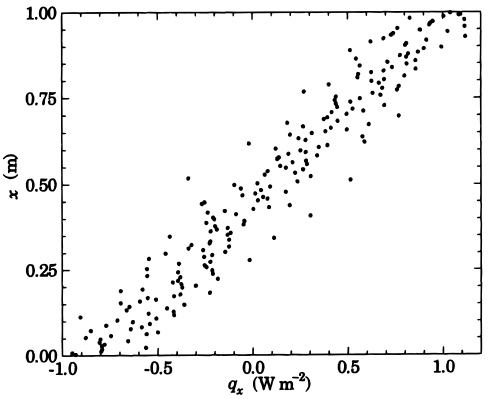

3-7(b): Bird

Figure 3-7: High-Speed Couette Flow (300 m/s): Heat Flux Profile

near continumm simulation is quite expensive. As such it was stopped when the IP-DSMC had acquired sufficient samples for smooth results

In previous IP-DSMC studies of thermal Couette flow, only the temperature profile and the heat transfer have been reported. It is interesting to note that slight variations in the temperature and density profiles in (see Figures 3-13 and 3-15(a)) may result in significant pressure differences between the IP-DSMC and the DSMC, although the magnitude remains comparable, as shown inf Figure 3-15(b).

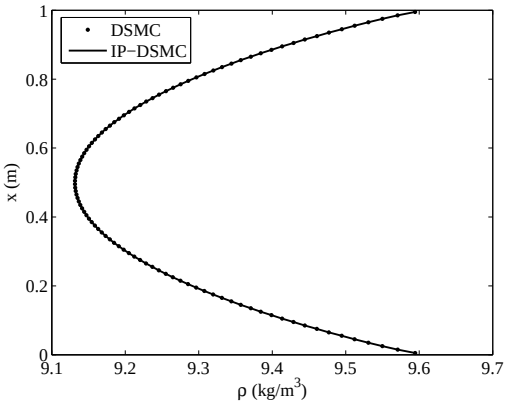

3-8(a): GT-DSMC

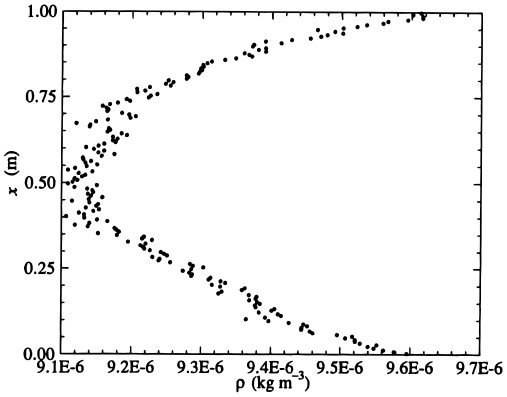

3-8(b): Bird

Figure 3-8: High-Speed Couette Flow (300 m/s): Density Distribution

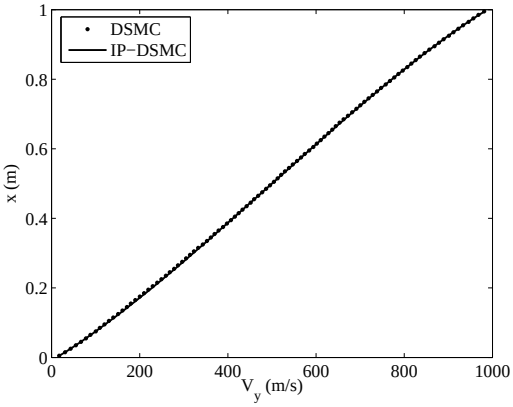

3-9(a): GT-DSMC

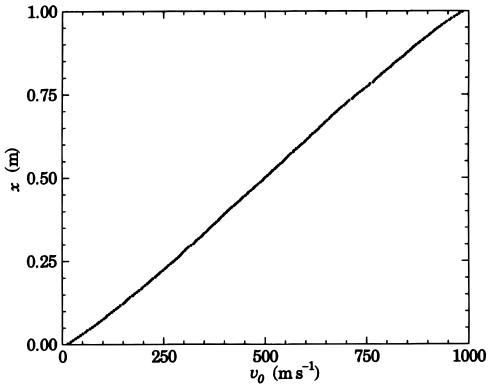

3-9(b): Bird

Figure 3-9: High-Speed Couette Flow (1000 m/s): Velocity Profile

Because of the wide range of heat flux values the average heat flux for each simulation are tabulated in Table 3-1. Numerical values are not available from the published reference.

3.4.3 Thermal Transpiration

The preceding simulations have attempted to validate the current implementation (and the Flux Splitting Method) for 1D flows. Before applying the method to coupled simulations, it is important to validate its behavior for more complex flows. One of the many interesting

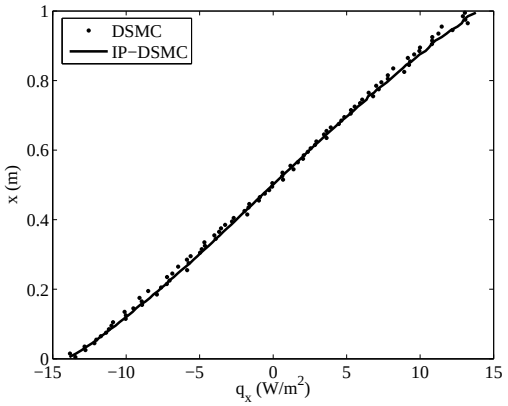

3-10(a): GT-DSMC

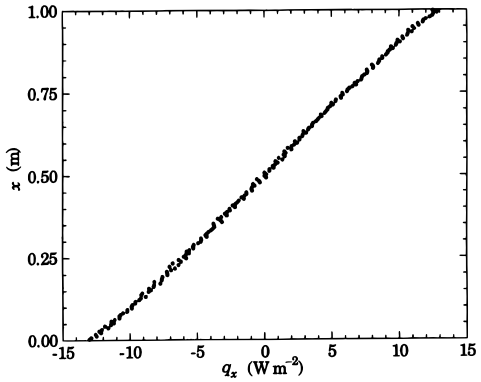

3-10(b): Bird

Figure 3-10: High-Speed Couette Flow (1000 m/s): Heat Flux Profile

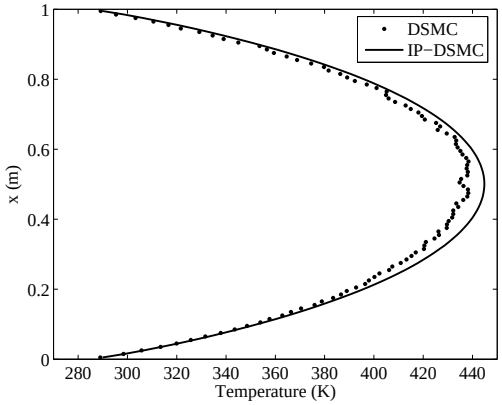

3-11(a): GT-DSMC: Temperature Distribution

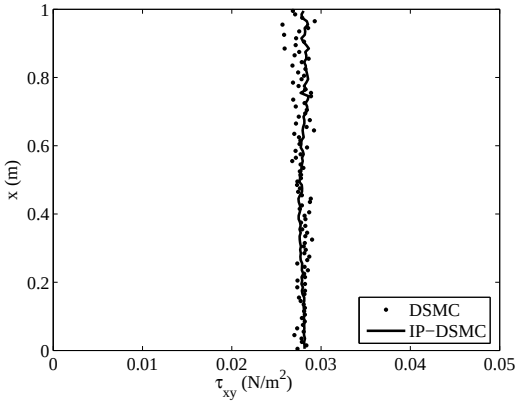

3-11(b): GT-DSMC: Shear Profile

Figure 3-11: High-Speed Couette Flow (1000 m/s)

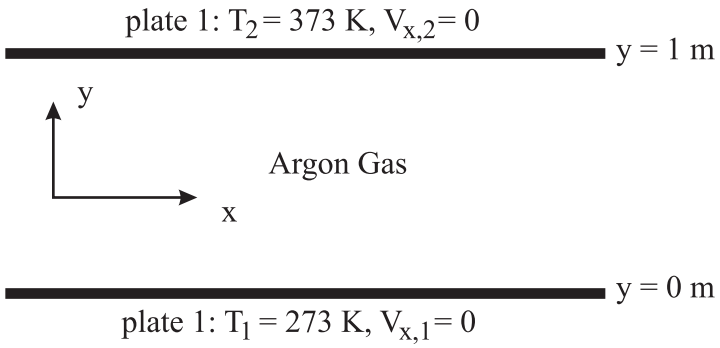

Figure 3-12: Schematic for thermal Couette flows

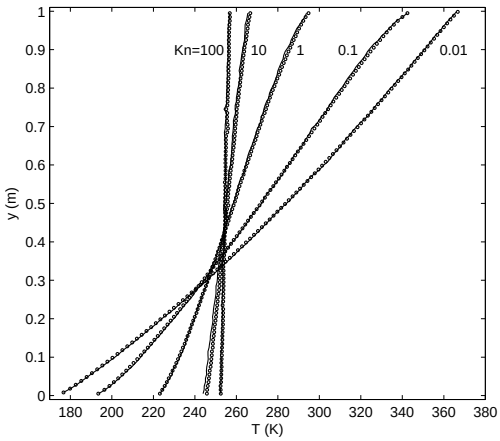

3-13(a): GT-DSMC

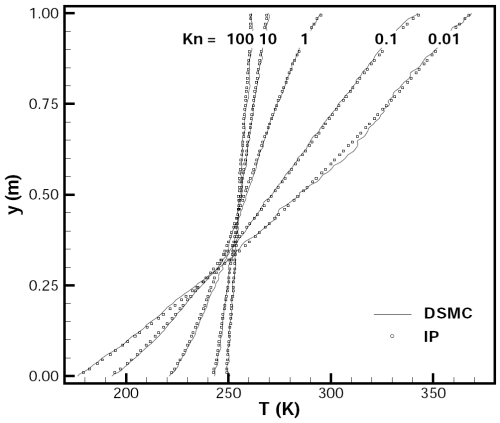

3-13(b): Reference Flux Splitting Method [101]

Figure 3-13: Thermal Couette Temperature Profiles for Kn = 0.01, 0.1, 1, 10, 100; circles: DSMC, line: IP-DSMC

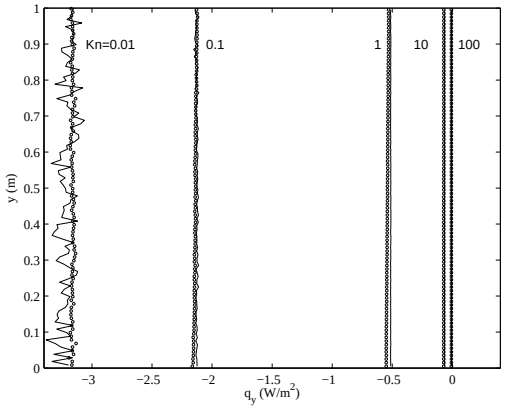

3-14(a): GT-DSMC

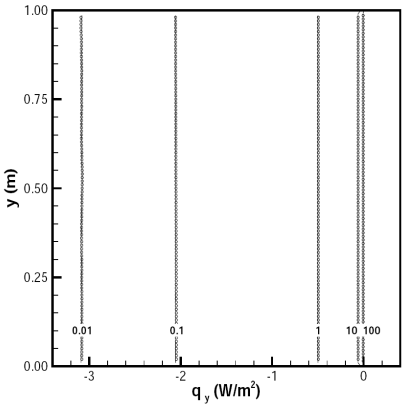

3-14(b): Sun

Figure 3-14: Thermal Couette flow: Heat flux profiles for Kn = 0.01, 0.1, 1, 10, 100; circles: DSMC, line: IP-DSMC

Table 3-1: Average heat flux of thermal Couette flow simulations

Knudsen Number	Current IP	Current DSMC
100	−0.0075	−0.0066
10	−0.078	−0.0637
1	−0.5397	−0.5126
0.1	−2.1396	−2.1266
0.01	−3.1617	−3.2180

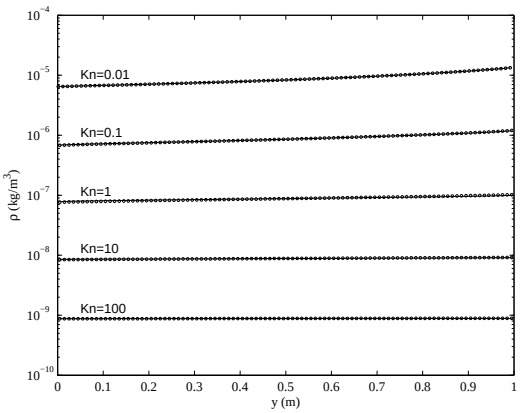

3-15(a): Thermal Couette Density Profiles for Kn = 0.01, 0.1, 1, 10, 100

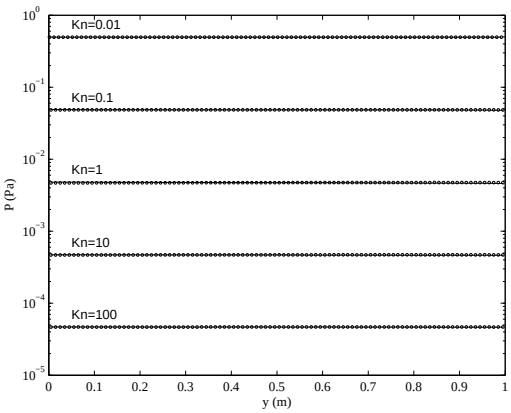

3-15(b): Thermal Couette Temperature Profiles for Kn = 0.01, 0.1, 1, 10, 100

Figure 3-15: Thermal Couette Flow: Density and Pressure Profiles for Kn = 0.01, 0.1, 1, 10, 100; circles: DSMC, line: IP-DSMC

phenomena that may manifest in rarefied gas flows is thermal transpiration. Thermal transpiration arises from the interaction of a rarefied gas with a surface with spatially varying temperatures (although similar flows may be induced by nonuniform temperature gradients away from a surface [49, 55]). A great deal of attention has been given to this (and the related phenomena of thermal creep, Knudsen Force, and the radiometric force): theoretically [11, 98], computationally [19, 79, 75], and experimentally [5]. Recently thermal transpiration MEMS systems for micropumping [4, 69, 103, 104] and micropropulsion [76] have been developed.

As molecules of the gas impinge on a surface they carry with them a certain amount of momentum. The speed of a particle will (on average) be proportional to the square root of the temperature of the region, or surface, it has last interacted with (surface or intermolecular collisions). In the case of rarefied gas flows, molecule may have traveled a significant distance from the previous point of interaction. As such, molecules coming from hotter regions of the gas will impart a greater tangential momentum to the surface than will molecules arriving from colder regions. On average, particles leaving the surface will have no net tangential, or shear, momentum. Thus the net exchange of momentum with

the surface will exert a tangential traction on the gas opposite the temperature gradient and resulting in a creep flow along the surface from cold to hot [50, 61, 98]. This then becomes the driving force for thermal creep, thermal transpiration and the radiometric effect. If the system is a channel or capillary, then the effect of thermal transpiration will be to pump molecules from the cold to the hot end until the pressure increases sufficiently at the hot end to counter the effect of thermal transpiration. If the channel connects two reservoirs, then pumping will continue as long as the temperature difference is maintained. In the case of the radiometric effect, the temperature difference between the two sides of a vane induces a flow from the cold (white) side to the hot (black) side—and is predominantly an edge effect. Recently, this understanding has led several researchers to design systems that maximize the edge effect by utilizing perforated surfaces [84, 90].

As with previous simulations, the IP-DSMC requires the DSMC to work, therefore, in these simulations the DSMC results will be used for comparison. Furthermore, a method proposed by Sharipov for calculating the pressure ratio due to thermal transpiration in 2D microchannels provides a second comparison [91, 92]. This method is based on a linearized S-model solution of the Boltzmann Transport Equations and assumes that the channel is long in comparison to the width, so that the end effects may be neglected and that the temperature gradient be small. The pressure ratio may be obtained by balancing the pressure driven and thermal creep flows. As the channel simulated here is short, and is a sealed system involving corners, there will be some non-idealities not accounted for in Sharipov's model.

The geometry for the thermal transpiration simulation consists of a 2D microchannel, 5 μm in length with and 1 μm wide. A temperature gradient is prescribed along the length of the walls varying linearly from 273 K to 573 K. The working gas is Argon and the DSMC and IP-DSMC simulation molecules are initialized such that the pressure is uniform and 1 atm. The channel is divided into 200 computational cells along the length and 40 cells along the width.

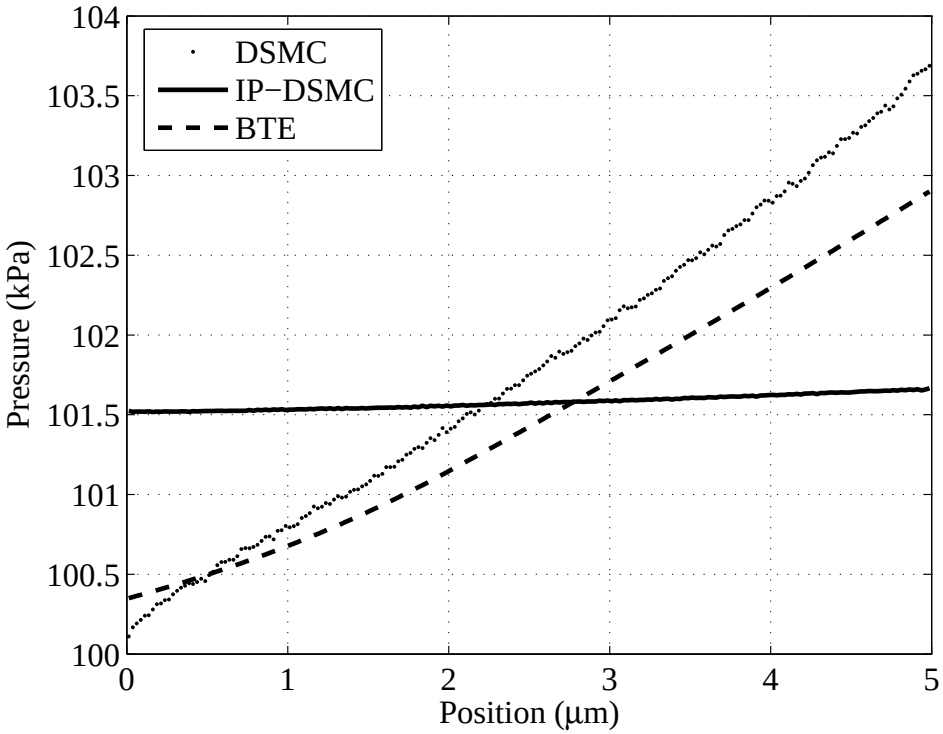

Figure 3-16: Pressure distribution from DSMC and Flux Splitting IP-DSMC

Figure 3-16 presents the results of these simulations, comparing the DSMC and IP-DSMC and Sharipov's solution. The simulation was allowed to run 96000 time steps. At this point sampling was begun until 7000 samples were accumulated (to ensure statistical significance there are 12 time steps between each sample). Although the temperature profiles agree very well (not shown), the IP-DSMC predicts a nearly uniform pressure along the length of the channel (see Figure 3-16), and essentially zero flow. Meanwhile, the DSMC exhibits a significant pressure difference of approximately 4 kPa, which corresponds well with Sharipov's solution ($\approx$ 3 kPa pressure difference). From these results, it is evident that the Flux Splitting method does not adequately capture the behavior of thermal transpiration or related phenomena.

3.5 Thermal Transpiration: Postmortem

In order to understand why the Flux Splitting IP-DSMC fails, one must carefully consider the conditions in the real gas, and how and what the IP-DSMC preserves. The 1D thermal Couette flow will be useful in the following discussion.

Consider a 1D thermal Couette flow where the working gas may be considered to be a continuum. Energy is transported in a diffusive manner, *e.g.*, molecules move very small distances relative to the domain before interacting with other molecules. Furthermore, these collisions are frequent. Thus, in any small region of the flow, one may assume that the gas molecules are in a quasi-equilibrium and may be described by a single equilibrium (or Maxwellian) distribution.

$$f(\boldsymbol{c}) = \frac{\beta^3}{\pi^{3/2}} e^{-\beta^2(\boldsymbol{c}-\boldsymbol{c}_0)^2} \tag{3.89}$$

recalling that in a stationary gas, $\boldsymbol{c}_0 = \mathbf{0}$ and $\boldsymbol{c}' = \boldsymbol{c}$. Consider now that the gas is rarefied such that collisions are infrequent, *e.g.*, free molecular flow. In this case the molecules can no longer be considered to be in equilibrium with each other, and in the complete absence of intermolecular collisions they are in fact equilibrated with the last surface with which they interacted. Thus, in the free molecular limit, the flow is bimodal, with two modes, or classes, of particles, each in equilibrium with the surface from which they were last emitted. The average speed of each of these classes normal to the surfaces is

$$\overline{c_H} = \frac{\int_{-\infty}^{\infty}\int_{-\infty}^{\infty}\int_{0}^{\infty} c_x f_H \, \mathrm{d}c'_x \, \mathrm{d}c'_y \, \mathrm{d}c'_z}{\int_{-\infty}^{\infty}\int_{-\infty}^{\infty}\int_{0}^{\infty} f_H \, \mathrm{d}c'_x \, \mathrm{d}c'_y \, \mathrm{d}c'_z} = \frac{1}{\sqrt{\pi}\beta_H} = \sqrt{\frac{2\,R\,T_H}{\pi}} \tag{3.90}$$

$$\overline{c_C} = \frac{\int_{-\infty}^{\infty}\int_{-\infty}^{\infty}\int_{0}^{\infty} c_x f_C \, \mathrm{d}c'_x \, \mathrm{d}c'_y \, \mathrm{d}c'_z}{\int_{-\infty}^{\infty}\int_{-\infty}^{\infty}\int_{0}^{\infty} f_C \, \mathrm{d}c'_x \, \mathrm{d}c'_y \, \mathrm{d}c'_z} = \sqrt{\frac{2\,R\,T_C}{\pi}} \tag{3.91}$$

$$\tag{3.92}$$

(The average tangential velocity is zero). In steady state, mass conservation requires the net mass flux at any cross section to be zero, thus

$$\rho_H \overline{c_H} = \rho_C \overline{c_C} \tag{3.93}$$

$$n_H m \sqrt{\frac{2RT_H}{\pi}} = n_C m \sqrt{\frac{2RT_C}{\pi}} \tag{3.94}$$

$$\frac{n_H}{n_C} = \frac{\rho_H}{\rho_C} = \sqrt{\frac{T_C}{T_H}} \tag{3.95}$$

In the IP-DSMC, the underlying DSMC model behaves in the same manner as the real gas, *i.e.*, characterized by a bi-modal distribution of velocities. One of the primary objectives of the IP-DSMC is to reduce statistical scatter, particularly in the sampling of the velocity. As such, the update scheme modifies all particle velocities within a computational cell equally, blurring any modality in the preserved velocities. Furthermore, following a particle-surface interaction, the preserved velocity of the particle is reset to reflect the *velocity* of the wall and not its *temperature*. The preserved temperature is set as a function of the surface temperature, fulfilling the rôle of preserving the thermal components of velocity.

As a result of the manner in which the velocity is updated, the average preserved velocity of the simulation molecules within a computational cell approaches the expected stream velocity (zero). However, if the molecules are "colored" such that "red" and "blue" molecules have recently interacted with the hot and cold surfaces, respectively, then the average preserved velocities of the separate classes will also be zero—not $\sqrt{2RT_w/\pi}$. Temperature modality is preserved ($T_i = T_w$), but the velocity modality is not and must in fact be sacrificed in order to reduce statistical scatter.

So how does this effect the Flux Splitting method with respect to the thermal transpiration problem? Consider the momentum correlation coefficient tensor (see Eq. (3.42)) for a

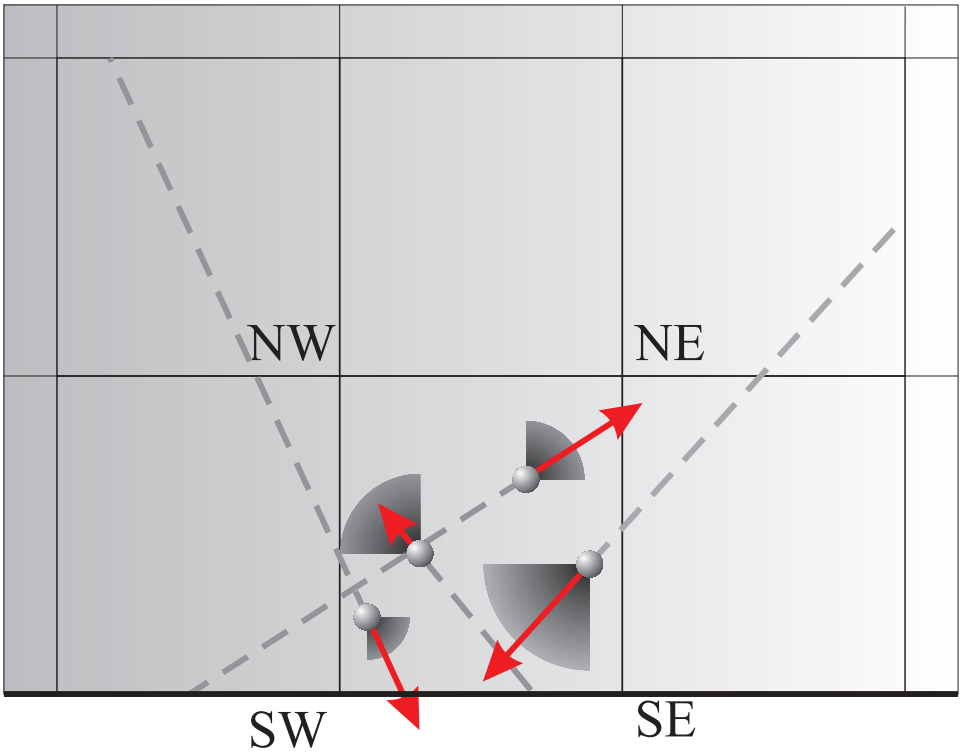

Figure 3-17: Diagram of particles classified into quadrants based on microscopic velocities (arrows) and showing the quadrants of velocity space for integrations

simulation molecule with temperature T and preserved velocity equal to the stream/splitting velocity $\boldsymbol{V} = \boldsymbol{a} = \boldsymbol{c}_0$

$$\overline{\boldsymbol{c}'\boldsymbol{c}'''} = \begin{bmatrix} RT/2 & 0 & 0 \\ 0 & RT/2 & 0 \\ 0 & 0 & RT/2 \end{bmatrix} \tag{3.96}$$

The purpose of the momentum correlation coefficient is to capture the momentum transport not preserved by the IP velocity. From Eq. (3.96), it is apparent that the Flux Splitting preserves the transport of momentum normal to an interface, but does not preserve the shear components.

Having identified this characteristic, it is now possible to revisit the 2D thermal transpiration case. Consider a small control volume adjacent to the lower bound of a 2D microchannel with a prescribed temperature gradient, $T(x = 0) = T_C$ and $T(x = L) = T_H$.

Assuming rarefied flow conditions, molecules entering the control volume from the left, will tend to be "colder", *i.e.*, have lower velocities than those entering from the right. Furthermore, molecules moving down ($c_y < 0$) are more likely to have traveled farther since their last interaction with either a surface or other molecules, than are those with $c_y > 0$, which have probably recently interacted with the lower bound at some nearby location. As the temperature gradient exists principally in the x-direction (most cross sections have nearly uniform temperatures), it should be appropriate to classify the particles in one of four classes designated by the direction of motion in two dimensions as shown in Table 3-2.

Table 3-2: 2D Particle Splitting Directions

Class	x-direction	y-direction
SE	$c_x < 0$	$c_y < 0$
SW	$c_x > 0$	$c_y < 0$
NE	$c_x < 0$	$c_y > 0$
NW	$c_x > 0$	$c_y > 0$

From the above arguments regarding the distance traveled, the following inferences may be made: 1. particles moving SW tend to have traveled from a region of higher temperature (located to the NE) and will thus have higher velocities on average than particles in the NW class. 2. Similarly, particles moving in the in SE direction are likely to be slower than particles moving in the NE direction. Thus we observe that there is (at least) a four-way modality to the system. A logical step would then be to treat each of these four classes, or modes, separately and then add up their contributions. This then leads to a Quadrant Splitting method in two dimensions and a general Octant Splitting method in three dimensions. Although it may seem more complex at this point, the following derivation will treat the 3D Octant Splitting Method.

3.6 Octant Splitting Method Correlation Coefficients

In the Flux Splitting method, each dimension of the velocity space was split into two half-spaces, and the halves summed to obtain the correlation coefficients for that dimension, *i.e.*, to calculate $c_i' c_1'''$, $c_i' c_2'''$, $c_i' c_3'''$ the velocity space in the i^{th}-dimension is split. In effect, each particle participates in D half-spaces—one for each dimension. Participating in multiple half-spaces does not cause a problem in the Flux Splitting method because of the way the correlation coefficients are averaged, and the fact that the off-diagonal terms of the Flux Splitting correlation coefficient are zero. Conversely, in the Octant Splitting method, it is assumed that the particles and the velocity space will be split uniquely into one and only one octant. Correlation coefficients may then be evaluated by performing the same integrations as before, but with limits of integration that reflect the octant splitting, *i.e.*, integration over eighth-Maxwellians (or more generally for the 2^D splitting directions in D-dimensional space):

$$\overline{\boldsymbol{Q}} = \sum_{j=1}^{2^D} \left[\frac{\sum_i \left\{ \delta(\boldsymbol{\zeta}) \frac{\beta^3}{\pi^{3/2}} \int_{\zeta_z} \int_{\zeta_y} \int_{\zeta_x} \boldsymbol{Q} \exp\left(-\beta^2 (\boldsymbol{c} - \boldsymbol{V})^2\right) \mathrm{d}\boldsymbol{c} \right\}_{ij}}{\sum_i \{\delta(\boldsymbol{\zeta})\}_{ij}} \right] \tag{3.97}$$

where $\boldsymbol{\zeta}$ is the splitting vector

$$\boldsymbol{\zeta} = \begin{bmatrix} c_x \gtrless a_x \\ c_y \gtrless a_y \\ c_z \gtrless a_z \end{bmatrix} \tag{3.98}$$

and $\delta(\boldsymbol{\zeta})$ classes each molecule into one of the Octants. The limits of integration for each of the three integrals directions are from $-\infty \rightarrow a_i$ for a negative split in the i^{th}-direction and from $a_i \rightarrow \infty$ for a positive split in the i^{th}-direction, and similarly for the other directions. After performing the integrations for all splitting directions, the many terms of the Octant

Splitting Correlation Coefficients may be summarized as follows:

$$\overline{c_i' c_i'''} = \left(1 \overset{J}{\pm} \operatorname{erf}\left(\beta\left(V_j - a_j\right)\right)\right)\left(1 \overset{K}{\pm} \operatorname{erf}\left(\beta\left(V_k - a_k\right)\right)\right) \times \left[\frac{R\,T\left(1 \overset{I}{\pm} \operatorname{erf}\left(\beta\left(V_i - a_i\right)\right)\right)}{8} \overset{I}{\pm} \frac{\left(a_i - c_{0i}\right) e^{-\beta^2 (V_i - a_i)^2}}{8\sqrt{\pi}\beta}\right] \tag{3.99}$$

$$\overline{c_i' c_j'''}|_{i \neq j} = \left(\overset{J}{\pm}\right) \frac{e^{-\beta^2 \left(V_j - a_j\right)^2}}{8\sqrt{\pi}\beta}\left(1 \overset{K}{\pm} \operatorname{erf}\left(\beta\left(V_k - a_k\right)\right)\right) \times \left[\left(V_i - c_{0i}\right)\left(1 \overset{I}{\pm} \operatorname{erf}\left(\beta\left(V_i - a_i\right)\right)\right) \overset{I}{\pm} \frac{e^{-\beta^2 (V_i - a_i)^2}}{\sqrt{\pi}\beta}\right] \tag{3.100}$$

Notice that the tensor $\overline{c_i' c_j'''}$ is not necessarily symmetric.

The correlation coefficient for energy transport may be obtained in a similar, albeit lengthy, manner:

$$\overline{\left(V^2 + 3\,R\,T - c^2\right) c_i'} = E_i - E_j - E_k \tag{3.101}$$

where

$$E_i = \left(1 \overset{J}{\pm} \operatorname{erf}\left(\beta\left(V_j - a_j\right)\right)\right)\left(1 \overset{K}{\pm} \operatorname{erf}\left(\beta\left(V_k - a_k\right)\right)\right) \times \left[-\frac{V_i\,R\,T\left(1 \overset{I}{\pm} \operatorname{erf}\left(\beta\left(V_i - a_i\right)\right)\right)}{4} \overset{I}{\pm} \frac{\left(\left(c_{0i} - a_i\right)\left(V_i + a_i\right) - R\,T\right) e^{-\beta^2 (V_i - a_i)^2}}{8\sqrt{\pi}\beta}\right] \tag{3.102}$$

and E_j and E_k can be expressed in terms of the momentum correlation coefficients:

$$\begin{aligned} E_j &= \left(\overset{J}{\pm}\right)\left(V_j + a_j\right) \frac{e^{-\beta^2 \left(V_j - a_j\right)^2}}{8\sqrt{\pi}\beta}\left(1 \overset{K}{\pm} \operatorname{erf}\left(\beta\left(V_k - a_k\right)\right)\right) \\ &\quad \times \left[\left(V_i - c_{0i}\right)\left(1 \overset{I}{\pm} \operatorname{erf}\left(\beta\left(V_i - a_i\right)\right)\right) \overset{I}{\pm} \frac{e^{-\beta^2 (V_i - a_i)^2}}{\sqrt{\pi}\beta}\right] \\ &= \left(V_j + a_j\right) \overline{c_i' c_j'''} \end{aligned} \tag{3.103}$$

$$\begin{aligned} E_k &= \left(\overset{K}{\pm}\right)\left(V_k + a_k\right)\left(1 \overset{J}{\pm} \operatorname{erf}\left(\beta\left(V_j - a_j\right)\right)\right) \frac{e^{-\beta^2 (V_k - a_k)^2}}{8\sqrt{\pi}\beta} \\ &\quad \times \left[\left(V_i - c_{0i}\right)\left(1 \overset{I}{\pm} \operatorname{erf}\left(\beta\left(V_i - a_i\right)\right)\right) \overset{I}{\pm} \frac{e^{-\beta^2 (V_i - a_i)^2}}{\sqrt{\pi}\beta}\right] \\ &= \left(V_k + a_k\right) \overline{c_i' c_k'''} \end{aligned} \tag{3.104}$$

As stated previously, the Octant Splitting Method, or OSIP-DSMC, is a general form for 3D simulations. If the simulation is to be of lower dimensionality then some simplifying substitutions may be made, for example for a 2D simulations in the x-y plane: a. the exponential terms in degenerate dimensions vanish, *e.g.*, $e^{-\beta^2(V_z-a_z)^2} = 0$, and b. terms involving the erf are replaced by 2, *i.e.*, $(1 \pm \text{erf}\,(\beta\ (V_z - a_z))) = 2$. This results in a Quadrant Splitting method (QSIP-DSMC). Similarly, for 1D simulations the equations degenerate further (with y being the degenerate dimension) to recover the 1D Flux Splitting Method of Sun and Boyd [101]. Further degeneration (to zero-dimension) recovers what has been termed the Local Thermal Equilibrium Model [101]—which provides insight into the inadequacy of the LTE method, as it could only be of value for purely (and thus uninteresting) equilibrium situations. The intent of the Flux Splitting method, and of the new Octant Splitting method is to improve the ability of the IP-DSMC to model non-equilibrium systems while maintaining the reduced scatter in sampled quantities. Such systems often exhibit modality in the particle behavior, due to rarefaction or strong gradients (as in shock flow). In an equilibrium gas, the molecular distributions are isotropic, and thus any splitting of fluxes would be symmetric. Consequently, the Octant method, either by choice of the analyst, or as a result of the flow conditions may degenerate to the lower forms (QSIP, FS, or LTE). For consistency and to accentuate the general form, the higher order splitting methods, Quadrant and Octant, will be referred to simply as the Octant Splitting method, or OSIP-DSMC.

Consider now a particle whose microscopic velocity $\boldsymbol{c}$ is such that it is moving in a NE direction and whose preserved velocity matches the stream velocity ($\boldsymbol{V}_i = \overline{\boldsymbol{V}} = \boldsymbol{c}_0$). The Quadrant Splitting momentum correlation coefficient for this molecule is for the NE direction:

$$\overline{c_i' c_j'''} = \begin{bmatrix} \frac{RT}{4} & \frac{1}{4\pi\beta^2} & 0 \\ \frac{1}{4\pi\beta^2} & \frac{RT}{4} & 0 \\ 0 & 0 & \frac{RT}{4} \end{bmatrix} = \begin{bmatrix} \frac{RT}{4} & \frac{RT}{2\pi} & 0 \\ \frac{RT}{2\pi} & \frac{RT}{4} & 0 \\ 0 & 0 & \frac{RT}{4} \end{bmatrix} \tag{3.105}$$

Notice that for such a particle, the terms above degenerate diagonal components, *i.e.*, $\overline{c_i' c_j'''}$, where $j > i$ and i is a degenerate dimension and j is not (*e.g.*, the third column in Eq. (3.105)) vanish due to degeneracy; whereas rows to the left of such terms ($i > j$, *e.g.*, bottom row (3.105)) vanish due to the velocity flow assumptions $\boldsymbol{V} = \boldsymbol{a} = \boldsymbol{c}_0$ and not because they are not constrained by degeneracy.

Now consider three additional particles with preserved velocities also equal to the stream velocity but classed in each of the other splitting directions. The correlation coefficients may now be evaluated over the quadrants into which these molecules are split and added to obtain the complete correlation coefficient tensor for this simplified four particle system:

$$\begin{aligned}
\overline{c_i' c_j'''} &= \begin{bmatrix} \frac{R\overline{T}}{4} & -\frac{R\overline{T}}{2\pi} & 0 \\ -\frac{R\overline{T}}{2\pi} & \frac{R\overline{T}}{4} & 0 \\ 0 & 0 & \frac{R\overline{T}}{4} \end{bmatrix}_{NW} + \begin{bmatrix} \frac{R\overline{T}}{4} & \frac{R\overline{T}}{2\pi} & 0 \\ \frac{R\overline{T}}{2\pi} & \frac{R\overline{T}}{4} & 0 \\ 0 & 0 & \frac{R\overline{T}}{4} \end{bmatrix}_{NE} \\
&\quad + \begin{bmatrix} \frac{R\overline{T}}{4} & \frac{R\overline{T}}{2\pi} & 0 \\ \frac{R\overline{T}}{2\pi} & \frac{R\overline{T}}{4} & 0 \\ 0 & 0 & \frac{R\overline{T}}{4} \end{bmatrix}_{SW} + \begin{bmatrix} \frac{R\overline{T}}{4} & -\frac{R\overline{T}}{2\pi} & 0 \\ -\frac{R\overline{T}}{2\pi} & \frac{R\overline{T}}{4} & 0 \\ 0 & 0 & \frac{R\overline{T}}{4} \end{bmatrix}_{SE} \qquad (3.106) \\
&= \begin{bmatrix} \frac{R\left(\overline{T}_{NE}+\overline{T}_{NW}+\overline{T}_{SW}+\overline{T}_{SE}\right)}{4} & \frac{R\left(\overline{T}_{NE}-\overline{T}_{NW}+\overline{T}_{SW}-\overline{T}_{SE}\right)}{2\pi} & 0 \\ \frac{R\left(\overline{T}_{NE}-\overline{T}_{NW}+\overline{T}_{SW}-\overline{T}_{SE}\right)}{2\pi} & \frac{R\left(\overline{T}_{NE}+\overline{T}_{NW}+\overline{T}_{SW}+\overline{T}_{SE}\right)}{4} & 0 \\ 0 & 0 & \frac{R\left(\overline{T}_{NE}+\overline{T}_{NW}+\overline{T}_{SW}+\overline{T}_{SE}\right)}{4} \end{bmatrix}_{NE} \qquad (3.107)
\end{aligned}$$

As may be seen, the Octant Splitting method introduces new terms in the momentum correlation coefficient tensor that may provide a mechanism to recover shear from the preserved thermal energy, even in the case of stationary flow.

If the distribution of particle temperatures within a cell is such that $T_{SW} = T_{NW} > T_{SE} = T_{NE}$ (a bimodal distribution in the x-direction and uniform in y) then the shear terms vanish. This is in fact a manifestation of degeneracy due to the symmetry in the y- and z-directions reducing the QSIP-DSMC to the 1D Flux Splitting Method. Likewise for a similar system with a gradient in the y-direction but uniform in x. If however, the gradient is diagonal,

e.g. $T_{SW} > T_{SE} = T_{NW} > T_{NE}$, then there will be a net shear component. As previously discussed, the thermal transpiration problem exhibits multiple modalities, which should Octant Method will attempt to capture.

The same thermal transpiration simulation as previously discussed was repeated with the Octant Splitting Method, producing very good results. Figure 3-18(a) presents the OSIP-DSMC velocity field for this simulation which exhibits a recirculatory flow pattern. This is comparable to that obtained from the DSMC presented in Figure 3-18(b) (note the significant scatter remaining in the DSMC as compared with the OSIP-DSMC). Furthermore a static pressure gradient is developed and the pressures at either end of the channel are found to be within 1% of the DSMC solution (see Figure 3-24). Prior to presenting additional thermal transpiration simulations using the OSIP-DSMC (see Section 3.7.1) another aspect of the Octant Method must be addressed.

3.6.1 The Split Box Problem and the Impact of Coordinate Systems

An important aspect of the OSIP-DSMC was uncovered by applying the method to an interesting thermally driven flow identified by Aoki, *et al*. [7]. The simulation domain consists of a square region with a discontinuous temperature distribution such that one half of the boundary is maintained at $T_1 = 200$ K and the other at $T_2 = 400$ K, as illustrated in Figure 3-19. Hereafter, this geometry will be referred to as the "Split Box" problem. Figure 3-20(a) presents the velocity field obtained from the BGK solution of the Boltzmann Transport Equation by Aoki *et al*. for the lower half of the system with Kn = 0.2. The velocities are normalized relative to the most probable velocity, *i.e.*, $\boldsymbol{\xi} = \boldsymbol{c}/(2RT_1)^{1/2}$. The most striking feature of this problem is the induced circular flow creating a vortex pattern. The maximum velocity occurs near the discontinuity.

Applying the OSIP-DSMC to this problem yields the surprising flow field presented in Figure 3-20(b) which exhibits two vorticular patterns (note, the DSMC flow field behaved as expected, see Figure 3-29(a)). In light of the excellent agreement obtained in modeling

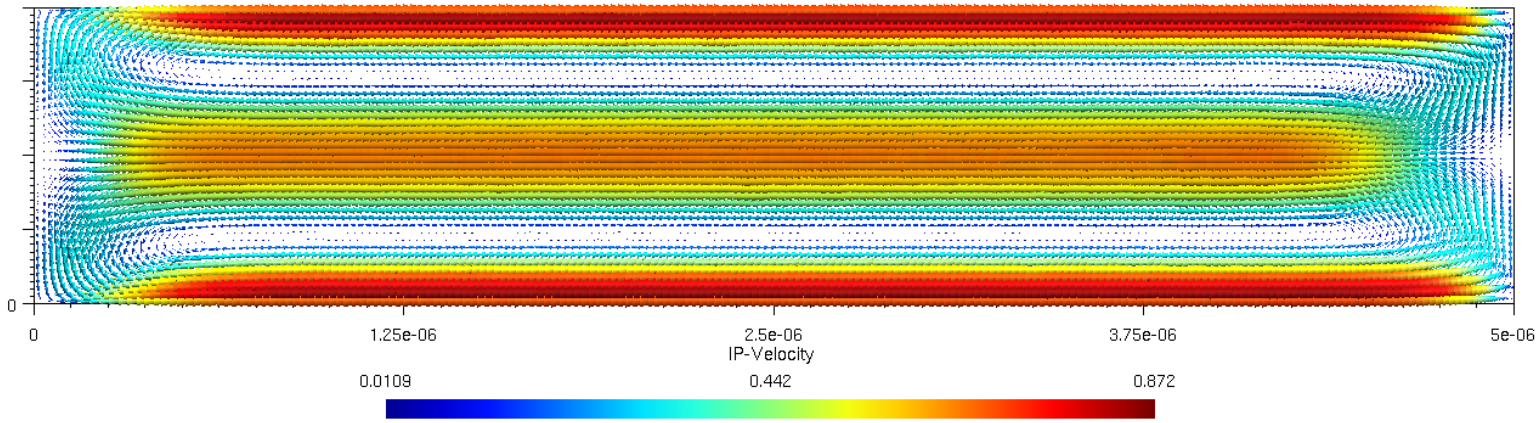

3-18(a): OSIP-DSMC

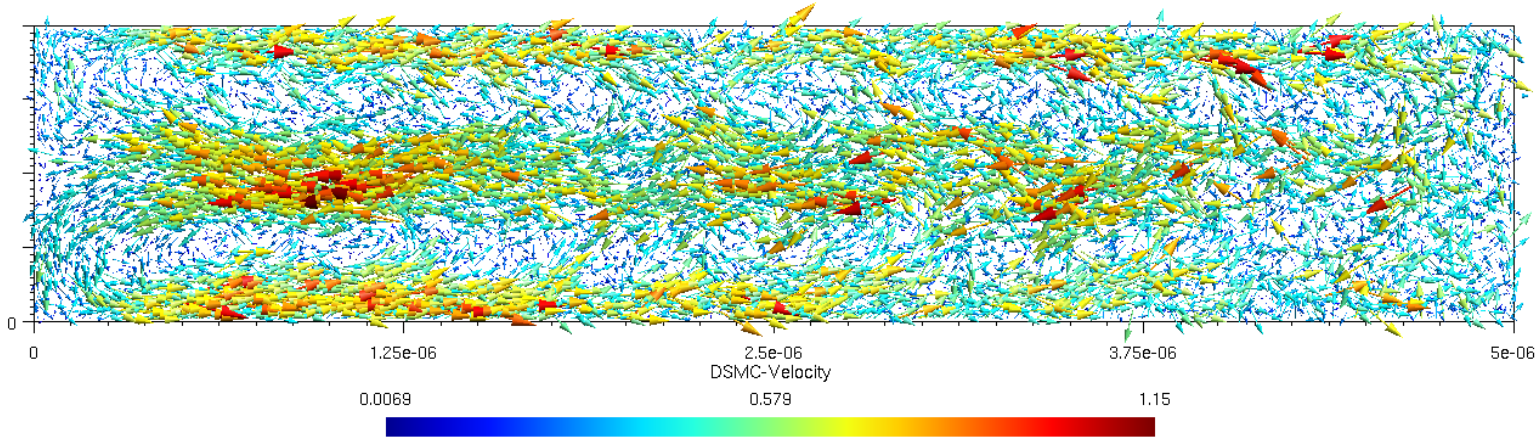

3-18(b): DSMC

Figure 3-18: Simulation results for thermal transpiration of a 5 μm × 1 μm channel with T_1 = 273 K and T_2 = 573 K

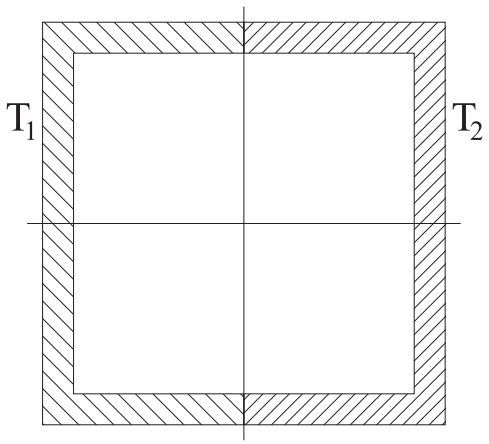

Figure 3-19: Boundary conditions for Split Box problem

thermal transpiration and the correct behavior of the underlying DSMC, this results seems quite mysterious. The explanation (and solution) may be identified by first returning to the correlation coefficient tensor. Using the same assumptions as before, the simplified form of the complete correlation coefficient tensor Eq. (3.107) may be used. A net shear will only arise in the absence of horizontal or vertical symmetry. From the published solution (and the DSMC solution) it is obvious that a net shear exists and is driving the flow—but in the case of the OSIP-DSMC, the wrong flow. Now consider the eigenvectors of the momentum correlation coefficients (recalling that this tensor is related to the stress tensor), clearly these will always be oriented at 45° from the global coordinate system (GCS) (although for flows where $\boldsymbol{V} \neq \boldsymbol{a} = \boldsymbol{c}_0$ there will generally be a small deviation). Consequently, the principal stresses (or pressure components) will also be oriented at 45° degrees from the global CS. This would seem to be a limitation of the method, and indeed affects all of the flux splitting IP Methods.

Recalling that the flux splitting methods seek to preserve the modality of the flow, it is logical—and in this case obvious—that the choice of coordinate system is not arbitrary, and that the global coordinate system is often a poor choice. This then requires that a natural local coordinate system (LCS) be chosen reflecting the flow conditions. As the

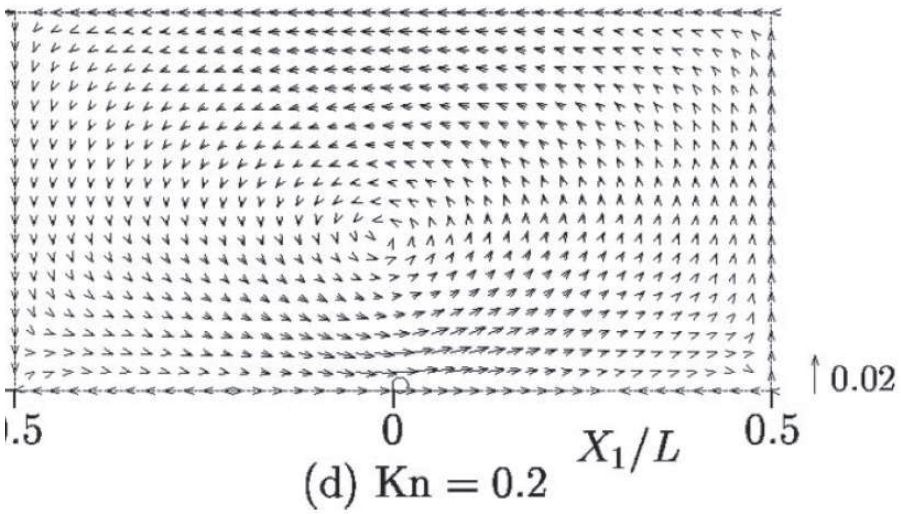

3-20(a): Velocity Field for Kn = 0.2

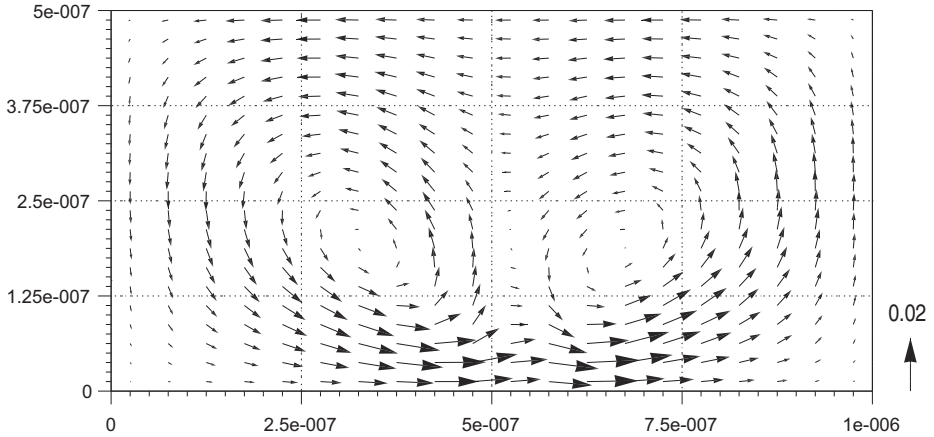

3-20(b): Octant Method simulation of Temperature Discontinuity without transformation to local coordinate system

Figure 3-20: Comparison of Velocity fields from BGK soluton for Kn = 0.2 and OIP-DSMC (Global CS)

modality to be preserved and exploited is usually associated with a temperature difference, or gradient, a logical choice would be for the LCS to be aligned with the iso-lines of temperature or—more generally and conveniently—the heat flux vector, $\boldsymbol{q}$. Figure 3-21 shows the iso-lines and heat flux vectors for the Split Box problem, and a strong curvature near the discontinuity is clear.

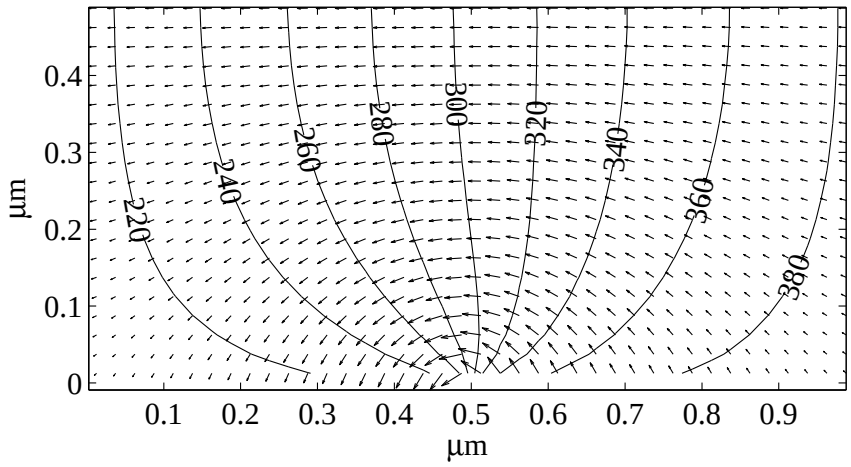

Figure 3-21: Split Box temperature contour plot (20 K iso-lines) and heat flux vectors

The heat flux vector, $\boldsymbol{q}$, for each computational cell is sampled periodically and is thus available for this purpose and will reflect changes in the flow conditions (in practice a weighted average of $\boldsymbol{q}$ is used until steady state is reached, then the steady state value is used). From $\boldsymbol{q}$ the local coordinate system may be constructed and the correlation coefficients evaluated as follows[1].

1. Identify the local coordinate system: $\boldsymbol{x}^{\diamond} = \frac{\boldsymbol{q}}{\|\boldsymbol{q}\|}$ and $\boldsymbol{y}^{\square} = \mathbf{R}_{z,90}\boldsymbol{x}^{\diamond}$ (where $\mathbf{R}_{z,90}$ rotates 90° counter-clockwise about the z-axis). In two dimensions $\boldsymbol{y}^{\diamond} = \boldsymbol{y}^{\square}$ and $\boldsymbol{z}^{\diamond} = \boldsymbol{z}$. In three dimensions $\boldsymbol{z}^{\square} = \boldsymbol{x}^{\diamond} \times \boldsymbol{y}^{\diamond}$, $\boldsymbol{z}^{\diamond} = \frac{\boldsymbol{z}^{\square}}{\boldsymbol{z}^{\square}}$ and $\boldsymbol{y}^{\diamond} = \boldsymbol{z}^{\diamond} \times \boldsymbol{x}^{\diamond}$

2. Construct the rotation matrix, $\mathbf{R} = [\boldsymbol{x}^{\diamond}, \boldsymbol{y}^{\diamond}, \boldsymbol{z}^{\diamond}]$

3. Transform the stream velocity and splitting velocity into the new coordinate system, *i.e.*, $\boldsymbol{c}_0^{\diamond} = \mathbf{R}^T\boldsymbol{c}_0$ and $\boldsymbol{a}_0^{\diamond} = R^T\boldsymbol{a}_0$

4. Transform the DSMC and IP velocities for each particle into the new coordinate system

[1]The choice of the directions orthogonal to $\boldsymbol{q}$ *i.e.*, $\boldsymbol{y}^{\diamond}$ and $\boldsymbol{z}^{\diamond}$, in three dimensions is currently considered arbitrary. This is an area that deserves further study.

5. Determine the splitting direction within the new coordinate system and calculate the correlation coefficients $\left(\overline{c_i' c_j'''}\right)^{\diamond}$ and $\left(\overline{c_i' \left(V^2 + 3\,R\,T - c^2\right)}\right)^{\diamond}$ and average these as in Eq. (3.97)

6. Return the complete correlation coefficients to the global coordinate system: $\overline{c_i' c_j'''} = \mathbf{R}\left(\overline{\boldsymbol{c}'\boldsymbol{c}'''}\right)^{\diamond}\mathbf{R}^T$ and $\overline{c_i'\left(V^2 + 3\,R\,T - c^2\right)} = \mathbf{R}\left(\overline{c_i'\left(V^2 + 3\,R\,T - c^2\right)}\right)^{\diamond}$

Steps 4 and 5 are repeated for every particle within the computational cell, where as the remaining steps need only be performed once per timestep. Figure 3-22 presents a flowchart of the complete Octant IP-DSMC method.

The excellent performance simulating thermal transpiration is easily explained by observing that other than very small regions near the corners, the heat flux and temperature profile predicted by the IP-DSMC are essentially aligned with the global coordinate system (see Figure 3-23).

3.7 Thermally Driven Flow Simulation Results

As previously noted, the 1D Octant IP Method is identical to the Flux Splitting method, therefore, its performance will be the same for any of the 1D flows. The following 2D flows explore the effects of thermally induced flow and the ability of the Octant Splitting IP Method to efficiently capture these phenomena.

3.7.1 Thermal Transpiration

The effect of thermal transpiration is known to increase as the Knudsen number increases, reaching a maximum value in the free molecular case, where the ideal pressure ratio of

$$\frac{P_1}{P_2} = \sqrt{\frac{T_1}{T_2}} \tag{3.108}$$

will be achieved. Two additional microchannels have been modeled with widths of 100 nm and 20 nm. For improved initial conditions (closer to the final state) Sharipov's solution is used for the initial pressure distribution (rather than the continuum solution of uniform

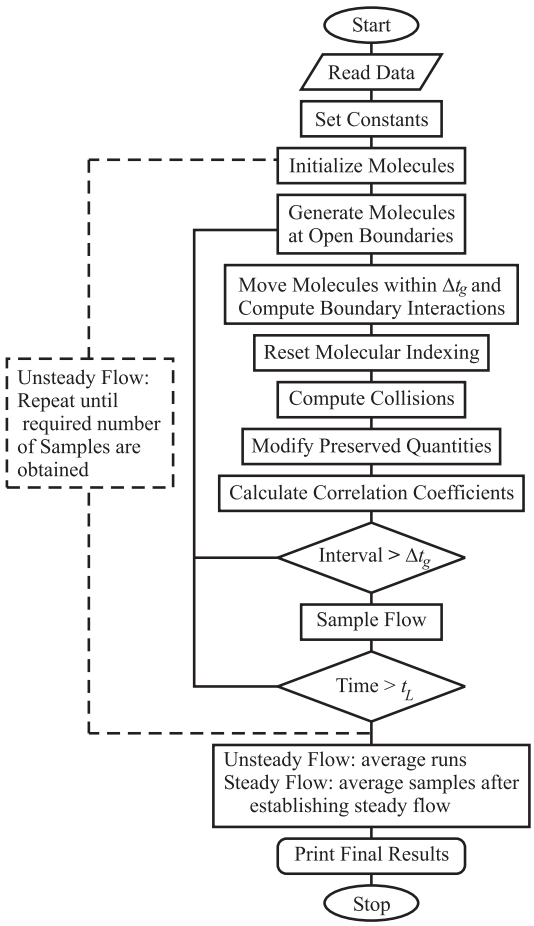

Figure 3-22: Flowchart of OSIP-DSMC operations

pressure). The resulting pressure distributions from the OSIP-DSMC, DSMC, and BTE are presented in Figure 3-24. Considering the nonidealities in the short channels and the degree of scatter in the DSMC, these are in excellent agreement with each other. For the narrower channels, the recirculatory flow was not evident, but may be observed in the 1 μm wide channel (see Figure 3-18). Sharipov's solution does not provide information regarding the velocity distribution in the flow field, but one may compare the DSMC and OSIP-DSMC solutions and observe that both display recirculatory flow. The maximum velocities predicted by the DSMC are roughly double those predicted by the OSIP-DSMC. However, if we consider the average velocity profile along the channel (excluding the region near the ends) and separate the x- and y-components, we can obtain a clearer comparison of the

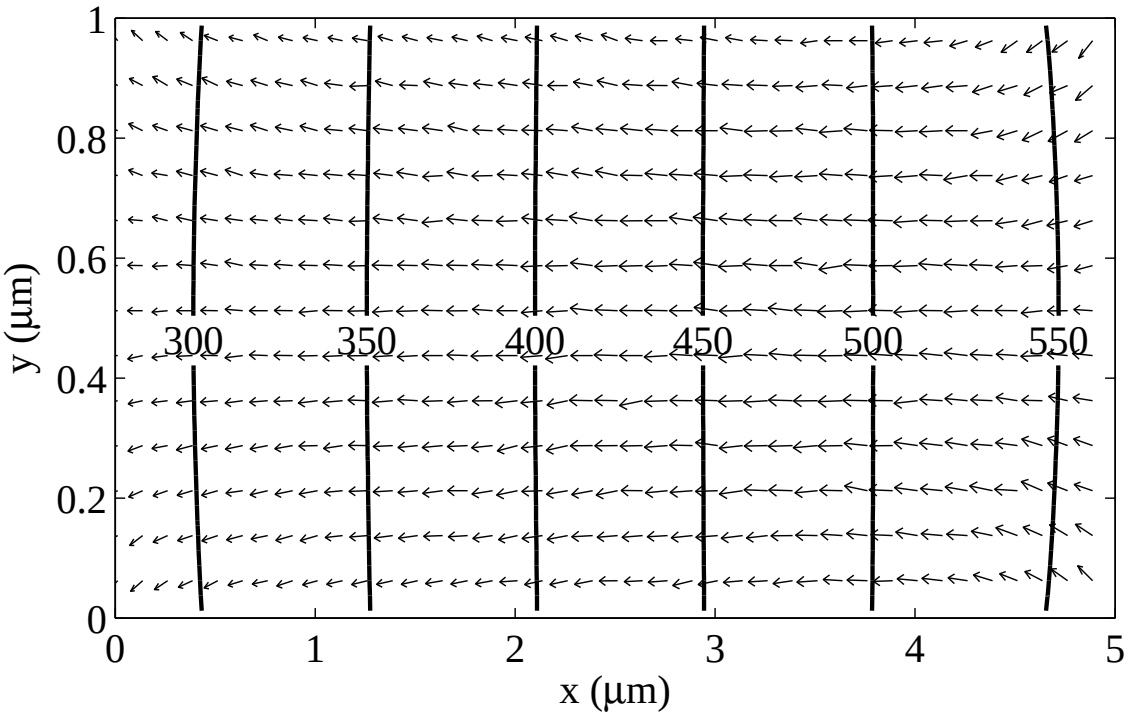

Figure 3-23: Thermal transpiration temperature contour plot (50 K iso-lines, starting at 300 K) and heat flux vectors

DSMC and OSIP-DSMC, as shown in Figure 3-25. The DSMC still displays some scatter, but the similarities in the velocity profiles are apparent. Additional samples would further improve the DSMC results but were not performed at this time.

3.7.2 Temperature Discontinuity: Split Box

Returning to the Split Box problem, the Kn = 0.2 simulation was repeated. Figure 3-26 presents the velocity distribution for this flow, which is comparable in its magnitude and distribution to that reported by Aoki, *et al*. (see Figure 3-20(a)) and the DSMC solution. Figure 3-27 presents a visualization of the correlation coefficients, more precisely the shear components:

$$\tau_{ij}^{cc} = \boldsymbol{c}_i' \boldsymbol{c}_j''' - \delta_{ij} \frac{1}{3} \boldsymbol{c}_i' \boldsymbol{c}_i''' \tag{3.109}$$

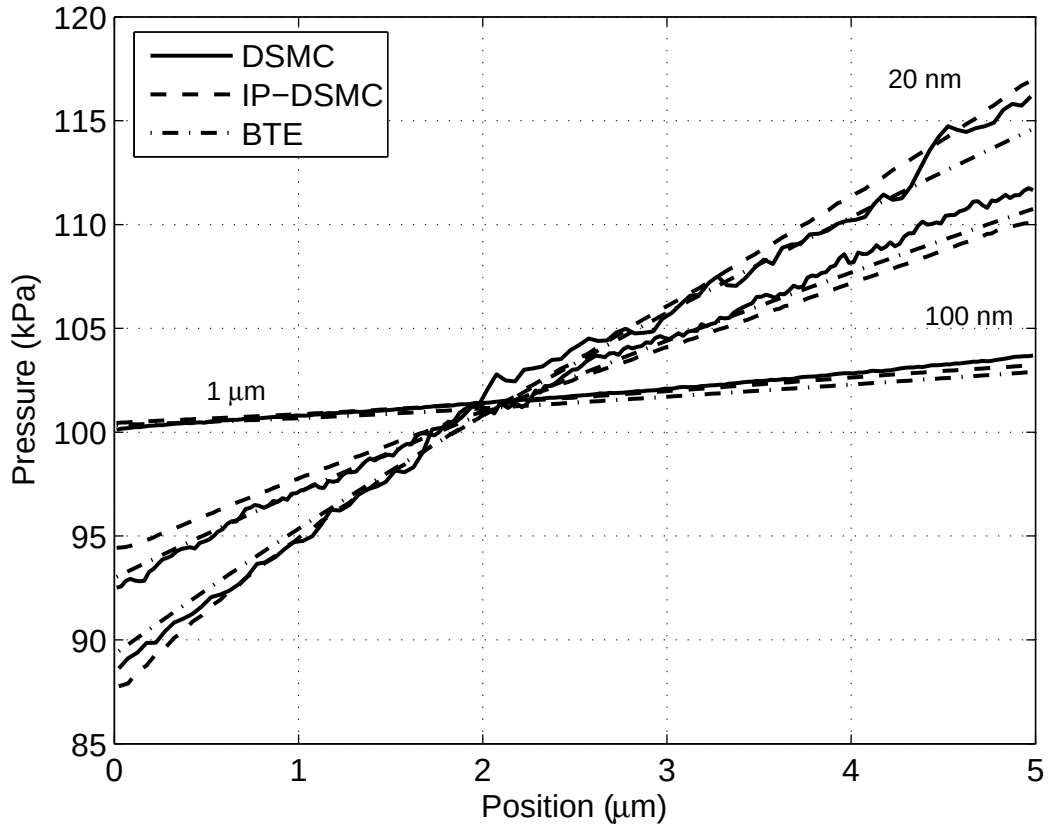

Figure 3-24: Summary pressure distributions for 5 µm long channels comparing DSMC, OSIP, and Sharipov's BTE solutions.

plotted as row vectors (τ_{i1}^{cc}, τ_{i2}^{cc}, τ_{i3}^{cc}). Physically, this may be difficult to interpret as it is the gradients of the correlation coefficients that contribute to the particle modifications, but it does illustrate the effect of the local coordinate system. However, due to the rôle of the correlation coefficients in the pressure (or stress) tensor (see Eq. (3.49)), the correlation coefficient is very closely related to the stress tensor, as may be seen in Figure 3-28 which plots the OSIP-DSMC correlation coefficients and shear stress as scalars (in the manner of Von Mises stress):

$$\sigma' = \sqrt{\frac{\left(\sigma_{xx} - \sigma_{yy}\right)^2 + \left(\sigma_{yy} - \sigma_{zz}\right)^2 + \left(\sigma_{zz} - \sigma_{xx}\right) + 6\left(\tau_{xy}^2 + \tau_{yz}^2 + \tau_{zx}^2\right)}{2}} \tag{3.110}$$

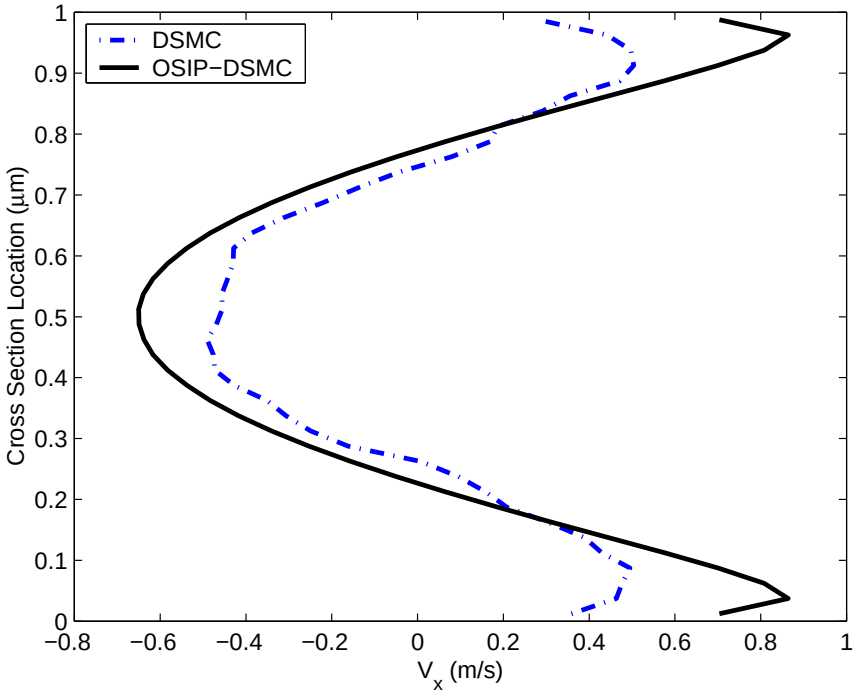

3-25(a): Distribution of the *x*-component of velocity across the width of the channel

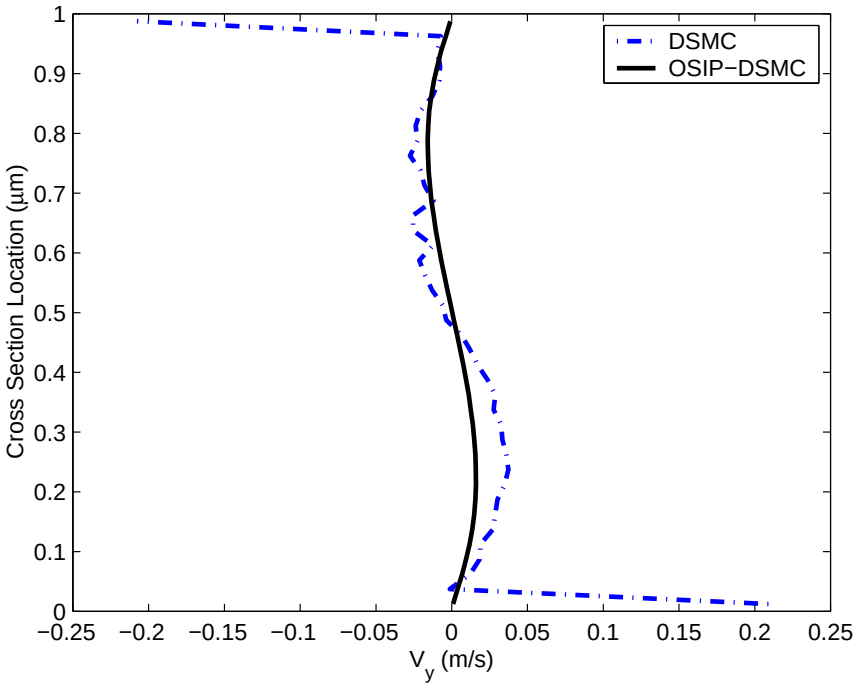

3-25(b): Distribution of the *y*-component of velocity across the width of the channel

Figure 3-25: Velocity distributions across the 1 µm wide channel (averaged over the length of the channel from 0.5 µm to 4.5 µm)

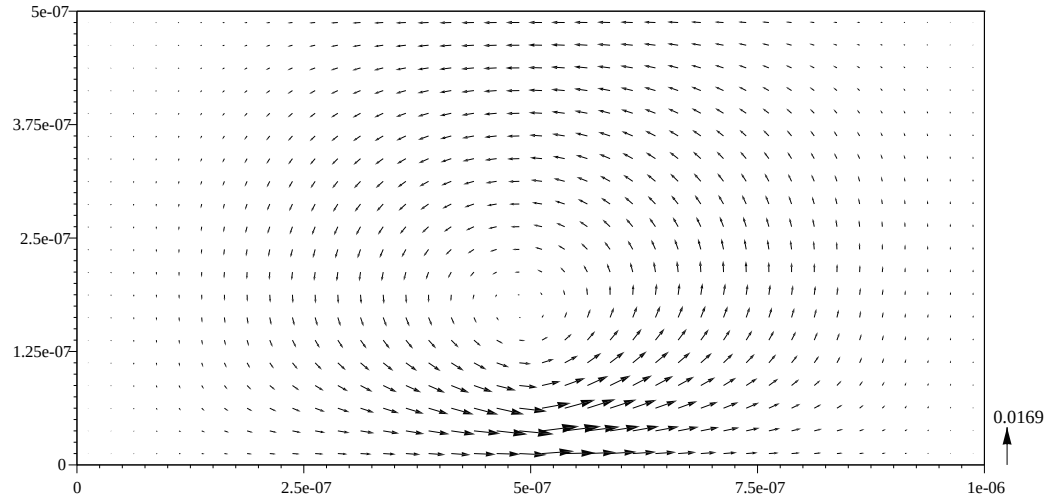

3-26(a): OSIP-DSMC

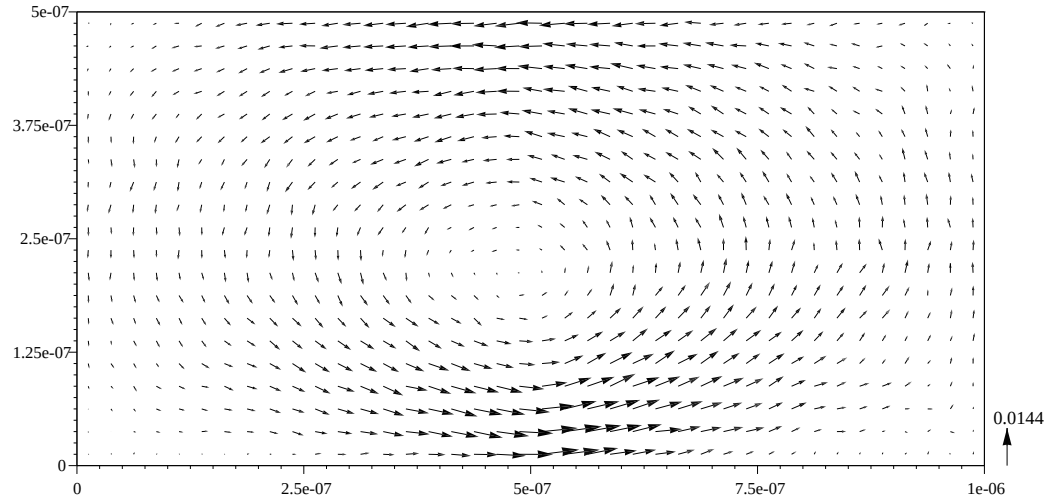

3-26(b): DSMC

Figure 3-26: Simulation of Split Box problem Kn = 0.2, T_1 = 200 K and T_2 = 400 K. Scale vectors indicates maximum scaled velocities

Figure 3-29 presents another Split Box solution for Kn = 0.1. A number of additional flow simulations are presented in Chapter 6.

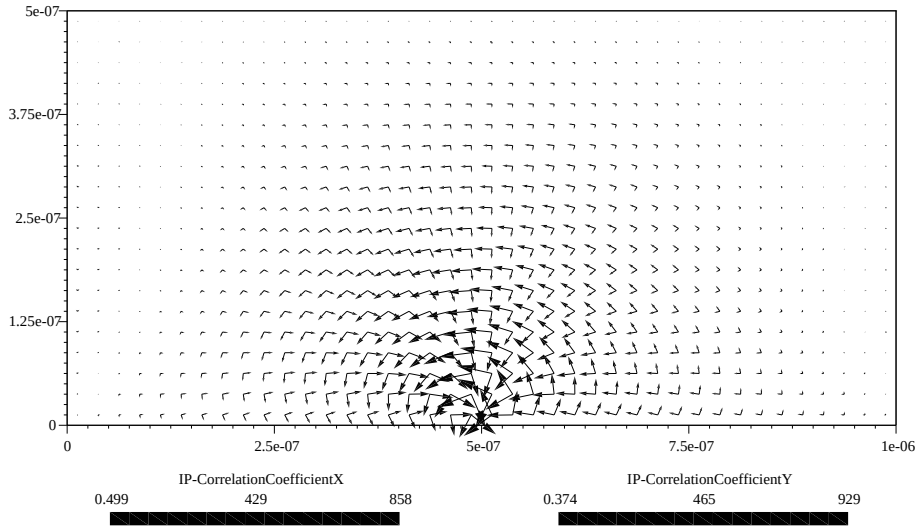

Figure 3-27: Shear components of momentum correlation coefficients for the Split Box problem

3.8 Summary

The IP-DSMC is a very attractive method due to the greatly reduced scatter in sampled quantities. This comes at a price, as a number of assumptions must be made, and as has been seen, certain flow characteristics may be obscured. The Flux Splitting formalized the IP-DSMC method and sought to improve the ability of the IP-DSMC to model non-equilibrium flows by accounting for flow modality. However, the splitting technique used in the Flux Splitting method was still insufficient to recapture contributions to shear components hidden within the preserved temperature by the method. The Octant Splitting IP-DSMC is a significant advance in the IP-DSMC theory and provides a valuable tool for modeling low-speed rarefied gas dynamics, particularly those resulting from thermal stresses.

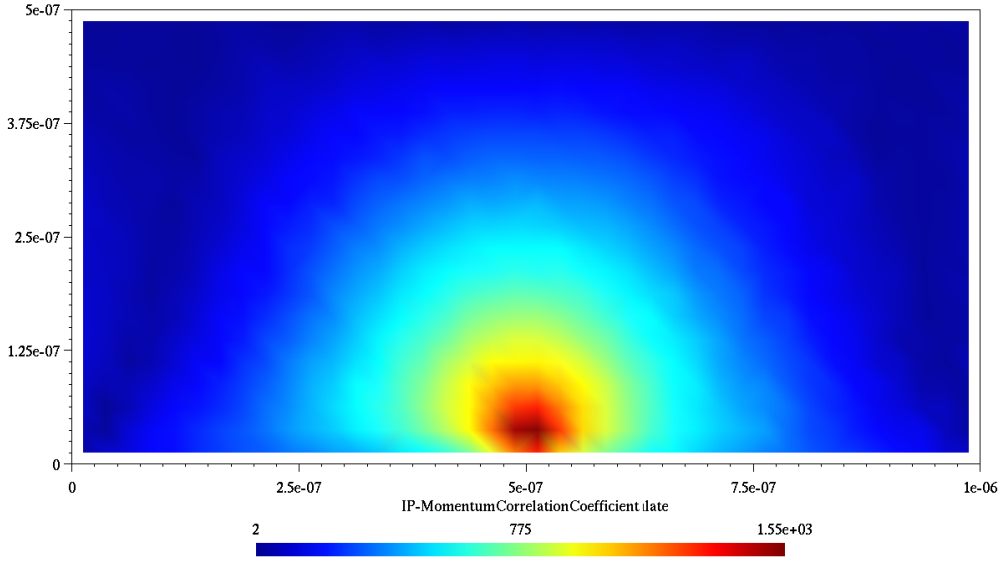

3-28(a): OSIP-DSMC Correlation Coefficients (effective stress)

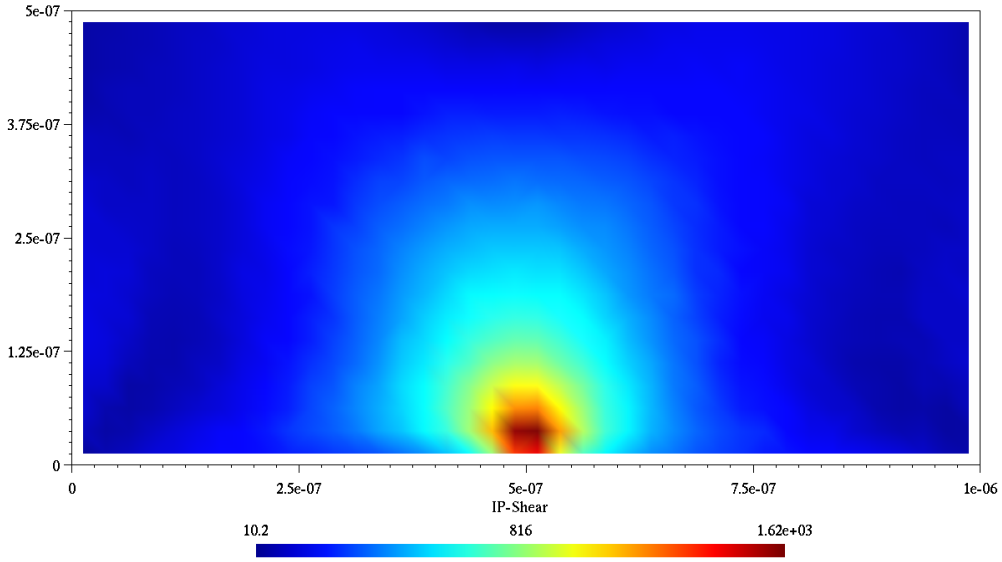

3-28(b): OSIP-DSMC stress (effective)

Figure 3-28: Simulation of Split Box problem Kn = 0.2, T_1 = 200 K and T_2 = 400 K. Scale vectors indicates maximum scaled velocities

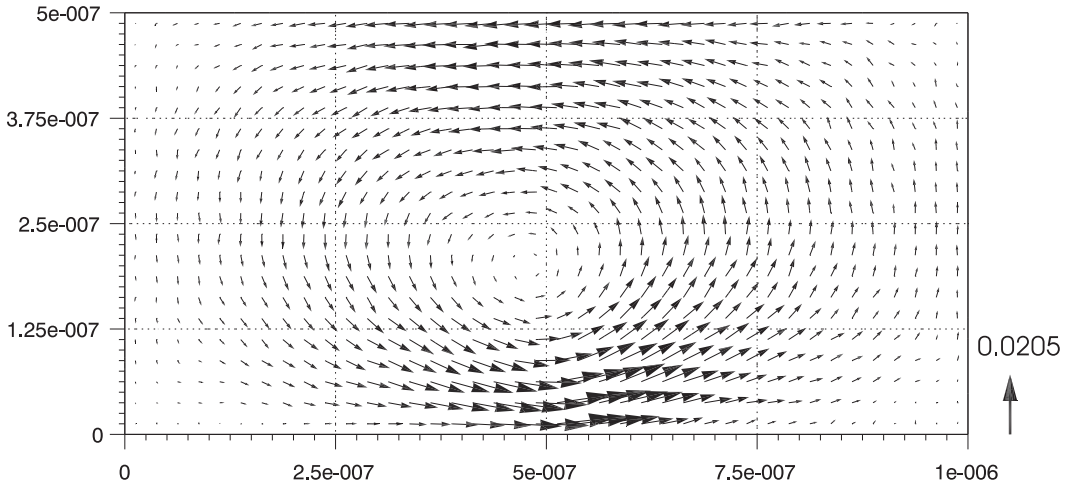

3-29(a): DSMC Velocity Field for Kn = 0.1

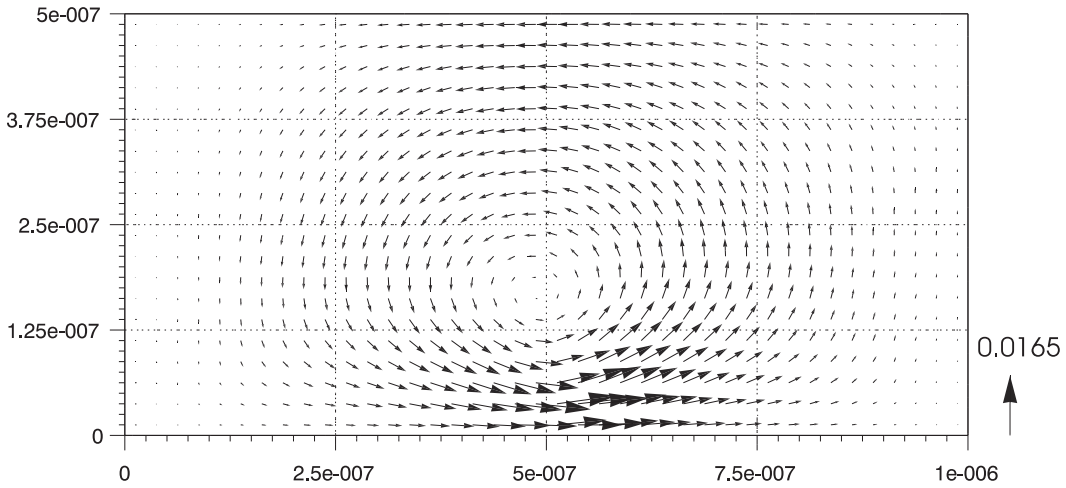

3-29(b): OIP-DSMC Velocity Field for Kn = 0.1

Figure 3-29: Comparison of Velocity fields from DSMC (a), and OIP-DSMC (b). Kn = 0.1

CHAPTER IV

MACROSCALE MODELING

4.1 Boundary Element Method

There are many different numerical techniques which may be used to solve the differential equations with which continuum phenomena are described, including finite difference, finite element, finite volume, *etc*.. Most such method are domain methods, requiring the domain of interest to be discretized in order to form the system of equations. The boundary element method (BEM) provides an alternative: by using the integral form of the governing equations. As a result of the integral formulation the technique operates on the boundary and the problem order is reduced by one—*e.g.*, from 3D to 2D—consequently the resulting systems of linear equations are also reduced in size [10]. As such, it is particularly well suited to problems with infinite or semi-infinite domains. Such problems are quite common in problems of fluidics, heat transfer, electromagnetics. In such problems the boundaries of interest are very small in comparison to the domain, therefore the BEM mesh will be very small, as opposed to domain methods (FEM, FDM, FVM, *etc*.) which require meshing a large region of the domain and possibly the use of special elements to approximate the infinite domain. Although the solution of the BEM formulation is only for the boundary elements, the solution at any point within the domain may be calculated as a continuous function of the boundary solution as a post-processing step. The principal drawbacks of the BEM are the difficulty encountered in performing kernel integrations and the fact that systems of equations (although smaller) are fully dense. Kernel integrations often require special treatment for the singular integrals that arise. A number of accelerations techniques have been proposed to reduce the expense of setting up and solving the dense systems [72, 87].

Many of the previous studies of multiscale modeling of gas phase phenomena have considered channel flow, for which the domain methods may be preferable for continuum modeling. However, many MEMS and NEMS systems operate within what may be considered to be a semi-infinite domain, with small systems fabricated on the surface of (relatively) large surfaces open to an even larger environment. For such problems, the BEM provides a highly efficient continuum modeling technique. To the author's knowledge it has not been been applied to multiscale micro/nanoscale gas phase modeling.

4.2 Constant Element BEM Formulation

The steady state solution of heat conduction and the electrical field can both be described by the Laplace equation.

$$\nabla^2 u = 0 \tag{4.1}$$

The following is a brief review of the Direct BEM formulation for 2D heat transfer problems. This research uses both Direct and Indirect formulations as needed (the Indirect BEM is easier to implement and offers some advantages for treating exterior problems). The Direct BEM utilizes the physically significant quantities of potential (temperature) and flux throughout, whereas the Indirect BEM uses non-physical quantities which are then transformed back to the quantities of interest.

The Direct BEM Integral formulation for the Potential Problem given by

$$p(\xi) = \int_S \left[p(x)F(x,\xi) - q(x)G(x,\xi)\right] \, \mathrm{d}S(x) + \int_V \psi(x)G(x,\xi) \, \mathrm{d}V(x) \tag{4.2}$$

where the 2D kernel, or Green's, functions are

$$G(\boldsymbol{x},\boldsymbol{\xi}) = -\frac{1}{2\pi k} \ln r \tag{4.3}$$

$$F(\boldsymbol{x},\boldsymbol{\xi}) = \frac{(\boldsymbol{x}-\boldsymbol{\xi})_i n_i(x)}{2\pi r^2} = \frac{y_i n_i(x)}{2\pi r^2} \tag{4.4}$$

and $\boldsymbol{x}$ designated the "load" (or "source") point and $\boldsymbol{\xi}$ the "field" (or "evaluation") point, $y_i = \xi_i - x_i$, $r^2 = y_i y_i$, [96], k is the heat transfer coefficient of the medium, and q is the heat

flux. In this study k is calculated using (5.4). Integration is with respect to x and for this case, the second integral on the RHS vanishes as there are no interior sources or sinks. As constant elements will be used, Eq. (4.2) may be rewritten as:

$$\oint_S p(x)F(x,\xi)\,\mathrm{d}S(x) = \frac{1}{2}p(\xi_0) + \int_S p(x)F(x,\xi_0)\,\mathrm{d}S(x) \tag{4.5}$$

which leads to the discretized Boundary Integral formulation for constant elements

$$\frac{1}{2}p(\xi_0^m) = \sum_{n=1}^{N} p^n \int_{\Delta S} F(x^n,\xi_0^m)\,\mathrm{d}S(x) - \sum_{n=1}^{N} q^n \int_{\Delta S} G(x^n,\xi_0^m)\,\mathrm{d}S(x) \tag{4.6}$$

This may now be cast as a matrix problem

$$\frac{1}{2}p^m = \left(\bar{F}^{nm}\right)p^n - \left(\bar{G}^{nm}\right)q^n \tag{4.7}$$

$$\left(F^{nm}\right)p^n - \left(G^{nm}\right)q^n = 0 \tag{4.8}$$

$$\mathbf{F}^s\boldsymbol{p} - \mathbf{G}^s\boldsymbol{q} = 0 \tag{4.9}$$

where the matrices $\mathbf{F}^s$ and $\mathbf{G}^s$ are populated by the kernel integrations, and the vectors $\boldsymbol{p}$ and $\boldsymbol{q}$ are the potentials (temperatures) and fluxes at the boundary elements. For mixed boundary conditions, entries in the two system matrices are interchanged to form the right and left hand sides and the system may be solved numerically. Eq. (4.2) may now be used to calculate the temperature at any point $\boldsymbol{\xi}$ interior to the domain. The fluxes interior may be calculated from

$$q(\boldsymbol{\xi}) = \int_S \left[p(x)H(x,\xi) - q(x)F(x,\xi)\right]\,\mathrm{d}S(x) + \int_V \psi(x)F(x,\xi)\,\mathrm{d}V(x) \tag{4.10}$$

where the kernel function H is given by

$$H(x,\xi) = \frac{k}{2\pi r^2}\left(\frac{2y_iy_j}{r^2} - \delta_{ij}\right)n_i(x)n_j(\xi) \tag{4.11}$$

Kernel integrations may be either numerical or for special cases (as for the constant valued elements used in this research) analytic.

4.3 Summary

The BEM provides an efficient modeling technique for certain physical problems, by reducing the dimensionality of the problem by one. It will be used in the next chapter as a novel and efficient technique for multiscale modeling of rarefied gas dynamics.

CHAPTER V

MULTISCALE MODELING OF A TSAFM CANTILEVER

The goal of Multiscale modeling is to utilize the most efficient models that are applicable to the various flow regimes of interest and couple these to obtain a solution for the over flow. In this chapter a detailed OSIP-DSMC/BEM coupled model for the heat transfer and thermally driven flow will be developed and evaluated. However, prior to introducing the coupled model, the development and results of a preliminary modeling effort will be presented. This will provides a point of comparison for the full coupled model.

5.1 Preliminary Modeling: TSAFM Sensitivity

The following sections describing the preliminary model are extracts from a paper entitled "The impact of subcontinuum gas conduction on topography measurement sensitivity using heated atomic force microscope cantilevers," by the current author and Drs. Wenjing Ye and William P. King. This work has been published in the Journal *Physics of Fluids* [67] .

5.1.1 Introduction

The scanning probe microscope is likely the most widely used scientific instrument for nanometer-scale sensing and manipulation. It has had profound effect on the metrology and fabrication of microelectronics and microelectromechanical systems—with the ability to measure [14] and modify [113] nanometer-scale surface features and characteristics. In atomic force microscopy (AFM), a cantilever probe having a tip of near-atomic sharpness is scanned across a nanostructured surface as a sensor detects the vertical tip position. Various methods have been developed to detect the motion of or forces on the probe tip as it

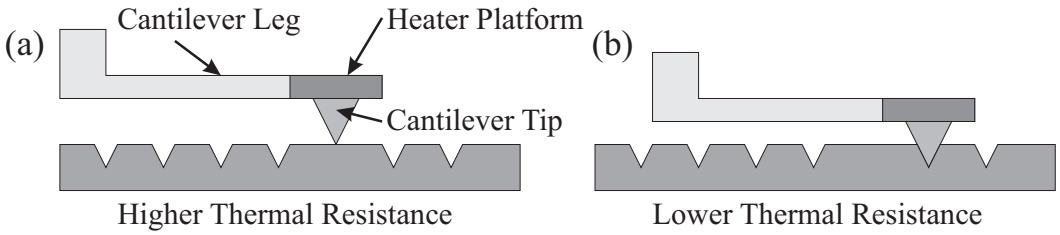

Figure 5-1: Diagram of TSAFM Operation. A heated cantilever is scanned across a nanostructured surface (a). As the proximity changes, the thermal resistance changes (b).

follows the surface contours including laser illumination with optical detection [14], integrated piezoresistors [44], and current tunneling [15]. Thermal Sensing Atomic Force Microscopy (TSAFM) is a recent development in scanning probe microscopy that has arisen from the use of AFM heater-cantilevers for high density read/write data storage [106, 13]. In TSAFM, the temperature of a heated cantilever probe is governed by heat flux from the cantilever to the nearby substrate, and can therefore measure proximity between the cantilever and the surface over which it scans. The cantilevers are made from electrically active doped silicon to allow resistive heating and monitoring of temperature-dependent electrical resistance. Imaging requires only electrical signals to and from the cantilever. This removes the need for optical access, simplifies the system, and enables the implementation of heater cantilever arrays capable of parallel operation.

Although similar in many ways to conventional AFM systems, a description of the form and function of TSAFM systems serves to clarify the motivation and the direction of this study. The AFM heater-cantilever sensor is an electrically conductive V-shaped microcantilever with a sharp tip, as shown in Figure 5-1. The tip is typically 500 nm high with a nominal radius of curvature at the point of 20 nm. In operation, the cantilever is biased with an electrical voltage resulting in resistive heating near the cantilever tip, reaching thermal equilibrium with the environment within 1 ms [52, 27]. The localized heating is due to nonuniform impurity doping: low doping concentrations near the tip result in high electrical resistance while high doping in the legs produces lower resistance.

This heating affects the temperature-dependent electrical resistivity of the cantilever. As the heated cantilever tip is scanned across a nanostructured surface, the tip follows the surface contours such that the distance between the heater platform and the surface changes. This alters the thermal impedance between the cantilever and the substrate and consequently the steady-state temperature profile and the electrical resistance of the cantilever. Thus, the proximity to the surface can be sensed via the temperature-dependent electrical resistance.

Correct interpretation of the cantilever temperature signal and the rational design of cantilevers for improved sensing require accurate models of the heat transfer. Prior modeling efforts have used both analytical and finite difference formulations and considered steady-state and transient cantilever heating [52, 27, 26] although only two have considered reading sensitivity [52, 27]. All have assumed continuum gas phase heat transfer. The cantilever-substrate distance is governed by the height of the tip, nominally 500 nm. Sensitivity increases for decreasing tip height. Under standard atmospheric conditions in which heater cantilevers are usually operated, the gas molecular mean free path λ is approximately 64 nm [50]. For a separation of $g = 500$ nm the Knudsen number is $\mathrm{Kn} = \lambda/g \approx 0.13$, which indicates that the flow is in the transition regime. Smaller gaps will approach free molecular flow. Improved heat transfer modeling is thus required to predict the behavior of heater cantilevers within these noncontinuum flow regimes. This paper describes the investigation of subcontinuum gas phase heat transfer on the behavior of heated AFM cantilevers and seeks to improve the design of heater cantilevers operated in the range of $\mathrm{Kn} \sim 0.1 - 1$.

5.1.2 Heat Transfer Modeling

The V-shaped cantilever is modeled as a rectangular beam with the heater platform located at its center. Figure 5-2 shows the one dimensional conservative finite difference model used to evaluate heat transfer and to predict the temperature profile along the cantilever. The finite difference formulation accounts for the heat generation within each element ($q_{gen,i}$) with the heat transfer along the cantilever (q_{i-1}, and q_{i+1}), to the environment ($q_{e,i}$), and to

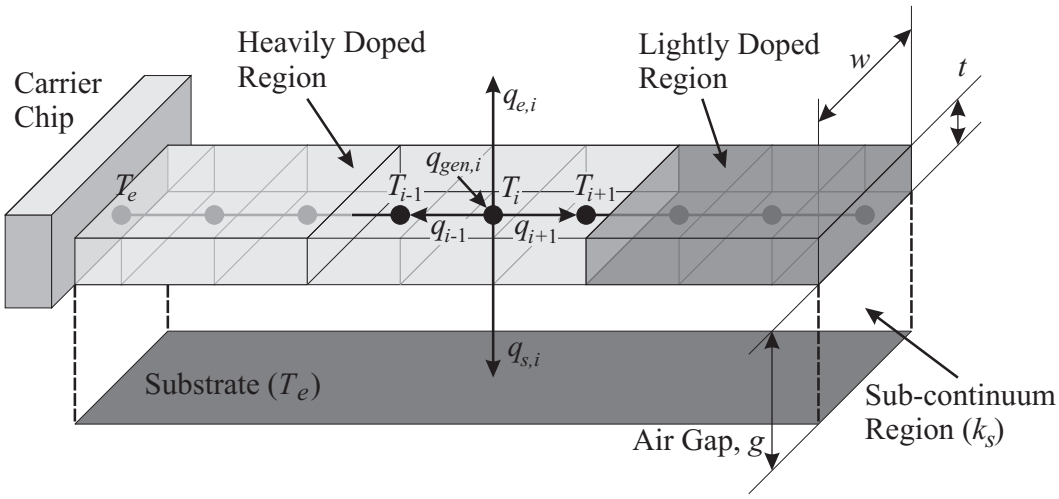

Figure 5-2: Diagram of Thermal Sensing Atomic Force Microscope (TSAFM) finite difference model showing nodes, temperatures, heat generation ($q_{gen,i}$), and heat transfer (with paths q_{i-1} and q_{i+1} along the cantilever, $q_{e,i}$ to the environment and $q_{s,i}$ to the surface) used in the formulation. The region immediately below the cantilever must be considered as subcontinuum due to the small air gap, g.

the surface ($q_{s,i}$) as illustrated in Figure 5-2 and considers continuum and noncontinuum gas phase heat transfer. Prior studies [52, 106, 27, 26, 64] have shown that conduction through the tip and radiative heat transfer may be neglected. For gaps smaller than $\sim$ 10 nm, near-field radiative effects may become significant [70, 36]. Thus, the dominant mode of heat transfer is gas phase conduction. A conduction shape factor [47] combines $q_{e,i}$ and $q_{s,i}$, such that the total continuum gas phase heat transfer per unit length (W/m) to the surface and environment is

$$q'_{s,i} + q'_{e,i} = S\,k_c\,(T_B - T_E) = S\,k_c \Delta T \longrightarrow S = \frac{q_{s,i} + q_{e,i}}{k_c \Delta T} \tag{5.1}$$

where k_c is the continuum heat transfer coefficient (W/m-K), and T_B and T_E are the beam and the ambient temperatures (K), respectively.

A 2D finite element analysis (FEA) determines the shape factor for a given cross section geometry and separation gap. The FEA model consists of a rectangular body with

cross section width, w, and thickness, t, parallel to a surface (substrate) at a distance g, embedded in a semi-infinite medium, as in Figure 5-2. The body is maintained at a uniform temperature T_B, whereas the substrate is maintained at T_E, and the medium has uniform thermal properties. Shape factors are calculated for each combination of beam geometry and separation distance used in this study. Meshes were refined for the smallest separation geometry until a converged solution was obtained, and this level of refinement was then maintained for subsequent shape factor calculations. The conductance per unit length of the cantilever can thus be expressed as $G' = k_c S$, where k_c is the continuum heat transfer coefficient.

Previous studies assumed the temperature to be uniform across the cantilever with the Biot number, $\mathrm{B_i} \ll 1$, and good a agreement between modeling and measurement was observed. Here we confirm this to be appropriate for the present study. The Biot number, $\mathrm{B_i} = h_{eff} L_c / k_s$, compares the thermal conductance of the gas and the cantilever. First, consider the "convective" coefficient h_{eff} (W/m^2-K) which is defined as

$$q' = S k_c \Delta T = 2 (w + t) h_{eff} \Delta T \longrightarrow h_{eff} = \frac{S k_c}{2 (w + t)} \tag{5.2}$$

where w and t are the cantilever width and thickness and k_c is the conductive heat transfer coefficient for the gas. The following values provide an upper bound for h_{eff}: $k_c \sim$ 0.04 W/m-K (approximate value for Argon at 1600 K, see Eq. (5.4)), $S \approx 2000$ (corresponding to a gap of 5 nm), $w = 10$ µm, and $t = 200$ nm, yielding $h_{eff} \approx 4 \times 10^6$ W/m^2-K. The heat transfer coefficient, k_s, of the silicon cantilever is approximately 80 W/m-K and $L_c = A_c / P = wt/(2(w + t))$ will be used for the characteristic length. The resulting Biot number, $\mathrm{B_i} \approx 0.005$, is quite small, indicating that the uniform temperature distribution in the cross section is appropriate.

The shape factor accounts for the continuum gas phase heat transfer from the cantilever and a correction must be made to include subcontinuum effects. In the finite element simulations for the shape factor it has been observed that the heat flux in the region immediately

beneath the cantilever is essentially uniform and one dimensional except for a small "fringing" region near the edge of the cantilever. If the assumption is made that the heat transfer in the region immediately beneath the cantilever is in fact one dimensional, then an approximate correction to the thermal conductance may be made by replacing the effective 1D continuum conductance ($G' = k_c w/g$, under the beam) with the corresponding subcontinuum conductance,

$$G' = q'/\Delta T = k_c \left(S - \frac{w}{g} \right) + k_{eff} \frac{w}{g} \tag{5.3}$$

where k_{eff} is the effective subcontinuum conduction heat transfer coefficient, for which an accurate model is provided as described below. As a check, a second set of shape factors, S', was calculated that excluded the region beneath the cantilever, i.e., considered only the heat transfer from the top and side. This was then corrected by adding the effective 1D shape factor for the region under the beam ($S_c = S' + w/g$). This was found to agree with the normal (continuum) shape factor to within 3% for all geometries. At a minimum, the assumption of 1D heat transfer requires that the gap and cantilever thickness both be small compared to the width of the cantilever—which is the case for all geometries in this study.

5.1.3 Subcontinuum Heat Transfer

Two different techniques were used to evaluate the one dimensional subcontinuum heat transfer for the region immediately beneath the cantilever: Direct simulation Monte Carlo (DSMC) and a kinetic theory based macromodel.

5.1.3.1 DSMC

The DSMC code is implemented in C++ and provides user selectable dimensionality for 1D, 2D, or 3D simulations and implements the major collision models: Hard Sphere (HS), Variable Hard Sphere (VHS), and Variable Soft Sphere (VSS). The Hard Sphere model treats the molecules as elastic particles with constant cross diameters [17]. The Hard Sphere molecular diameter and mass of Argon are $d = 3.63 \times 10^{-10}$ m, and 66.3×10^{-27} kg. The Variable Hard Sphere [17] and Variable Soft Sphere [17, 56] models were developed to

more accurately simulate the temperature-dependence of the viscosity of real gases. However for Argon and the temperature range typically encountered in TSAFM operation, the Hard Sphere model would provides slightly improved efficiency with little loss of accuracy [41].

DSMC simulations were performed for a wide range of temperature differences and gaps to obtain the effective heat transfer coefficient for each case. The subcontinuum region was treated as one dimensional, and the computational domain divided into 100 cells spanning the gap ($\Delta x = L/100$) with each cell initially containing 100 particles and the time steps set to ensure that particles would require approximately five time steps to traverse a cell. This meets recommended criteria for minimizing the truncation error associated with the DSMC method [43] as follows: 1. the cells were smaller than the mean free path, specifically for all gaps, where λ is the average value for the undisturbed gas and 2. the time step was much smaller than the mean free time ($\Delta t = (\Delta x/5c_0) < \lambda/(7c_0)$, where $c_0 = \sqrt{2RT}$). Between 100,000 to 300,000 iterations were performed for each simulation to ensure that steady-state was achieved and that statistical noise was minimized. Furthermore, four independent runs were averaged together to further improve the final results. The normalized standard deviation of the effective heat transfer coefficients for these independent simulations was less than 1%. This can be further reduced by increasing the number of particles per cell and/or the number of samples as the statistical error is inversely proportional to the square root of the number of particles per cell and the number of samples [41].

5.1.3.2 Macromodel

Although the DSMC provides considerable insight into the behavior of rarefied gases, revealing characteristics that might not be observable otherwise, it is computationally expensive. One way to overcome this obstacle is to perform a large number of simulations over a wide range of possible conditions and then interpolate these results for use in the cantilever

heating model. However, an analytic equation capable of describing the subcontinuum heat transfer would be advantageous.

The proposed macromodel first considers the limiting cases of continuum and free molecular heat transfer, which correspond to Kn $\ll$ 1 and Kn $\gg$ 1 respectively. From kinetic theory, the effective heat transfer coefficient, defined as $k_{eff} \equiv q''L/(T_H - T_L)$, of a continuum gas bounded by parallel surfaces maintained at temperatures T_L and T_H ($T_H > T_L$) can be written as:13

$$\overline{k} = \frac{15\,(9\gamma - 5)\,k_B}{128 d^2} \sqrt{\frac{k_B T_{eff,c}}{\pi\, m}} \tag{5.4}$$

where γ is the specific heat ratio, cp/cv ($\gamma = 5/3$ for monatomic species), k_B is Boltzmann's constant, $T_{eff,c} = (T_H + T_L)/2$ is the effective, or average, temperature and d and m are the effective molecular diameter and mass of the gas, respectively [50].

The free molecular heat flux for the same surfaces can be evaluated as [40]:

$$q''_{fm} \approx \alpha n k_B \sqrt{\frac{k_B}{2\,\pi\, m}} \left(\frac{\gamma + 1}{\gamma - 1}\right) \frac{\sqrt{T_H T_L}}{\sqrt{T_L} + \sqrt{T_H}} (T_H - T_L) \tag{5.5}$$

where α is the accommodation coefficient of the walls which is assumed to be $\alpha = 1$ in this study, i.e., fully accommodating and n is the number density of the gas ($n = \rho/m$). The heat flux is independent of separation which is consistent with the collisionless nature of the free molecular regime.

A macrorule may be formed by applying Matthiessen's Rule, which has long been used to treat length scale dependent effects in electrical and thermal resistance [54, 23], resulting in the following form:

$$k_{eff} = \frac{k^\star}{l} \left(\frac{1}{l} + \frac{1}{L}\right)^{-1} \tag{5.6}$$

Where L, l, and $k^\star$ represent the macroscopic and microscopic length scales and the reference heat transfer coefficient, respectively. At this point in the derivation, these quantities are undetermined. In the continuum limit it is assumed that $L \ll l$, therefore

$$k_{eff} = \lim_{L \ll l} \frac{k^\star}{l} \left(\frac{1}{l} + \frac{1}{L}\right)^{-1} \rightarrow k^\star \tag{5.7}$$

From which it is obvious that $k^\star$ must equal $\overline{k}$. A reasonable choice of the macroscopic length scale, L, in this 1D problem is the separation gap, g. To identify the microscopic length scale, consider the heat flux in the free molecular limit, $g \ll 1$. The macromodel gives

$$q'' \approx \lim_{g \ll l} \frac{\overline{k}}{l}\left(\frac{1}{l}+\frac{1}{g}\right)^{-1}\frac{\Delta T}{g} \rightarrow \frac{\overline{k}}{l}(g)\frac{\Delta T}{g} = \frac{\overline{k}}{l}\Delta T = \frac{\overline{k}}{l}(T_H - T_L) \tag{5.8}$$

Equating this to Eq. (5.5) and solving for l, one has

$$l = \frac{1}{\sqrt{2}nd^2}\frac{15\sqrt{2}(9\gamma-5)(\gamma-1)\sqrt{T_H+T_L}\left(\sqrt{T_H}+\sqrt{T_L}\right)}{128\alpha(\gamma+1)\sqrt{T_H T_L}} \tag{5.9}$$

The kinetic definition of the mean free path[in general the mean-free path—as a function of the number density n—is dependent on the gas state (temperature, pressure, *etc.*); in this study the average number density and mean-free path of the gas at standard temperature and pressure are used], $\lambda = \left(\sqrt{2}\pi nd^2\right)^{-1}$, can be identified in this equation after multiplying the numerator and denominator by π, allowing it to be reduced to

$$l = \lambda\left(\frac{15\pi\sqrt{2}(9\gamma-5)(\gamma-1)\sqrt{T_H+T_L}\left(\sqrt{T_H}+\sqrt{T_L}\right)}{128\alpha(\gamma+1)\sqrt{T_H T_L}}\right) = \lambda C \tag{5.10}$$

Where the coefficient C is now defined as

$$C = \frac{15\pi\sqrt{2}(9\gamma-5)(\gamma-1)\sqrt{T_H+T_L}\left(\sqrt{T_H}+\sqrt{T_L}\right)}{128\alpha(\gamma+1)\sqrt{T_H T_L}} \tag{5.11}$$

Based on these results the final form of the macrorule is

$$k_{eff} = \frac{\overline{k}}{\lambda C}\left(\frac{1}{\lambda C}+\frac{1}{g}\right)^{-1} = \frac{\overline{k}}{\lambda}\left(\frac{1}{\lambda}+\frac{C}{g}\right)^{-1} \tag{5.12}$$

Eq. (5.12), should now account for the effects of the length scale, surface accommodation, and temperature on the effective heat transfer coefficient. Figure 5-3 shows the resulting effective heat transfer coefficient, k_{eff}, for a number of gaps ranging from 10 nm to 1 μm as predicted by the DSMC and macromodel. The working gas is Argon with an average density of 1.78 kg/m^3 and the boundaries are fully accommodating with a temperature difference ΔT = 300 K (T_L = 273 K). The bounds of the simulation regime

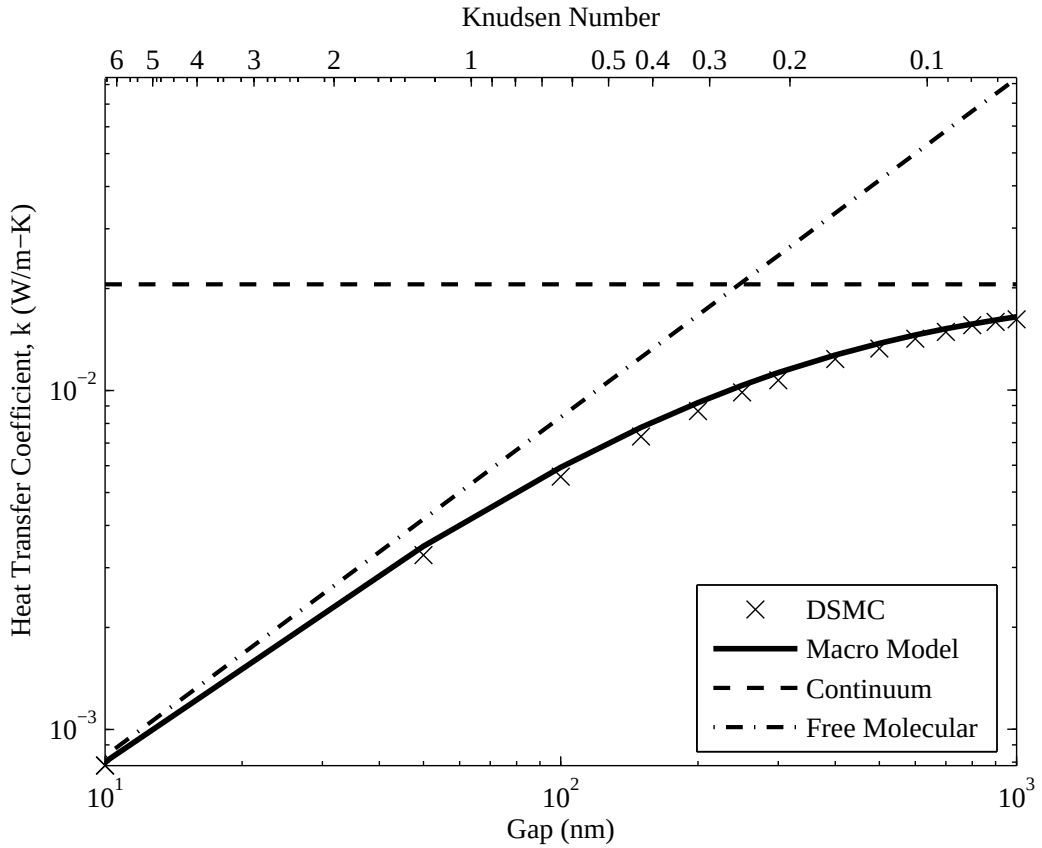

Figure 5-3: The effective heat transfer coefficient, k_{eff}, of argon as modeled by the DSMC, kinetic theory macromodel, continuum and free molecular models, for the case of ρ = 1.78 kg/m^3, T_H = 573 K, T_L = 273 K, and a range of separation gaps.

correspond to Kn $\gg$ 1 and Kn $\ll$ 1. In light of the excellent agreement of the macrorule with the DSMC simulations the macro rule is used for all further subcontinuum modeling in this study. An alternative formulation based on the Smoluchowski equation [29] may be manipulated to obtain Eq. (5.12). However, Eq. (5.12) provides additional insight into the length scale dependence of the heat transfer coefficient. Denpoh also explored the effect that the accommodation coefficient has on the heat transfer [29].

5.1.4 Subcontinuum Thermal Conductance of TSAFM FDM Element

It is possible to use the effective subcontinuum heat transfer coefficient k_{eff} to explore the subcontinuum thermal conductance in the framework of the finite difference model. The

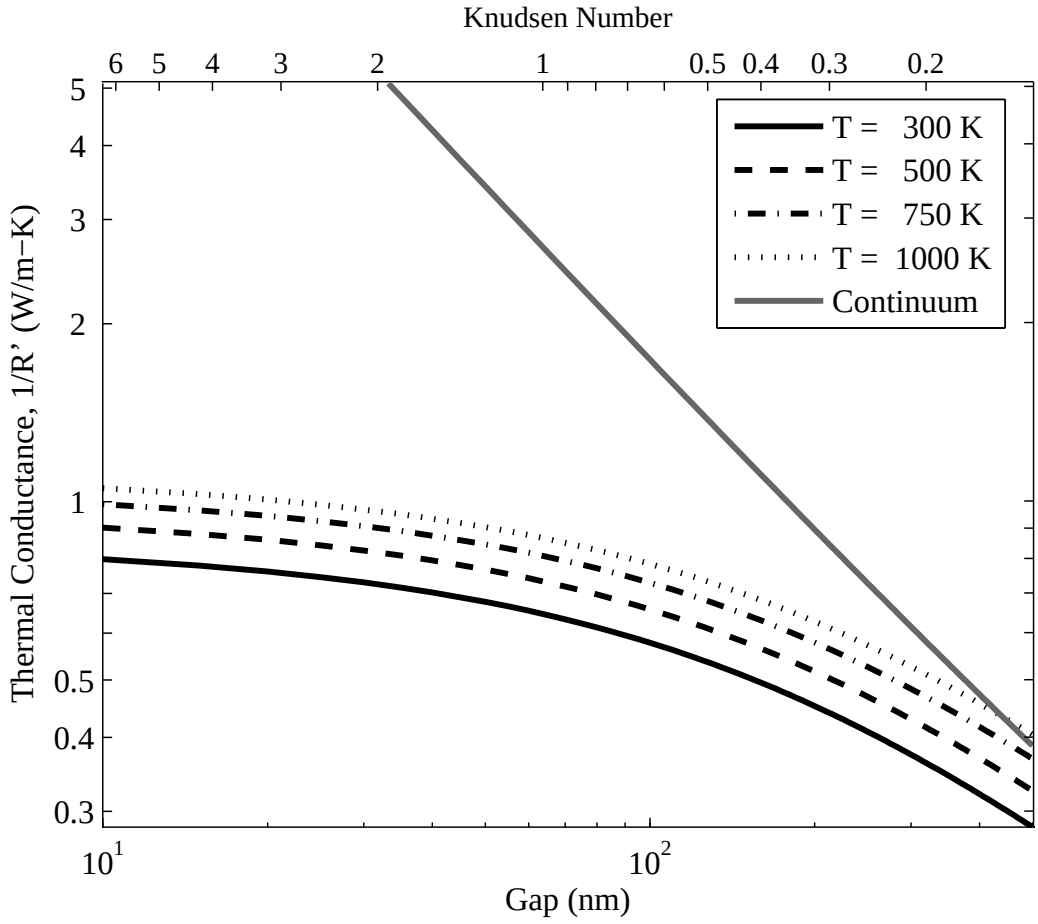

Figure 5-4: The thermal conductance (per unit length), G' , evaluated using continuum and subcontinuum models. The subcontinuum conductance is plotted for a number of temperatures (300, 500, 750, and 1000 K, with T_L = 273 K) whereas the continuum conductance is plotted for T_H = 300 K only.

thermal conductance per unit length, G' , for an element may be calculated by substituting the value of k_{eff} into Eq. (5.3). Figure 5-4 shows values of G' over a range of gaps from 10 nm to 500 nm, with w = 10 μm and t = 200 nm. Figure 5-4 also shows the uncorrected continuum conductivity. From these results we conclude that subcontinuum heat transfer effects must be included in order to correctly model TSAFM behavior for cantilever-substrate distances less than 200 nm.

Table 5-1: Table 1. TSAFM Cantilever Design Parameters

Parameter	Millipede	Design 2
Leg Length	50 μm	50 μm
Leg Width	10 μm	10 μm
Leg Thickness	200 nm	200 nm
Leg Doping	1×10^{20} cm^{-3}	1×10^{20} cm^{-3}
Heater Length	10 μm	20 μm
Heater Width	5 μm	10 μm
Heater Thickness	200 nm	200 nm
Heater Doping	1×10^{18} cm^{-3}	1×10^{18} cm^{-3}

5.1.5 Results and Discussion

The finite difference model, which includes the embedded subcontinuum model, can now be used to simulate TSAFM operation, including the steady-state temperature profile and electrical response. The electrical resistivity, which affects the heat generation term ($q_{gen,i}$), has a well characterized dependence on doping concentration and temperature [48]. This dependence is highly non-linear and thus requires an iterative solution technique to obtain the steady-state temperature profile and electrical resistance. Table 5-1 presents the design parameters for two cantilever designs: the data storage cantilever known in the literature as "Millipede" and an alternate design 2. The purpose for design 2 is to investigate the effect on the sensitivity of increasing the heater area without altering the room-temperature electrical resistance. Sensitivity is defined as the change in measured voltage resulting from a change in the air gap ($\Delta\mathcal{V}/\Delta g$). Predictions were made for cantilever operation over a range of separation gaps and heating currents. The finite difference model is implemented in MATLAB and the meshes, which are symmetric about the center of the heater, consist of 200 elements for the leg and 50 elements for the heater. Mesh refinement was determined by a convergence study. A 5 nm perturbation to the gap calculates the sensitivity, which is approximated as $S \approx (\mathcal{V}(g+\Delta g) - \mathcal{V}(g))/\Delta g$. Total computation time for the two designs was approximately 10 hours on an AMD Athlon XP 1900 (1.6 GHz).

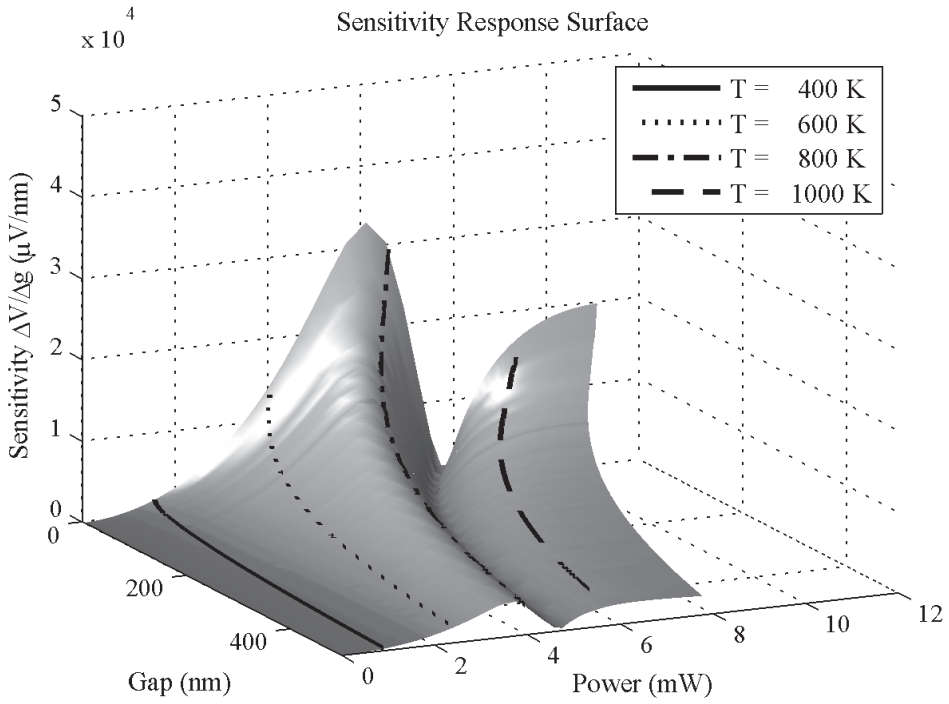

Figure 5-5: Sensitivity response surface and constant temperature curves for the Millipede design.

Figure 5-5 shows the sensitivity response surface for the Millipede design as a function of cantilever-substrate gap height and cantilever heating power. Superimposed on this surface are constant temperature lines representing the maximum predicted temperature at the cantilever tip for each operational point. In general, sensitivity increases as the gap decreases. As a function of power, the sensitivity increases until it reaches a ridge of maximum sensitivity, beyond which the sensitivity then drops off sharply to a trough of minimum sensitivity followed by a second region of increasing sensitivity. These features tend to coincide with the constant temperature lines. To understand this behavior it is necessary to consider the electrical resistivity, ρ_e , and the absolute value of its temperature derivative, $|\partial\rho_e/\partial T|$, as plotted in Figure 5-6 as functions of temperature for the doping concentrations used in this study. Comparing Figures 5-5 and 5-6, it becomes apparent that the sensitivity has a strong correlation with the temperature derivative of the resistivity. In

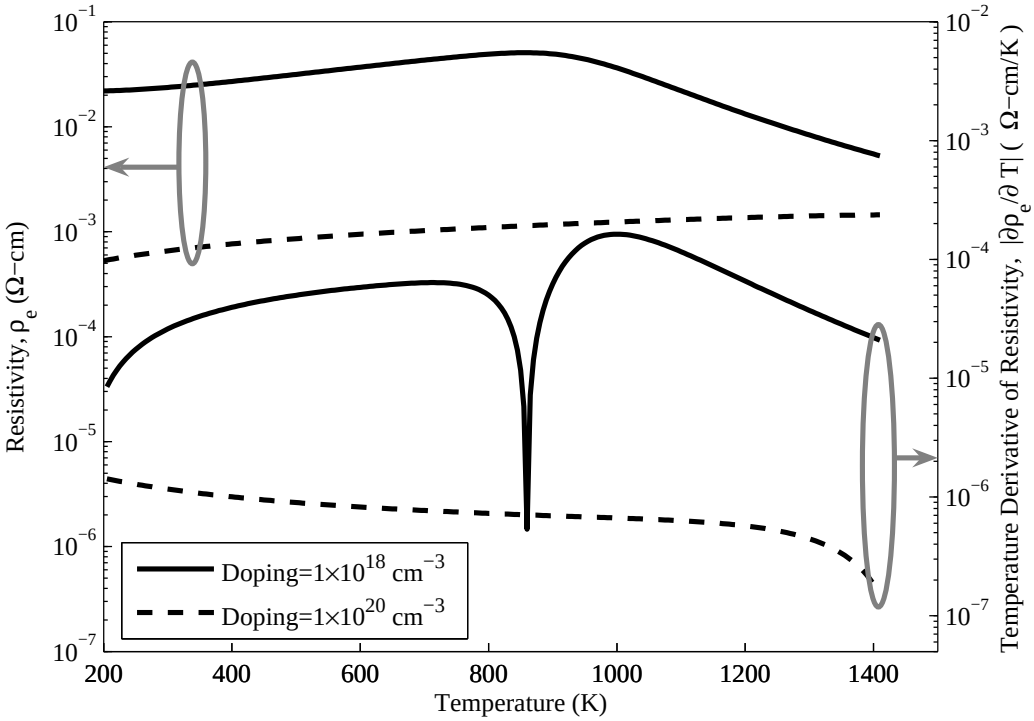

Figure 5-6: Cantilever electrical resistivity as a function of cantilever maximum temperature for the doping concentrations used in the Millipede and Design 2 designs.

Figure 5-5 the sensitivity increases with increasing power until the temperature approaches 750 K. This corresponds to the increasing derivative of the resistivity for the lightly doped (10^{18} cm^{-3}) heater region shown in Figure 5-6. Beyond this point the sensitivity falls off sharply, reaching a local minima at around 900 K, again corresponding well with the temperature at which the slope of the resistivity changes sign and $|\partial\rho_e/\partial T|$ reaches a minimum, at around 850 K. The slight discrepancy in these temperatures is likely due to the highly doped region playing a larger role in the sensitivity around these temperatures. The sensitivity and $|\partial\rho_e/\partial T|$ then increase again with increasing temperature. However, this may be considered infeasible as in operation the temperature should not exceed 750 K to avoid thermal damage and power consumption should not exceed 3 mW.

Figure 5-7 shows the response of design 2. A similar response is predicted, albeit with a higher maximum sensitivity and higher power consumption. Constant temperature lines

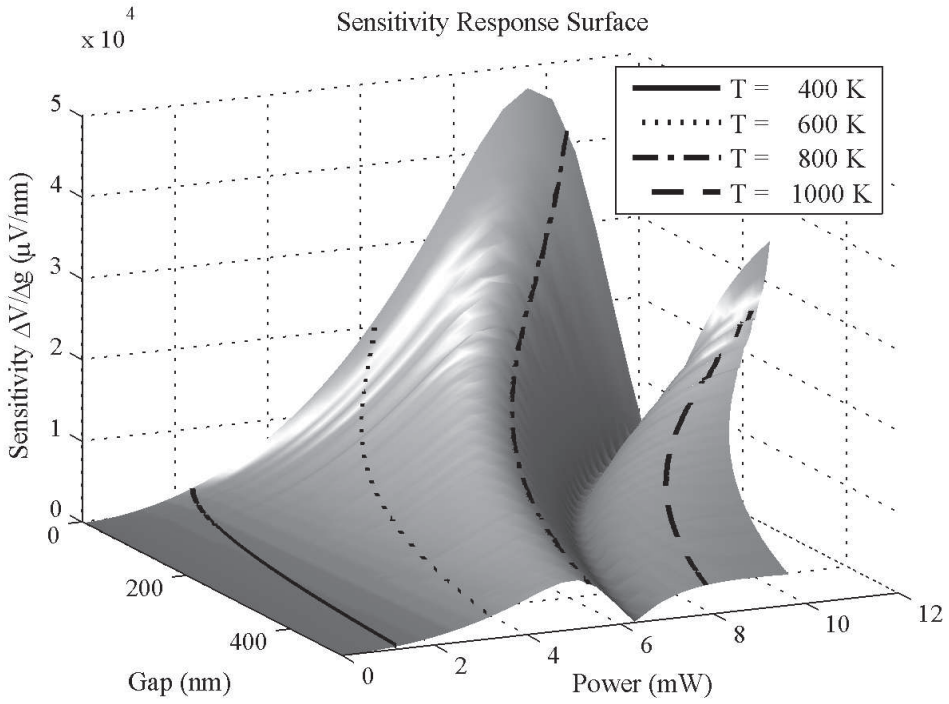

Figure 5-7: Sensitivity response surface and constant temperature curves for design 2.

are associated with similar features in both response surfaces, e.g., the ridge of maximum sensitivity at approximately 770 K and the trough at around 900 K, confirming the strong influence of the doping concentration on TSAFM sensitivity. Figure 5-7 shows that a higher maximum sensitivity is predicted for design 2 than that of the Millipede design. However, this is offset by increased power consumption. Again, the goal of design 2 was to explore the effect of quadrupling the surface area of the heater while preserving the room-temperature electrical and solid state thermal resistances along the length of the cantilever. Increasing the surface area increases the thermal conductance to the substrate and environment by up to a factor of four in the region near the heater. For simplicity, consider a 1D analysis of a heater region at a uniform temperature T_H in thermal equilibrium with the substrate and environment at T_L and thermally insulated from the legs. The total heat

transfer (or energy exchange) rate, q is proportional to the surface area

$$q = AK_{T_H,T_L,g}\left(T_H - T_L\right) \tag{5.13}$$

where $K_{T_H,T_L,g}$ is a proportionality term that lumps all the heat transfer terms and is a function of T_H, T_L, and g. The heat generation may be approximated as $q_{gen} \approx \mathcal{V}^2/R_T$, where $\mathcal{V}$ is the measured voltage and R_T is the temperature-dependent electrical resistance of the heater. Balancing the generation and the heat transfer ($q_{gen} = q$), solving for $\mathcal{V}$ ($\mathcal{V} = \sqrt{qR_T}$), and differentiating with respect to the gap, we obtain an expression for the sensitivity:

$$\frac{\partial \mathcal{V}}{\partial g} = \frac{\partial}{\partial g}\sqrt{AR_T K_{T_H,T_L,g}\left(T_H - T_L\right)} \tag{5.14}$$

For this analysis, assume that the heating power can be adjusted such that $\partial T/\partial g = 0$, and therefore $\partial R_T/\partial g$. Comparing the two designs, with the surface area being the only change, the change in the sensitivity will be bounded by the ratio

$$\frac{\left(\frac{\partial \mathcal{V}_1}{\partial g_1}\right)}{\left(\frac{\partial \mathcal{V}_2}{\partial g_2}\right)} = \frac{\left(\sqrt{A_1 R_T\left(T_{H,1} - T_{L,1}\right)}\frac{\partial}{\partial g_1}\sqrt{\frac{K_{T_{H,1}T_{L,1}g_1}}{g_1}}\right)}{\left(\sqrt{A_2 R_T\left(T_{H,2} - T_{L,2}\right)}\frac{\partial}{\partial g_2}\sqrt{\frac{K_{T_{H,2}T_{L,2}g_2}}{g_2}}\right)} \tag{5.15}$$

This now provides insight into the behavior of the two designs. Figures 5-8 and 5-9 plot the sensitivity vs. heating power and temperature vs. power for a number of constant gaps (10, 50, 100, 250, and 500 nm). The 2D log-log scales provide a more detailed and quantitative view of the target operational region (heating power less than 3 mW). Within this region the models predict slightly better performance from the Millipede design than the design 2 at any given power level. So, although larger heaters may provide higher maximum sensitivity, the trade-off of increased power consumption may actually reduce the sensitivity within the desired operational region. The thermal time constant may also be affected adversely. From a design standpoint, the behavior of the sensitivity is dominated by the temperature-dependent resistivity, which depends upon the doping type and concentration used in the cantilever legs and heater. Further research could explore this parameter in conjunction with geometries that may alter the electrical resistance.

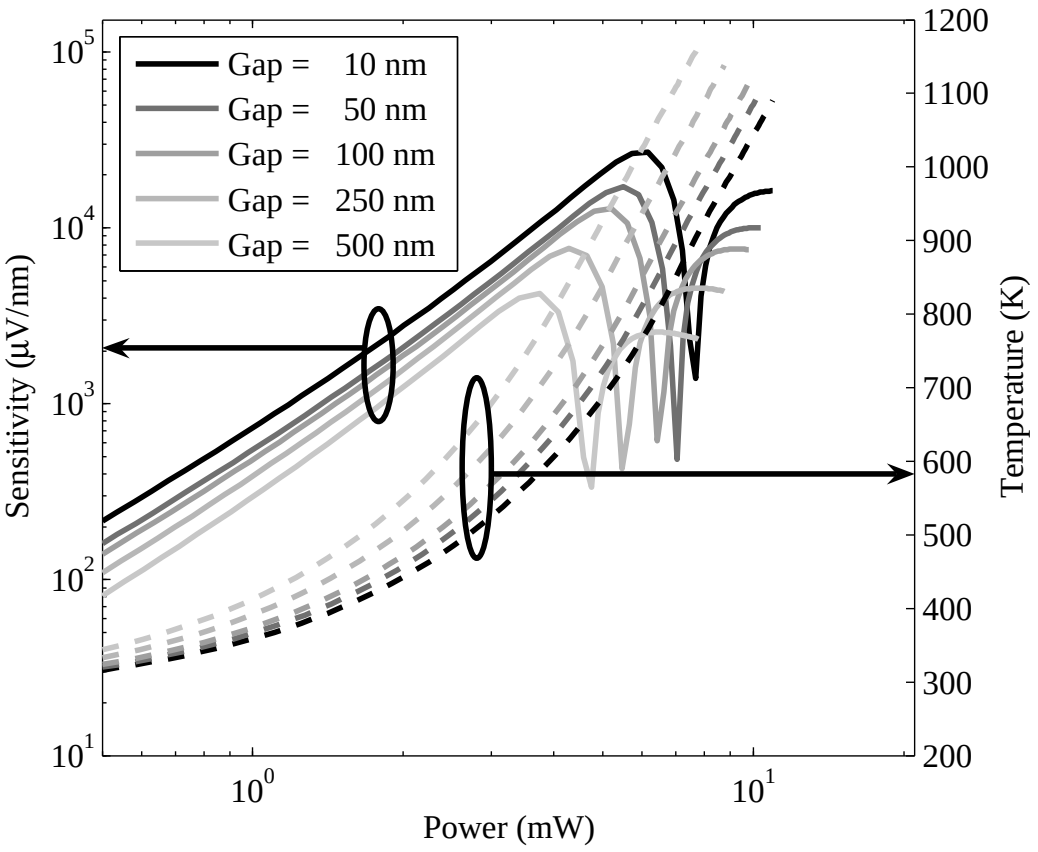

Figure 5-8: Plot of sensitivity and maximum temperature for selected air gap distances over a range of cantilever heating powers for the Millipede design.

5.1.6 Summary and Conclusion of Preliminary Model

From this model, it becomes clear that the subcontinuum heat transfer can have a profound impact on the sensitivity and operating conditions of the TSAFM and must be considered in modeling and design. The one-dimensional subcontinuum models, DSMC and macromodel, are in good agreement from free molecular to continuum limits, allowing the simpler (and far more efficient) macromodel to be used in the analysis. Although this model provides insight into these effects, 2D (or even 3D) models are needed to rigorously account for fringing regions neglected in this study. Furthermore, this simplified model does not account for mechanical phenomena that may manifest in the operation of the TSAFM

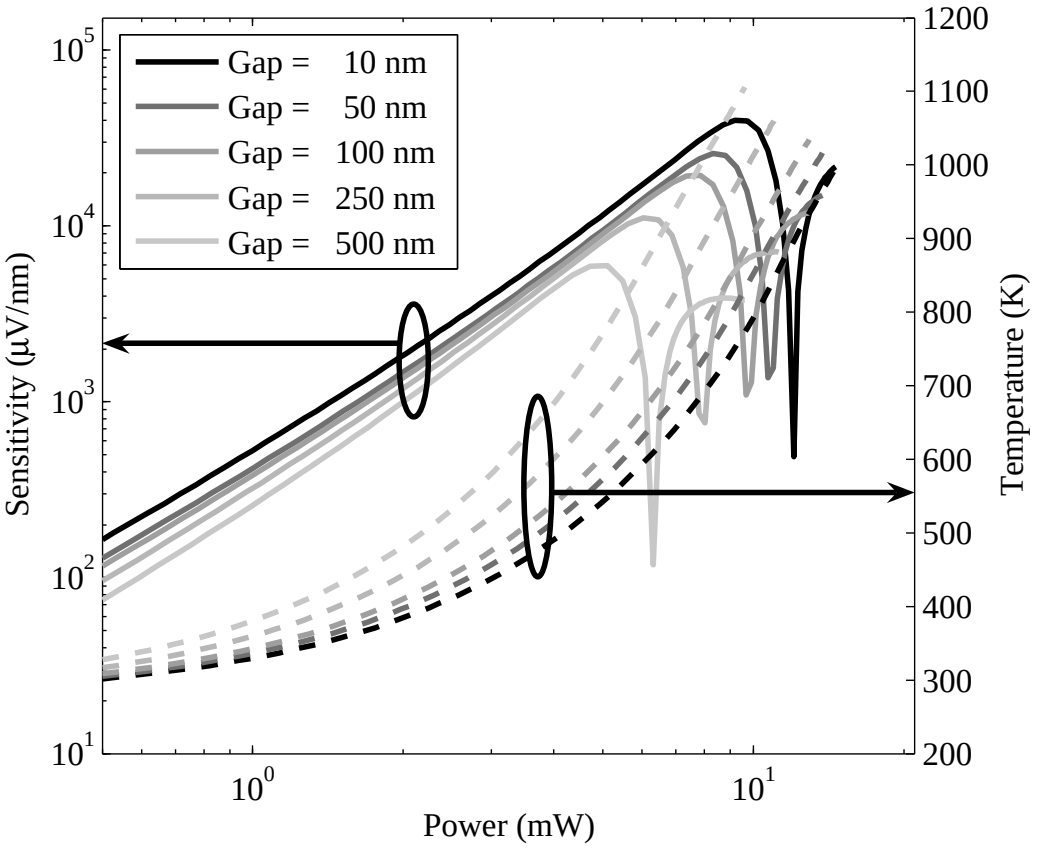

Figure 5-9: Plot of sensitivity and maximum temperature for selected air gap distances over a range of cantilever heating powers for design 2.

and similar systems. The coupled OSIP-DSMC-BEM model presented in the next sections will seek to do this.

5.2 Multiscale Modeling of a TSAFM Cantilever

Although simplified to function within the FDM framework, the model described in the preceding section did include many of the factors affecting TSAFM operation such as: Joule heating and non-uniform temperature distribution along the length of the cantilever. The balance of this chapter presents the development of a coupling scheme for the OSIP-DSMC and BEM models and its application to the multiscale modeling of the TSAFM.

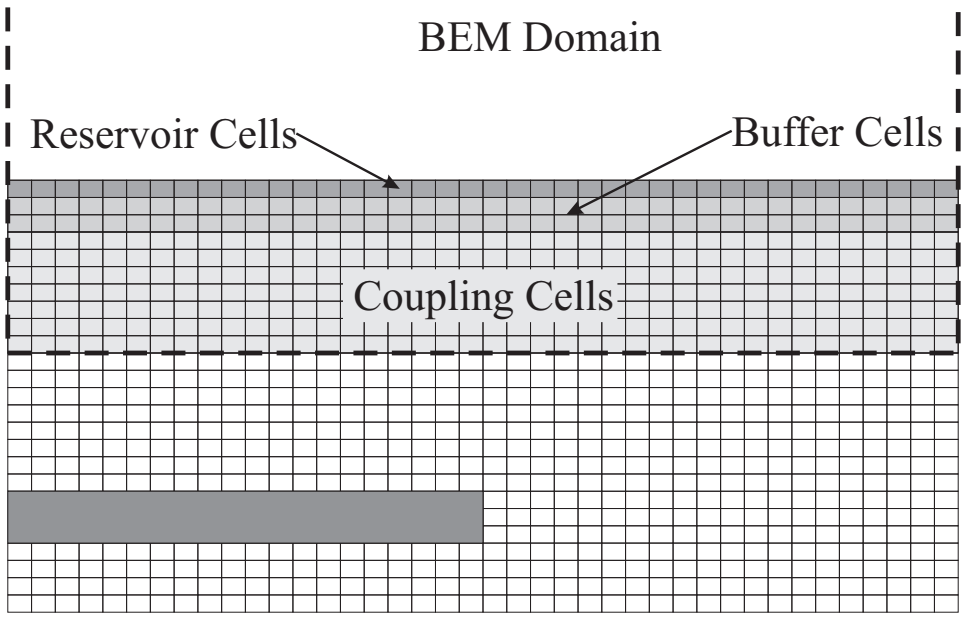

Figure 5-10: Coupling Scheme for multiscale modeling of a TSAFM cantilever

This model will include many of the effects that are neglected in the FDM model, but will not be as exhaustive with regards to characterization of system operation or sensitivity.

The method developed here is may be applied to many thermally driven systems, but the specific analysis geometry will be described at this point and referred in the course of the development. The computational domain consists of a 2D cross of the TSAFM cantilever, surrounding gas, and substrate as shown in Figure 5-11. The cantilever will be treated as if part of a close packed array (with 10 μm spacing) to allow doubly symmetric boundary conditions in the *x*-direction. The substrate will be maintained at 273 K and the analysis domain is treated as an open system with an ambient pressure of 1-atm. and a reference temperature of 273 K at some distant point. The dimensions of the TSAFM cantilever are 10 μm wide and 500 nm thick with a scan height (gap) of 500 nm and will be maintained at 573 K.

5.3 Coupling Scheme

The OSIP-DSMC and BEM are efficient numerical techniques for modeling at the appropriate length scales. This efficiency is relative, however, as the OSIP-DSMC requires a computational effort many orders of magnitude greater than does the BEM. As such, it should ideally be used as sparingly as possible, while still providing the desired accuracy. The proposed method for coupling these, and thus reducing the expense associated with the subcontinuum modeling, is the Alternating Schwarz coupling. As previously discussed, this method requires an overlapping boundary, as shown in Figure 5-10. The size and location of this region must be determined based on both computational expense and the appropriateness of the different models to various locations within the flow. Furthermore, particles must be allowed escape and new particles generated at the open boundary at the top of the domain. The consensus in the literature is that the Chapman-Enskog distribution (seeSection 2.2.2) should be used for the generation of particles at a coupled boundary, rather than the simpler Maxwellian [17, 45, 111, 112]. As this method will be used in this thesis, and plays a rôle in determining the coupling region, the following brief description of the acceptance-rejection scheme, as proposed by Garcia [37], is included.

1. Given τ_{ij} and q_i, find $B \equiv \max\left(\|\tau^\star_{ij}\|, \|q^\star_i\|\right)$, where $t^\star_{ij}$ and $q^\star_i$ are the dimensionless viscous shear tensor and heat flux vector, respectively.

$$q^\star_i = -\frac{\kappa}{P}\left(\frac{2m}{kT}\right)^{1/2}\frac{\mathrm{d}T}{\mathrm{d}x_i} \tag{5.16}$$

$$\tau^\star_{ij} = \frac{\mu}{P}\left(\frac{\partial \boldsymbol{v}_i}{\partial \boldsymbol{x}_j} + \frac{\partial \boldsymbol{v}_j}{\partial \boldsymbol{x}_i} - \frac{2}{3}\frac{\partial \boldsymbol{v}_k}{\partial \boldsymbol{x}_k}\right) \tag{5.17}$$

2. Set amplitude parameter $A = 1 + 30B$.

3. Draw $\boldsymbol{C}_{try}$ from the Maxwell-Boltzmann Distribution $f_0(\boldsymbol{C})$, *i.e.* $C_{try,i} = \mathcal{R}_n/\sqrt{2}$, where $\mathcal{R}_n$ is a normally distributed random variable with mean zero and unity standard deviation.

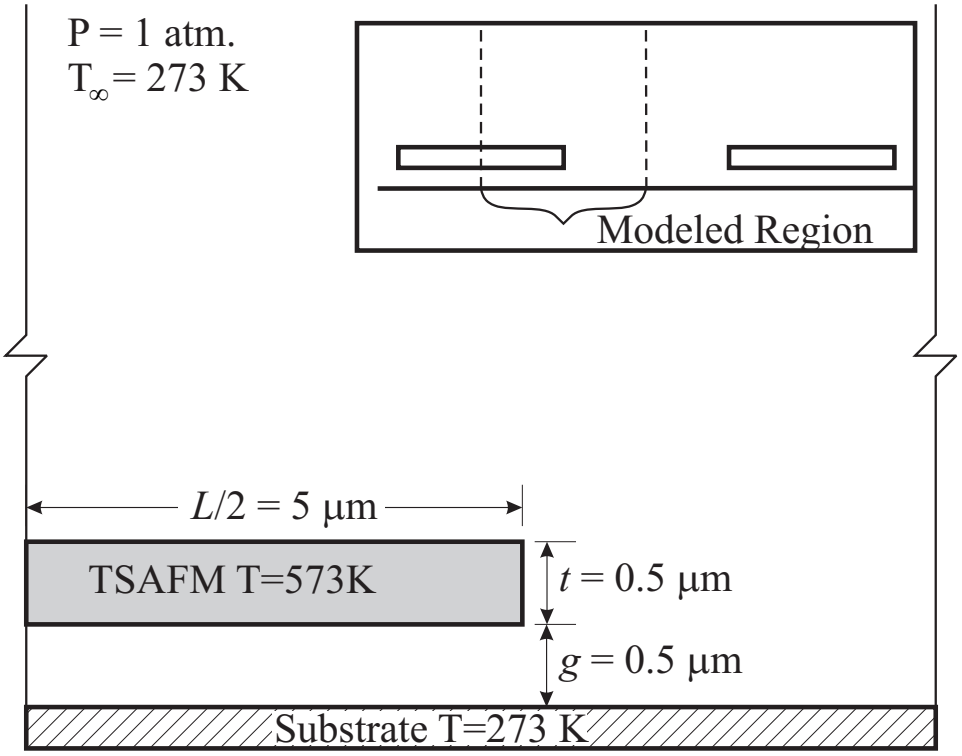

Figure 5-11: 2D TSAFM analysis domain

4. Accept $\boldsymbol{C}_{try}$ if $A\mathcal{R}_u \leq \Gamma\left(\boldsymbol{C}_{try}\right)$, where $\mathcal{R}_u$ is a uniform variate in [0, 1) and

$$\begin{aligned}\Gamma(\boldsymbol{C}) = 1 &+ \left(q_x C_x + q_y C_y + q_z C_z\right)\left(\frac{2}{5}C^2 - 1\right) \\ &-2\left(\tau_{xy} C_x C_y + \tau_{C_x C_z} + \tau_{yz} C_y C_z\right) \\ &-\tau_{xx}\left(C_x^2 - C_z^2\right) - \tau_{yy}\left(C_y^2 - C_z^2\right)\end{aligned} \tag{5.18}$$

   else go to step 3.

5. Generated particle velocity is $\boldsymbol{c} = (2k_B T/m)^{1/2}\,\boldsymbol{C}_{try} + \boldsymbol{v}$, where $\boldsymbol{v}$ is the stream velocity.

Particles will be generated in the reservoir cells (see Figure 5-10) and the number of particles generated will be determined from the current density of that region of the analysis domain. For the problem at hand, it may be safely assumed (and later shown) that the heat flux is the dominant factor in generating particles.

The breakdown of the Chapman-Enskog distribution may be as quantified by the breakdown parameter B which has just defined in terms of the dimensionless heat flux and shear stress. It is recommended that for the Chapman-Enskog distribution to be valid that $B < 0.1$. Thus for a thermally driven system, the degree of breakdown may be expressed solely in terms of the dimensionless heat flux:

$$B = |\boldsymbol{q}_i^\star| = \left| \frac{\boldsymbol{q}_i}{P} \left(\frac{2m}{kT} \right)^{1/2} \right| \tag{5.19}$$

and the coupling should be performed in a region which satisfies this criteria with respect to the breakdown parameter contours as shown in Figure 5-12(a). Figure 5-12(b) presents the temperature contours from the continuum BEM simulation of the TSAFM geometry and Figure 5-13 plots the breakdown parameter for this same simulation (for a region of space 10 μm × 5 μm) and a proposed coupling region removed from regions where the breakdown parameter is high. A further limitation of the coupling may come from the assumption that the flow is stationary, as required by the BEM for diffusive rather than advective heat transfer

From preliminary simulations, it appears that the region shown here is reasonable for coupling. This region begins 3.8 μm above the lower bound of the simulation and extends for 1 μm spanning the entire width of the analysis domain. At this time the coupling is kept simple and no attempts have been made to "fit" the coupling region to the contours of the breakdown parameter. A few additional cells are needed beyond the upper bound of the coupling region for the reservoir and buffer cells.

Now that the coupling method and region have been identified the coupled simulation will proceed as follows:

1. Perform continuum (BEM) simulation for the entire analysis domain to obtain break down parameter, initial temperature profile, and heat flux

2. Assuming a pressure equilibrium with the environment and that the density may be described by the ideal gas law $\rho = P/RT$, initialize the subcontinuum domain, setting

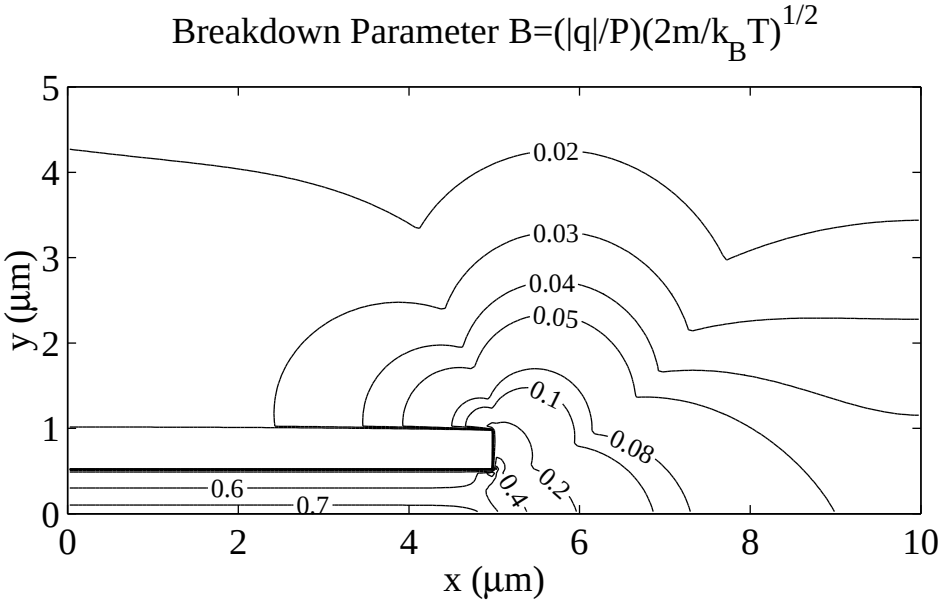

5-12(a): BEM solution for the breakdown parameter *B* for the TSAFM

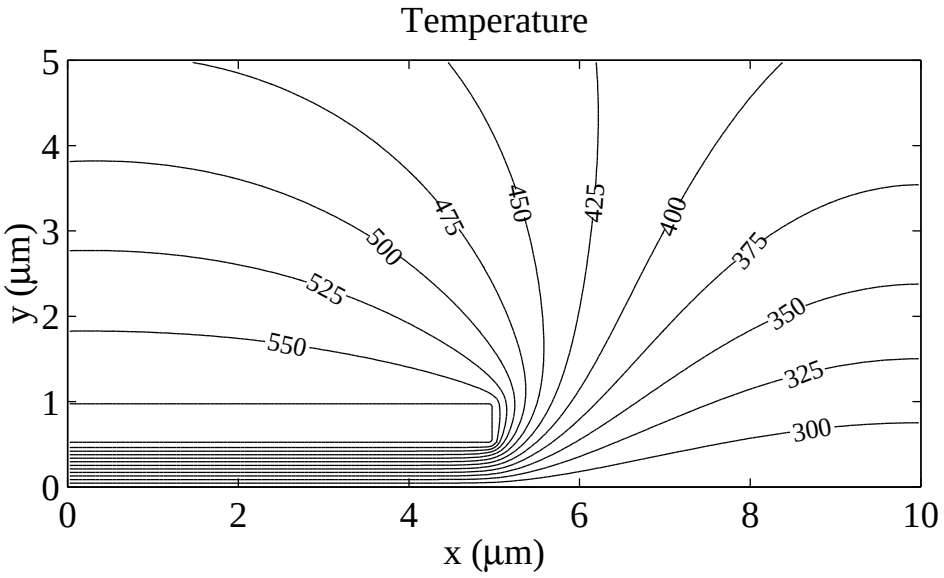

5-12(b): BEM solution for the temperature distribution of the TSAFM

Figure 5-12: Coupling preliminaries

cell temperatures, densities, and generating appropriate particles (Maxwellian may be used here)

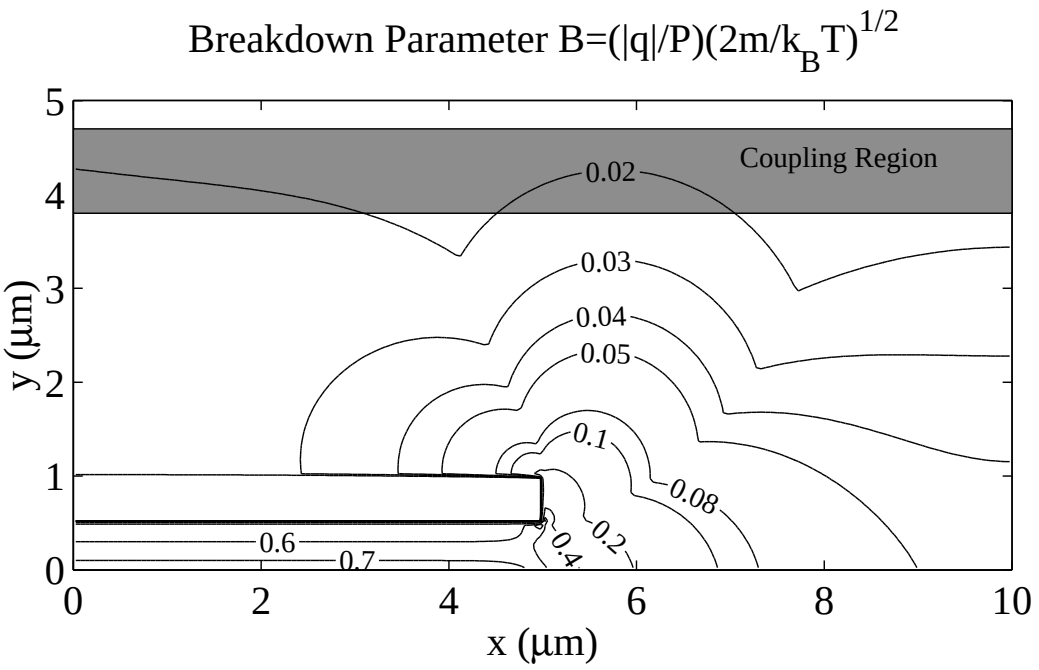

Figure 5-13: Break down parameter contours and proposed coupling region for multiscale TSAFM simulation

3. Perform N iterations of the OSIP-DSMC, using the temperature and heat flux solution from the continuum solution at the location of the reservoir cells to generate new particles. Particles leaving the subcontinuum region are removed from the simulation. At this time, $N = 1200$ timesteps which corresponds to 100 sample steps

4. Assign boundary conditions and the heat transfer coefficient for the continuum model using the current sampled temperature from OSIP-DSMC at the bottom edge of the coupled region

5. Perform the BEM simulation and post process to obtain new temperature and heat flux distributions for the reservoir cells

6. Repeat steps 3–5 until a sufficient number of time steps such that the OSIP-DSMC domain may be assumed to have reached stead state. Begin time ensemble sampling of OSIP-DSMC and continue repeating steps 3–5

7. Monitor convergence of BEM solutions and OSIP-IP, until acceptably converged

Despite the smoother results of the OSIP-DSMC, the method will still exhibit some fluctuations, so the convergence should have a reasonable tolerance.

The OSIP-DSMC domain for the TSAFM is subdivided into 10,000 computational cells (100×100) with an average of 100 particles per cell, for an initial population of 1,000,000 simulation molecules. The simulation was executed in parallel on an dual processor ATHLON MP 1900. The total execution time was approximately 70 hours and required over 700 MB of memory. Sampling of thte DSMC and OSIP-DSMC quantities began after 24000 time steps, corresponding to 0.14 μs of simulated time. The simulation proceeded for an additional 7900 sample steps, for a total of 118800 time steps (0.688 μs), at which time the simulation was considered converged and stopped. The runtime state has been saved allowing the simulation to be restarted at a later time if desired.

During the simulation, the convergence was monitored by 1. observing the OSIP-DSMC velocity field (to be compatible with the stationary flow assumption of the BEM), 2. comparing the BEM temperature distributions within the coupled domain with successive BEM solutions (every 100 OSIP-DSMC sample steps) and with the OSIP-DSMC solution, and 3. observing the convergence of the heat flux. Additionally the pressure acting on the TSAFM cantilever was monitored to identify the presence of Knudsen forces. The simulated velocity distributions for the OSIP-DSMC and DSMC are plotted in Figure 5-18. A thermally driven recirculatory flow can be observed near the edge of the beam (see Figure 5-19 for a detailed view) with a maximum velocity of 1.12 m/s. The maximum velocity within the coupling region is is 0.2173 m/s with an average magnitude of 0.1289 m/s. Although not stationary, the advective heat transfer will be small in comparison to the total heat transfer.

Figure 5-14 present the convergence of the BEM solutions. This compares the average and the maximum magnitude of the difference between the temperature field between successive BEM simulations. As can be seen, these converge very quickly after sampling

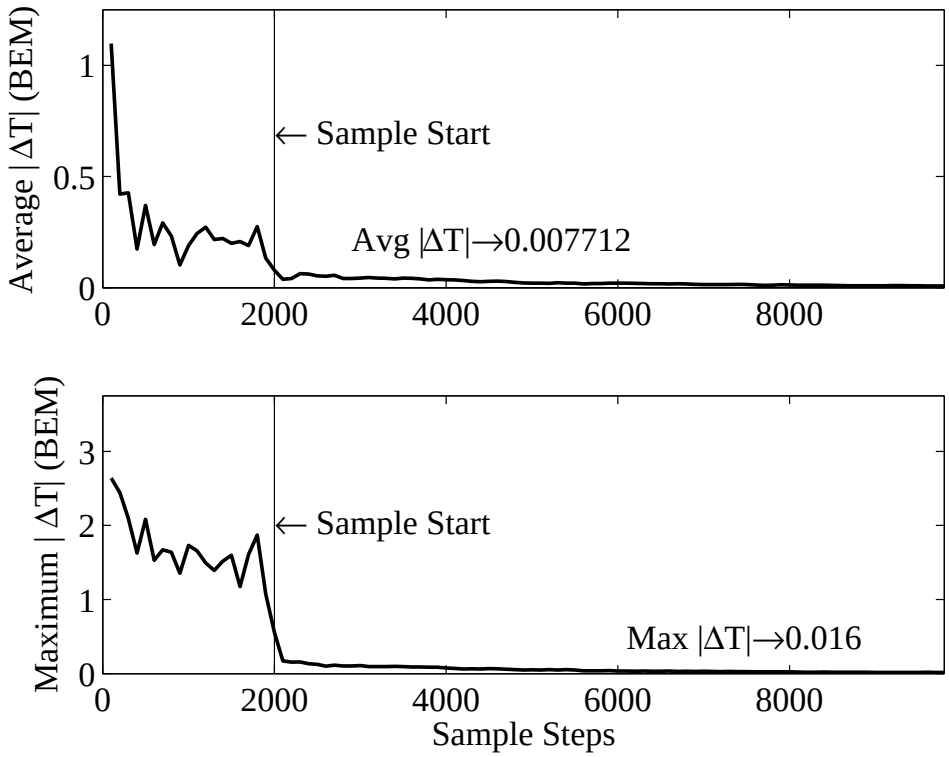

Figure 5-14: Convergence of BEM Temperature Solutions

has begun. Prior to the start of sampling, the boundary conditions applied to the BEM will fluctuate with the variations in the OSIP-DSMC, whereas after sampling has begun these quickly settle down.

The convergence of the temperature distribution within the coupling region, comparing the BEM and the OSIP-DSMC temperatures, is perhaps the key measure of convergence. The the compatibility of these solutions guarantees that both the models have reached the same solution within the overlap. Figure 5-15 the "Average $|\Delta T|$," or the average of the absolute value of the error between the two solutions over the 2000 cells in the coupling region, as well as the minimum and maximum observed errors at each time step. Again there are fluctuations prior to sampling, but this settles quickly, to a roughly steady average error of 1 K. Compared to the magnitude of the temperatures within this region, these differences are quite small (less than 1% error). Future simulations should be careful to

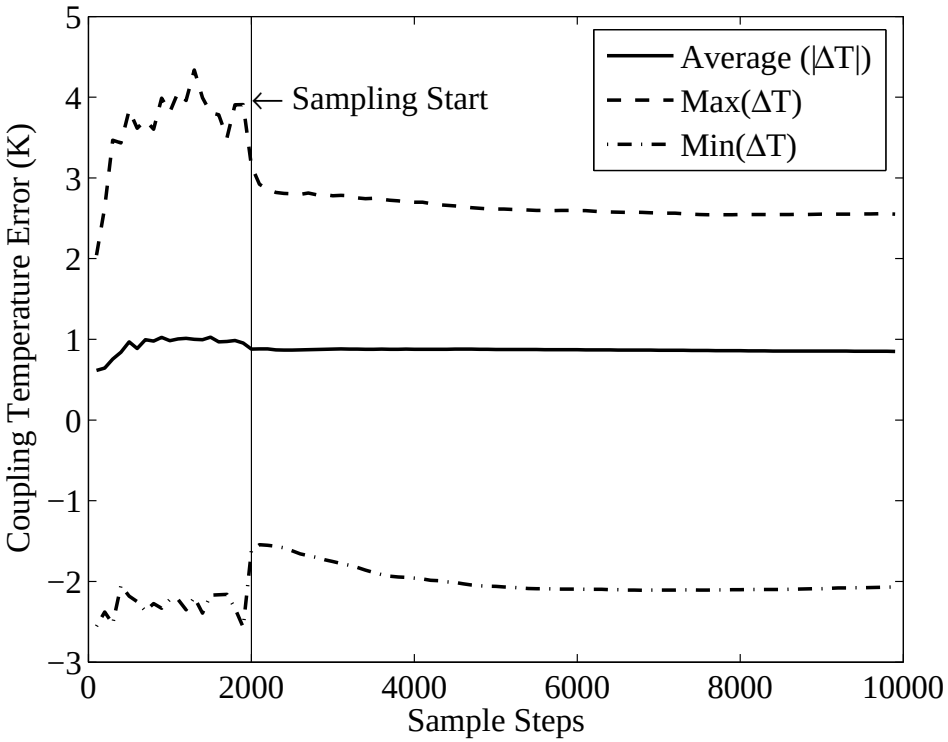

Figure 5-15: Convergence of Temperature Coupling Error

observe the behavior of the BEM as a macroscale model, as some of these discrepancies may be due to the assumptions of a stationary flow (purely diffusive heat transfer) and a constant heat transfer coefficient. Throughout the simulation the temperature distribution has evolved and the coupling scheme has resulted in consistently good agreement between the two models. The change in the temperature distribution is most clear in the comparison of the initial (continuum) solution, with the OSIP-DSMC temperature distribution at the final iteration as presented in Figures 5-16(a) and 5-16(b).

Figure 5-17 plots the convergence of the heat flux and Knudsen force. The heat flux is of immediate interest to the performance of the TSAFM, as well as a test for convergence. After the start of sampling the heat flux converges very quickly to nearly constant values. This rapid convergence would seem to indicate that shorter simulations could be used if the heat flux were the primary interest—as in a sensitivity analysis. The total heat flux per

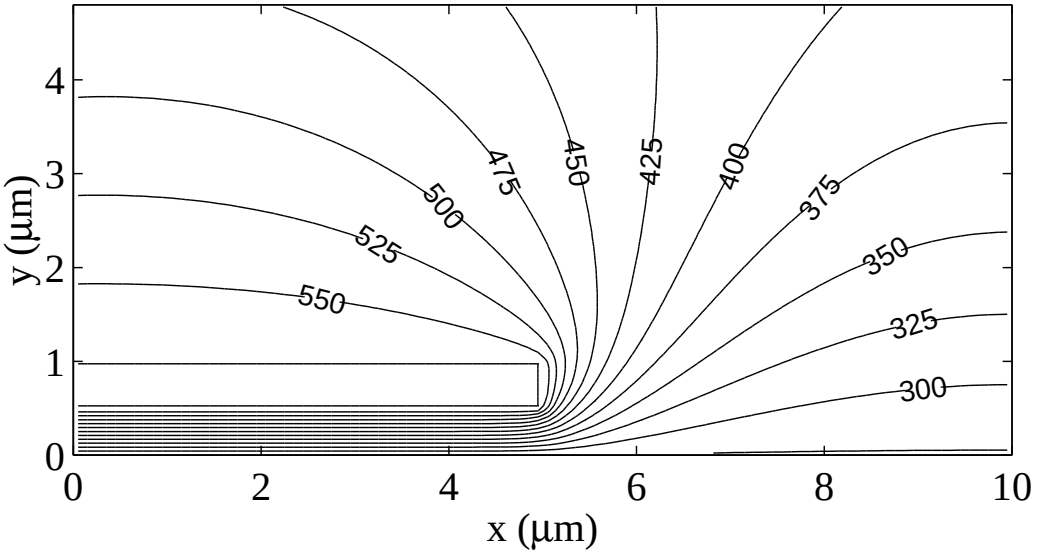

5-16(a): Initial

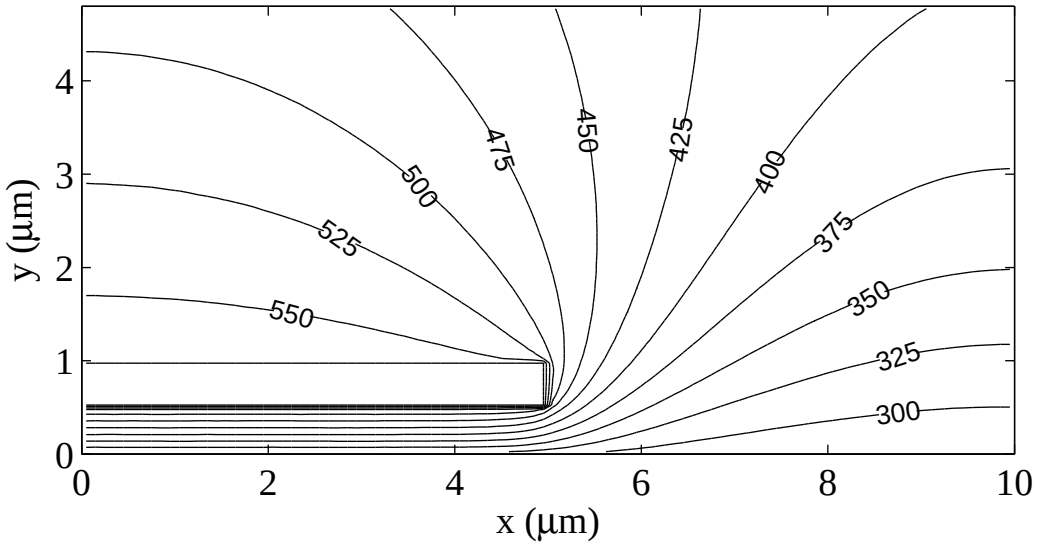

5-16(b): Sample Step 9900

Figure 5-16: Comparison of the initial and final temperature distributions for the coupled TSAFM simulation

unit length of the beam predicted by the OSIP-DSMC model is 84.46 W/m, as shown in Table 5-2. This is comparable to the DSMC flux prediction, although additional samples would be needed to have greater confidence in the DSMC value. The third column presents the continuum solution from the BEM solver for the current geometry (this uses the heat

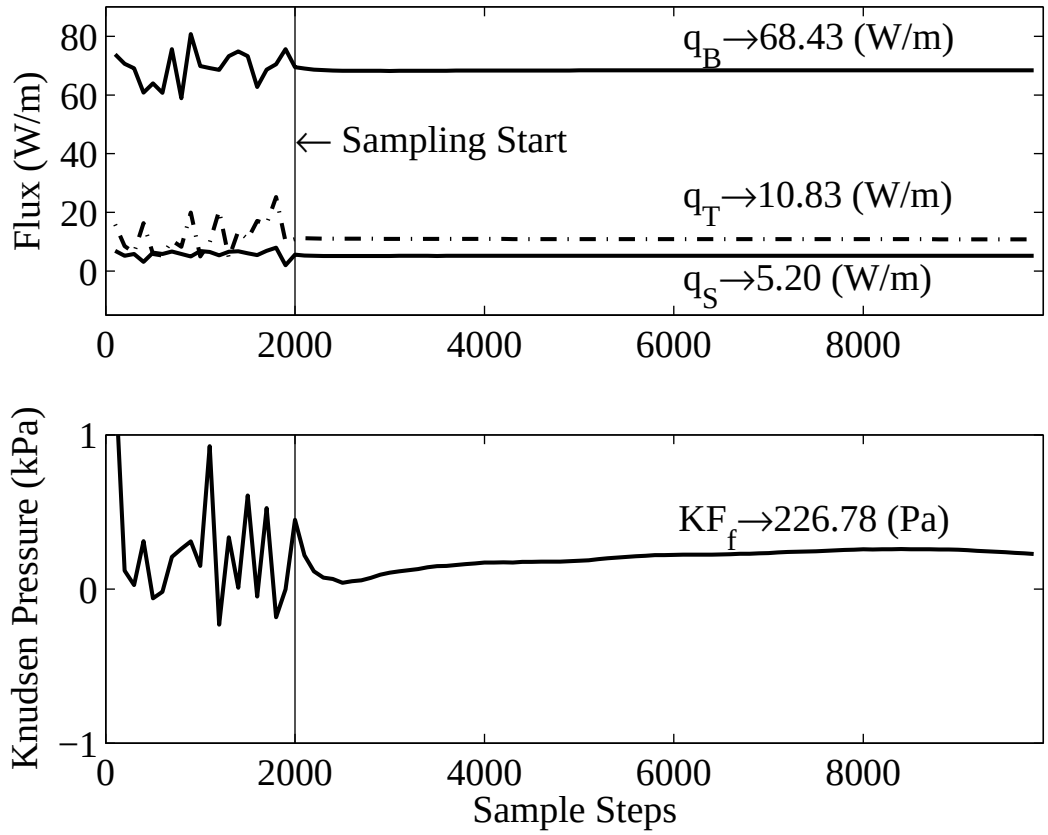

Figure 5-17: Convergence of Flux and Knudsen Force

transfer coefficient, $\bar{k}$, defined in Eq. (5.4)). The method used to develop the macromodel presented in Section 5.1.3.2 may be used to modify this solution by removing the contribution from the 1D continuum heat transfer immediately beneath the beam ($q'_c = \bar{k}w/g$) and replacing it with the subcontinuum heat transfer, $q' = k_{eff}w/g$. The results of this modification are shown in column 4. The contributions from the top and sides are comparable, but there is a significant discrepancy between the subcontinuum contributions, resulting in a 22% greater total heat flux. Reexamining the macromodel, the cause of this has been found. Whereas the continuum heat transfer coeffient depends only on the intrinsic gas properties and the temperature, the subcontinuum heat transfer coefficient also depends on density. The 1D DSMC simulations used in the development of the preliminary model treat the domain as a sealed volume, bounded by infinitely large parallel surfaces. The

Table 5-2: TSAFM Heat Flux Comparison

	Coupled OSIP-DSMC Solver	Coupled DSMC Solver	Continuum	Macro Model (273)	Macro Model (423)
Bottom (W/m)	68.43	72.92	123.15	81.73	69.34
Top (W/m)	10.83	11.67	10.25	22.16	22.16
Side (W/m)	5.20	5.58	8.51		
Total (W/m)	84.46	90.17	141.91	103.84	91.56
% Difference	—	6.62	67.23	22.37	7.90

simulations were then initialized with a density of 1.78 kg/m^3, corresponding to Argon at 1 atm. and 273 K. As the simulations progressed, the simulated gas responded to the applied thermal loads—but the average denity of the system remained the same. For the sealed 1D systems this is appropriate. The development of the macromodel remained consistent with this assumption and a constant density of 1.78 kg/m^3 was specified. Recognizing now that a 2D simulation, as well as real systems, are not sealed, it would seem appropriate to make the density a function of the ambient pressure and the probable temperature in the subcontinuum region. The density corresponding to these conditions, (1 atm. and the average temperature, 423 K) is 1.15 kg/m^3, and the resulting heat flux for the system is 91.56 W/m—a significantly better approximation. With this change, it appears that the macromodel should be able to provide rapid assessment of the heat transfer characteristics of a TSAFM cantilever with considerable accuracy.

The Knudsen force is an interesting subcontinuum effect related to thermal transpiration, and thermal creep. The Knudsen force manifests when a heated object is in close proximity (relative to the mean free path) to a cool surface. Recently a number of researches have taken an interest in the phenomenon as it can effect AFM systems, altering their operation [85, 86, 59]. Experiments done by Passian *et al*. have shown that the Knusen force, like many such effects has maximum effect in the transition regime. The current simulation models a device operating in the transition regime, and predicts that a Knudsen force,

resulting from a static pressure differential of approximately 200 Pa will be present (see Figure 5-17). The distribution of this pressure differential can be observed in Figure 5-21. The pressure distributions of the OSIP-DSMC and DSMC do not match (although both predict a Knudsen Force, but the current DSMC quantities predict a much higher value of nearly 1 kPa). The DSMC results seems to indicate the presence of a pressure gradient under the beam, such that the pressure is highest at the bottom surface of the beam and decreases closer to the underlying surface. In the authors experience, obtaining smooth results for pressure from the DSMC often requires large number of samples, but should be undertaken in the future in order to validate the OSIP-DSMC results. The effect of this Knudsen force predicted by the OSIP-DSMC would be a 2 milli-Newton/m distributed load. If we assume that the TSAFM behaves as an ideal cantilever and that the pressure differntial is uniform under the entire length of the beam, then the total displacement may be calculated as:

$$y = \frac{KFwL^4}{8EI} \tag{5.20}$$

where KF is the Knudsen force (or pressure differential), $w = 10$ µm is the width of the beam, L is the length, E is Youngs modulus, and I is the moment of inertia (for a rectangular cross section $I = wh^3/12$ where h is the beam thickness. Assuming that $E = 165$ GPa and the length $L = 150$ µm, the total deflection would be on the order of 3.5 nm—a deflection that could adversely affect the resolution of a TSAFM system. Furthermore, smaller (or perhaps larger) scan heights may induce stronger Knudsen Force effects.

The shear stress distribution (seeFigure 5-22) is again plotted as equivalent Von Mises stresses. Four features are particularly noteworthy in observing the OSIP-DSMC and DSMC shear stress results: 1. both models have a similar distribution of shear stresses near the edge of the beam, which result from the thermally driven flow; 2. the magnitude of these shear stresses is considerably different, probably indicating the inadequate number of samples for the DSMC; 3. there are regions of elevated shear stresses adjacent to the surface of the beam in both models, but the magnitude is again higher in the DSMC simulation

results; and 4. most of the domain, particularly the coupling region, is characterized by low shear stresses, supporting the assumption that the breakdown parameter for this problem should be the dimensionless heat flux.

5.4 Summary

Two models for simulating the behavior of the TSAFM have been developed in this chapter: a simplified model capable of rapid assessments for evaluating overall system performance and sensitivity, and a detailed multiscale 2D simulation coupling the BEM and the OSIP-DSMC. After recognizing and correcting the faulty assumption in the treatment of the density in the 1D model, the two models agree quite well in terms of total heat transfer from the TSAFM to the surface and environment. The detailed model provides great insight to the effects of thermal stresses on the gas flow, inducing a thermal driven flow near the edge of the beam and a pressure differential between the gap beneath the beam and the exterior, resulting in a net pressure difference of approximately 200 Pa. This give rise to what is known as the Knudsen force effect, and calculations here have shown that they are substantial enough to adversely affect TSAFM operation. The next chapter will present additional exploration of the Knudsen force as well other novel thermally driven flows.

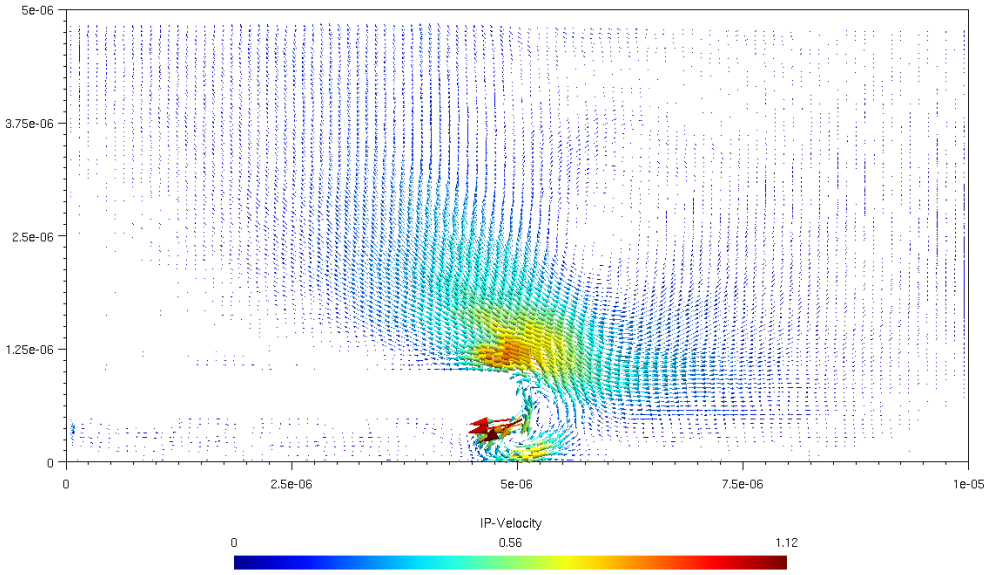

5-18(a): OSIP-DSMC

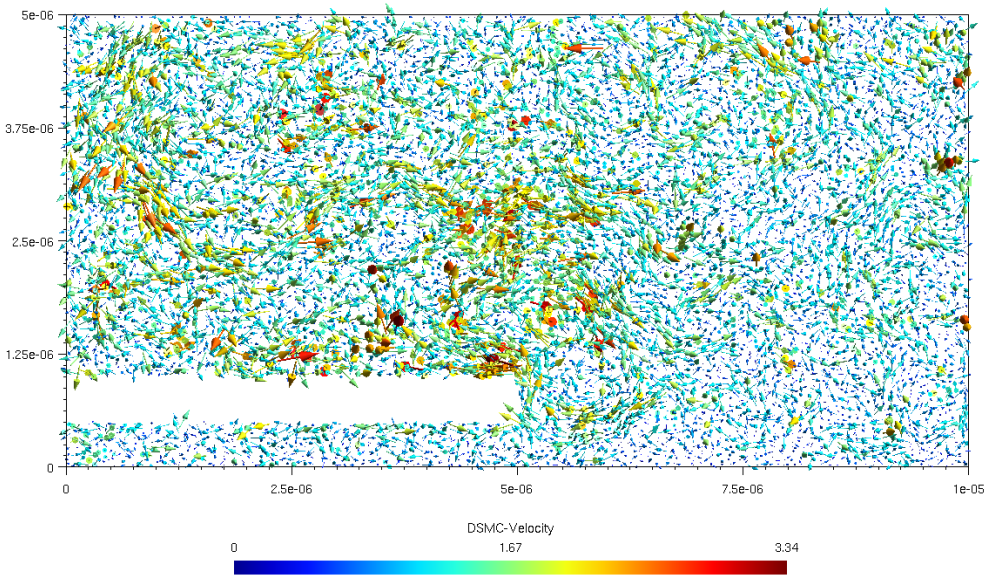

5-18(b): DSMC

Figure 5-18: TSAFM Velocity Distribution

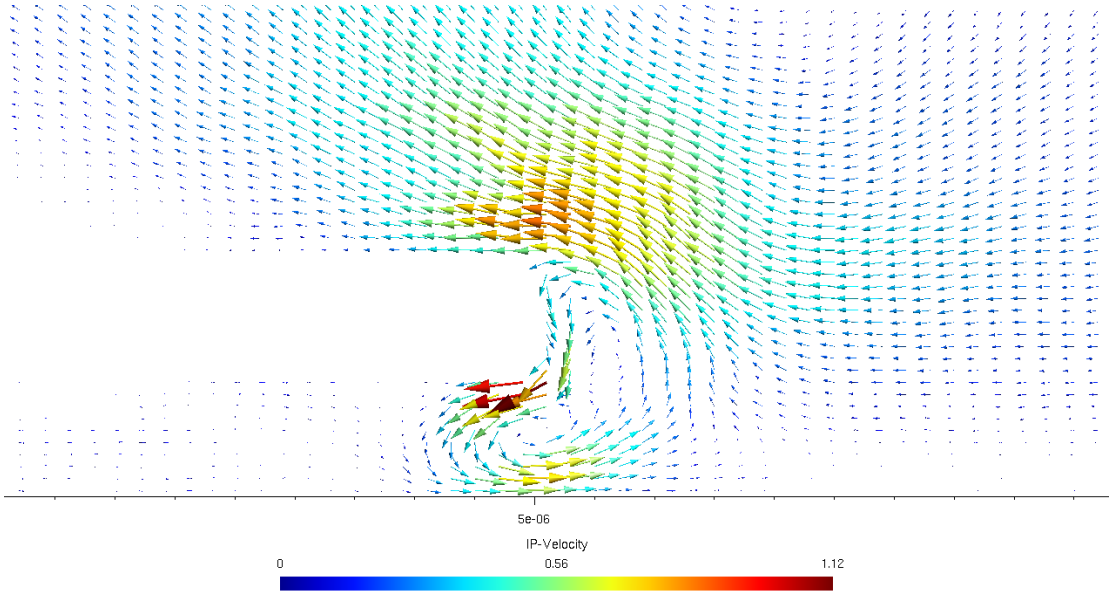

Figure 5-19: Detail of OSIP-DSMC Velocity Distribution near beam edge

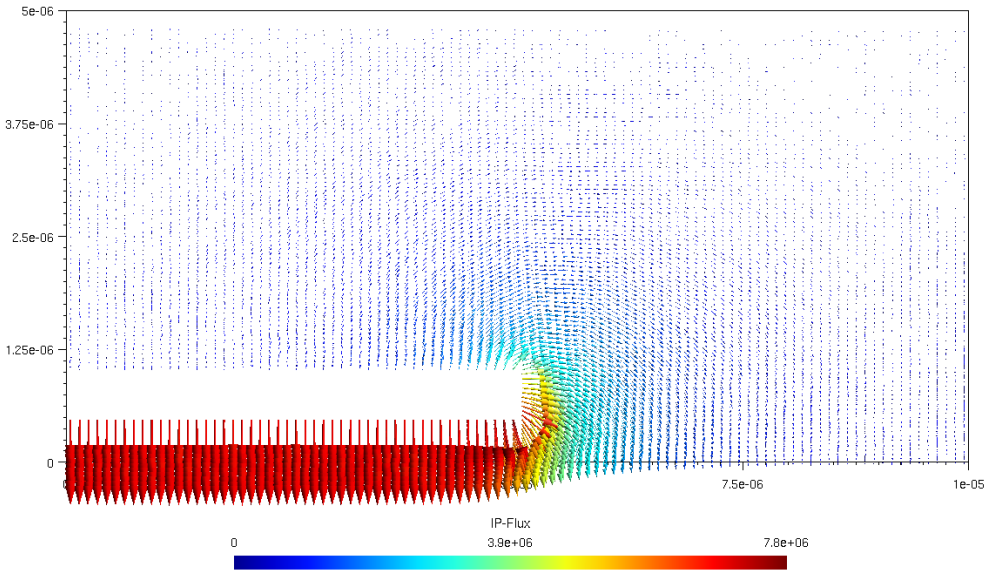

5-20(a): OSIP-DSMC

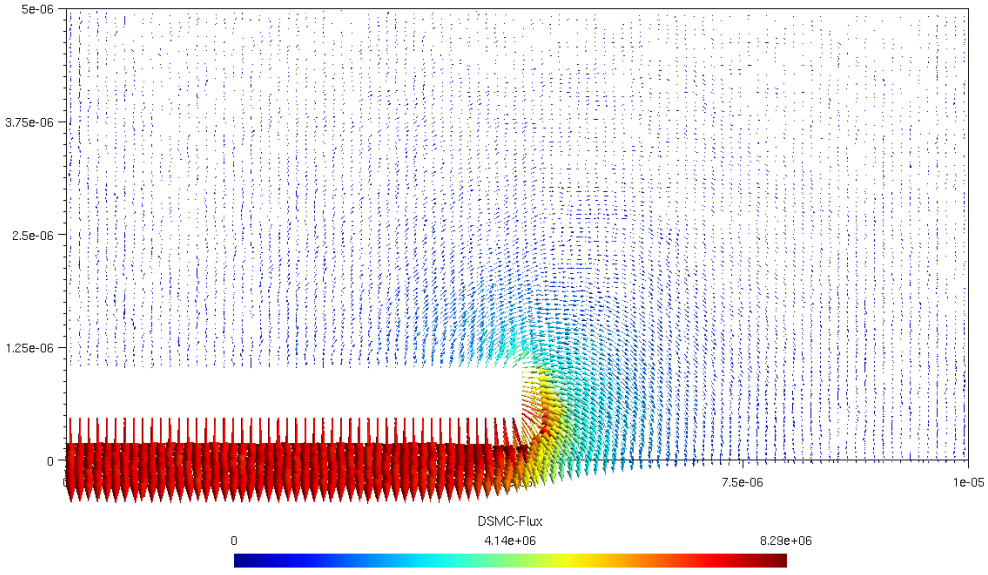

5-20(b): DSMC

Figure 5-20: TSAFM Heat Flux

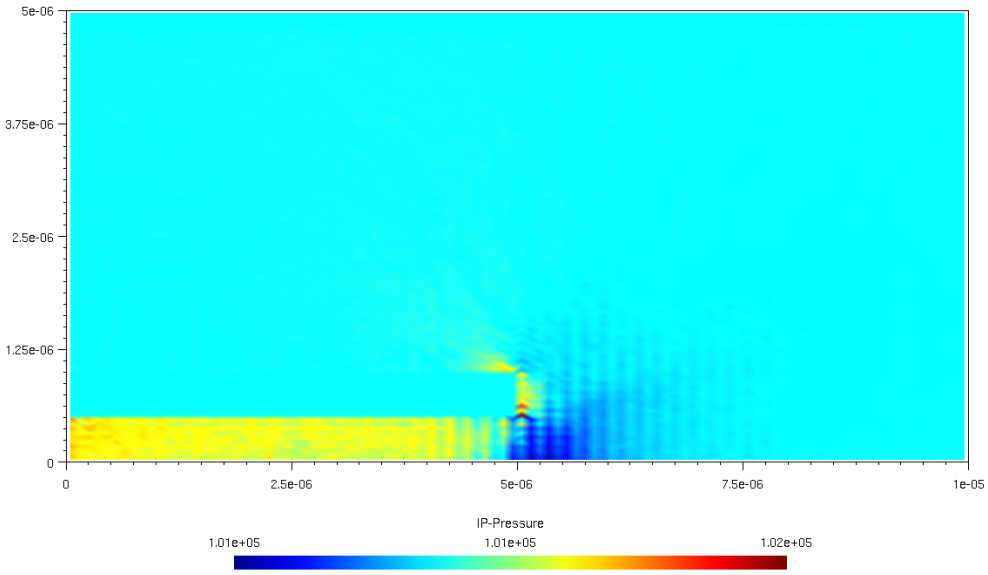

5-21(a): OSIP-DSMC

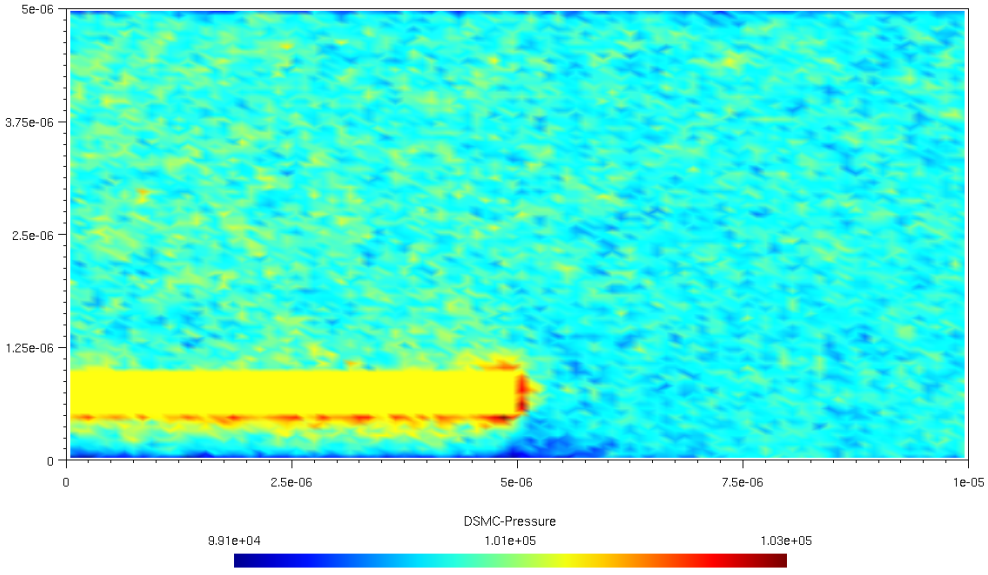

5-21(b): DSMC

Figure 5-21: TSAFM Pressure Distribution

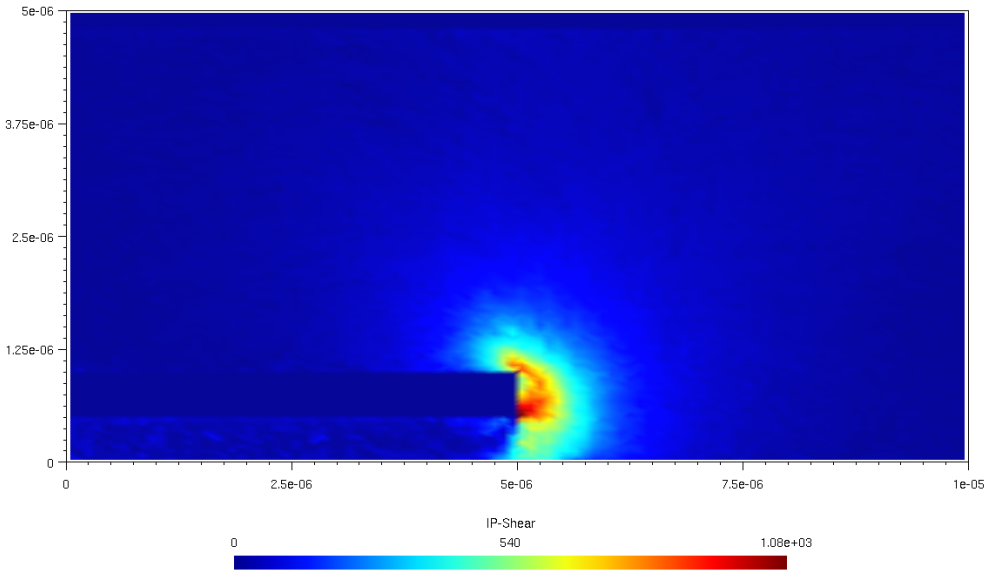

5-22(a): OSIP-DSMC

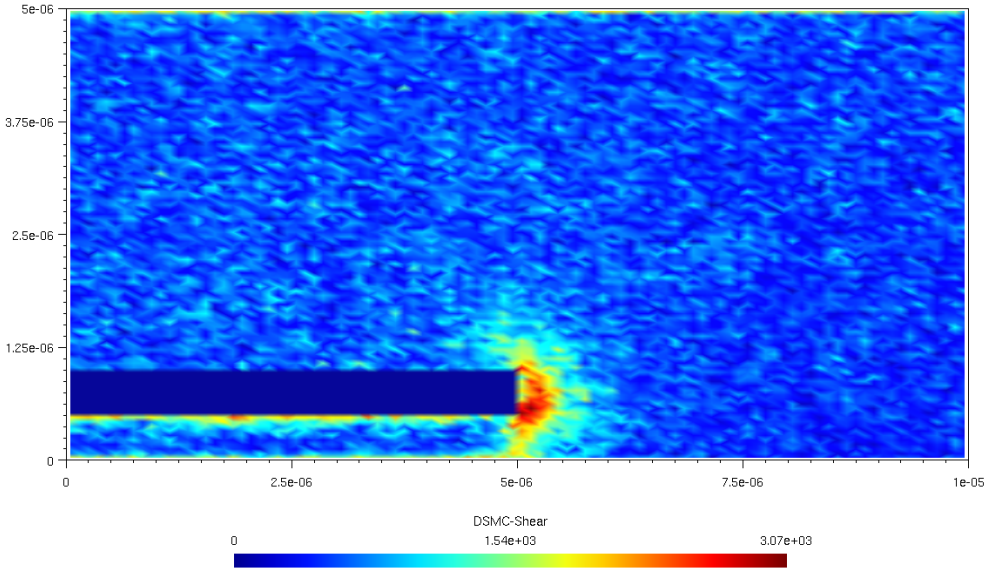

5-22(b): DSMC

Figure 5-22: TSAFM Shear Distribution

CHAPTER VI

ADDITIONAL THERMALLY DRIVEN FLOWS

The Octant Splitting Information DSMC is an exciting tool for exploring thermally driven flows. Many flows that are of interest for theoretical and practical reasons have been difficult to model. This chapter will briefly introduce a number of additional thermally driven flows that may be studied with the OSIP-DSMC.

6.1 Knudsen Force

The following is a preliminary effort to study the Knudsen force without requiring large coupled simulations, as used in the previous chapter. An improved understanding of the mechanism and the magnitude of this phenomenon as a function of beam geometry, temperature, and pressure would be of use to researchers in the fields of MEMS and NEMS as well as the various scanning probe microscopy techniques. In order to simplify the analysis, a sealed rectangular region will be used, in this case 5 μm × 2.0 μm. The left hand side will be treated as symmetric, with 0.25 μm thick beam extending 3 μm into the domain from this side. In this simulation the beam is suspended 250 nm above the lower bound, leaving 1.5 μm above and 2.0 μm on the side. Although is is possible that Knudsen force effects develop on the top and bottom of the beam, this simplified model may still provide considerable insight.

The boundaries are maintained at 273 K and a small temperature difference of 30 K is applied to the beam. Four different initial pressures are used: 0.25, 0.5, 1, and 2 atm. each initialized using the continuum temperature distribution and the ideal gas law. Figure 6-1 presents the IP pressure and velocity distributions for the 1 atm simulation. The pressure difference is clearly discernable, with region immediately beneath the beam at the highest

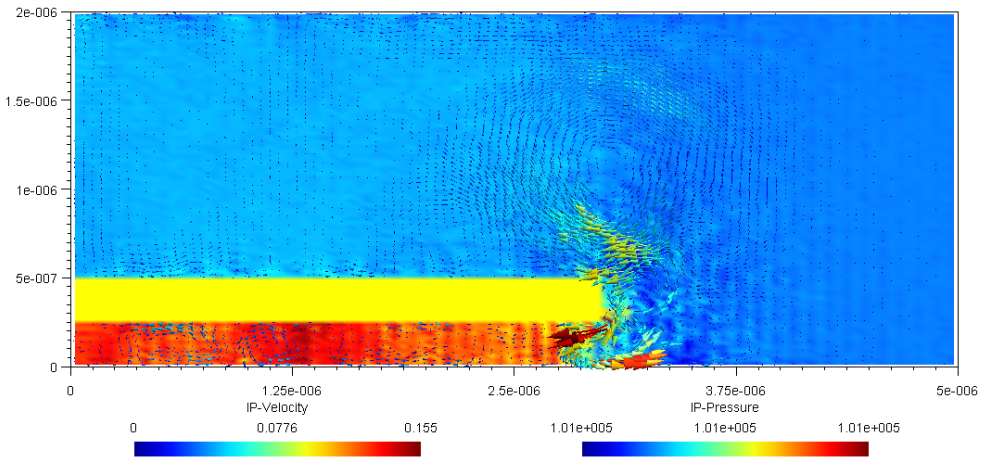

Figure 6-1: Knudsen force simulation pressure and velocity distributions

pressure. The lowest pressure occurs just past the end of the beam near the lower bound of the domain. The pressure above the beam is higher than that in the remaining space to the right of the beam, indicating the upper region is also experiencing a Knudsen force affect. The velocity distribution again predicts an impinging flow on the edge of the beam that recirculates above and below the beam, with the highest velocities immediately below the end of the beam.

Table 6-1 presents the results from these four simulations. It is surprising to find that the predicted Knudsen forces are of nearly the same magnitude. The reason for this—and whether this is entirely physical—needs to be determined. However, it may be useful to compare these results to the measurements reported by Passian, *et al*. [84]. In their work a microscale cantilever beam (see Figure 6-2) is fabricated and illuminated by a laser to produce a temperature rise. The deflection of the beam may be monitored via capacitance measurements. The beam is then placed in a vacuum chamber that may be filled with different species of gas at different pressures. For comparison, their results for Argon may be extracted, as shown in Figure 6-3. These results and those of the current simulations

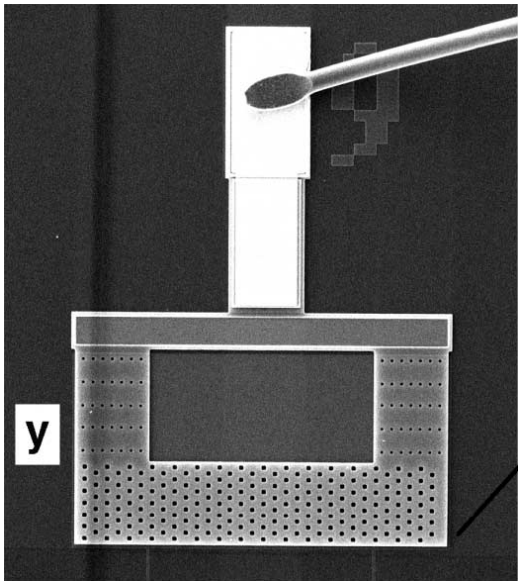

Figure 6-2: "Crookes Cantilever used in Knudsen Force study by Passian *et al*. [84]

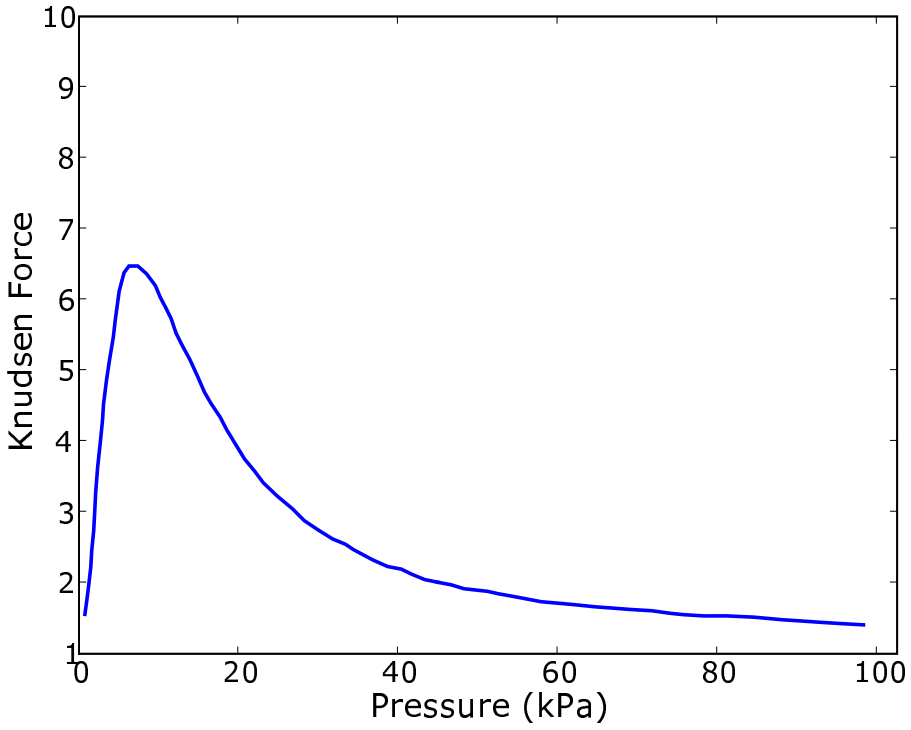

Figure 6-3: Experimental data of Knudsen force for the "Crookes" cantilever [84]

may be non-dimensionalized as the pressure ratio χ

$$\chi = \frac{P_b}{P_t} = \frac{KF + P}{P} \tag{6.1}$$

and plotted with respect to the corresponding Knudsen number at each point. Comparing these reveals that both follow a similar trend of increasing pressure ratio with increasing Knudsen number, but the current simulation predicts much higher pressure ratios. This may be due in part to the dissimilar geometries used, or may indicate unresolved issues in the simulation technique. In any case, further studies will be performed, perhaps using geometries that are compatible with such experiments.

Table 6-1: Summary of 5 μm × 2 μm Knudsen force simulations

Initial Pressure	Pressure on	Pressure	Knudsen Force
Initial Pressure	Bottom (Pa)	on Top (Pa)	(Pa)
0.25 atm	25368	25278	90.0
0.5 atm	50696	50600	96
1 atm	101361	101261	100
2 atm	202820	202712	108

As an additional observation, the velocity distribution in each of these simulations behaved much as in the TSAFM simulation, with a thermally driven current impinging on the edge of the beam. Due to the closed system a recirculatory flow develops above and below the edge of the beam in each of simulation. Future work will include additional Knudsen force simulations consisting of similar closed geometries. The parameters of beam width, gap, temperature, and initial pressure will be varied to map out the effect of the Knudsen Force

6.2 Crookes Radiometer

Perhaps the most familiar—and yet often misunderstood—effect of rarefied gas dynamics is the Crookes Radiometer. The effect was first observed by Fresnel, and then studied

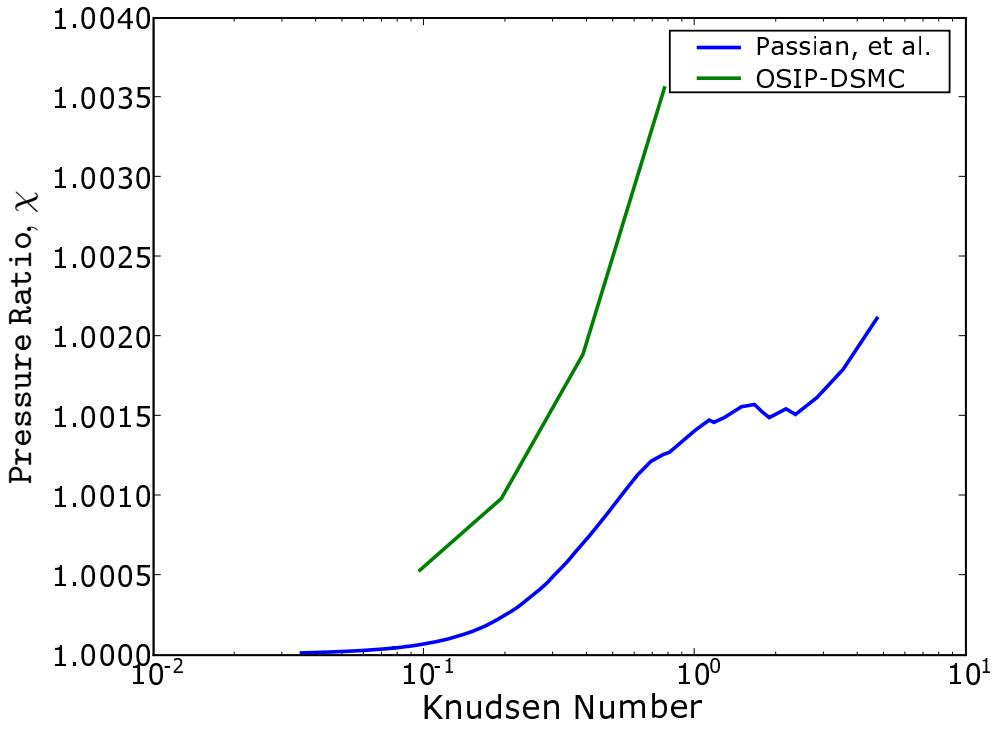

Figure 6-4: Pressure ratio comparison of with Knudsen force experiments of Passian *et al.*.

extensively by Crookes, beginning in 1873 [61]. The familiar form of a radiometer consists of a set of light-weight vanes mounted on a spindle and blackened on alternating sides. These are located inside a partially evacuated space, such that the radially arranged vanes are free to rotate and may be exposed to light. Under exposure to radiation, the vanes begin to turn with the rotation in the direction of the light colored side of the vanes. For more than 50 years the cause of this behavior was debated, involving efforts by Maxwell, Knudsen, and Einstein [61]. It turns out that although there are a number of effects that contribute to this behavior, the dominant one is the same thermal creep effect that leads to thermal transpiration and the Knudsen force. Basically, the gradient across the edges of the vane from the hot (blackened) side the cold (white) side induces a creep flow from the cold to

the hot side. As a result of the conservation of momentum, the vanes are pushed along, opposite the movement of the gas—and thus the light side precedes the dark side.

Two recent papers have each explored the radiometric effect by experiments and numerical simulations using the DSMC [62, 81]. The experiments in both studies identified the Knudsen number range from Kn = 0.1–0.3 as the optimal operating range. Both studies then included DSMC simulations of simplified radiometer geometry. In the paper by Ota, *et al*. a 300 K temperature difference is assigned to each 0.1 mm thick blade, where as Lu implements a 600 K temperature difference! These unrealistically high temperatures are needed to drive a flow of sufficient magnitude to be captured by the DSMC with a reasonable computational expense. Although no data is given on the actual temperature differences arising in the experiments, the results of both experiments are surprisingly similar, despite very different geometries. The observed rotational rates in reported by Lu ranged from 10 to 50 rads/s for the 20 mm vane system and from 20 to 70 rads/s for the 10 mm system. Ota *et al*., report rotation rates for their 1 mm vane system for Argon between 15 and 18 rps and additionally the torque for a stationary radiometer is reported.

As a first step in applying the OSIP-DSMC to the problem of the radiometer, a single microvane was modeled with a length of 0.8 μm within a sealed domain 2.04 microns by 1.6 microns and a temperature difference of 7 K (T_C = 273 K, T_H = 280 K). The pressure was initialized at 5 kPa. Figure 6-5 presents results for this simulation after 3400 samples showing the velocity and temperature distributions are superposed to accentuate the thermal creep that drives the radiometric effect (seeFigure 6-5(a)). The maximum velocity is less than 0.1 m/s, which, given the small temperature gradient is not surprising. The pressure distribution in Figure 6-5(b) and exhibits a pressure differential, albeit on the order of 4 Pa. To obtain this resolution from the DSMC would require thousands of times more samples—and months of computing time.

For a direct comparison with experimental results, a full model with four vanes, based on the geometry reported in [62], using 20 mm long vanes is simulated (see Figure 6-6).

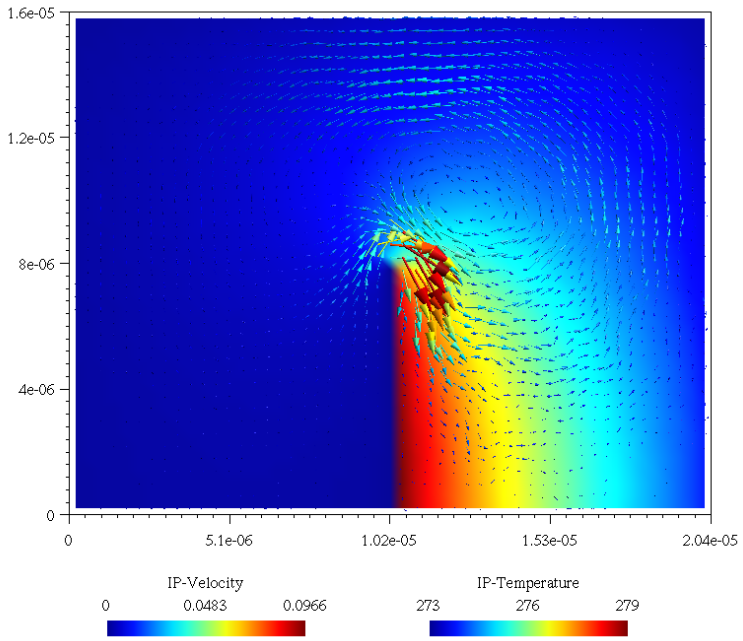

6-5(a): Temperature and Velocity

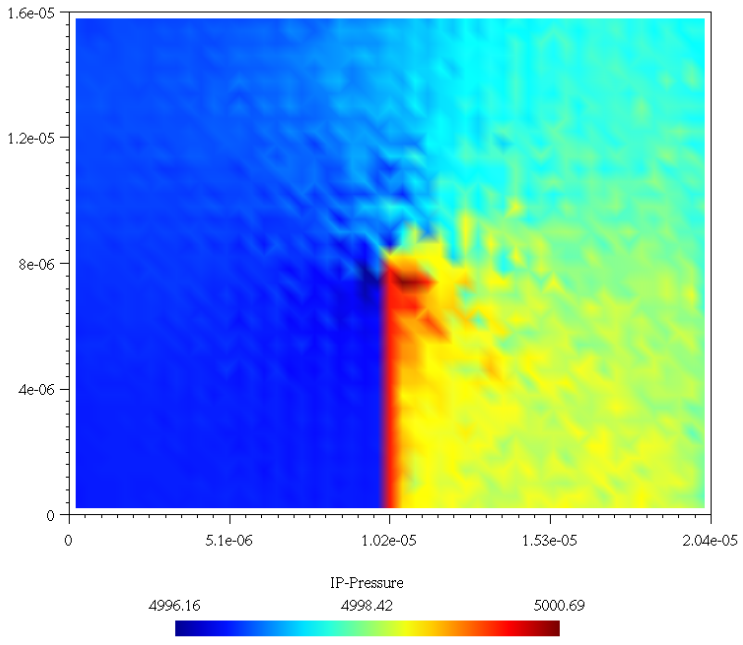

6-5(b): Pressure Distribution

Figure 6-5: Results for a single vane Crookes Radiometer

The working gas is Argon at an initial pressure of 0.2 Pa and uniform temperature of 273 K. A 7 K temperature difference is applied to the alternate faces of the radiometer. The velocity and temperature distribution for this simulation after 48000 time steps are presented in Figure 6-7(a) and the pressure distribution in Figure 6-7(b). The maximum velocity is 0.117 m/s, which if the outer edge of the vanes were moving at that speed would be a rotational rate of 0.7 rotations per second, or 4.68 rads/s. This is an order of magnitude lower than the experimental results, and requires the assumption that the vanes would move at the same speed as the maximum observed velocity. However, the true temperature difference in the experimental system is unknown. It would be very useful to instrument a radiometer vane such that the actual temperature difference could be obtained and used in future simulations.

However, allowing the simulation to continue reveals that there may be additional problems with the OSIP-DSMC. The results from the cited papers tend exhibit velocity fields that have maximum values near the extreme ends of the vanes. An addition simulation was performed using a larger 100 K temperature difference and allowed to run for 240000 time steps, accumulating 18000 samples. (Note, that the orientation of the hot and cold sides has been reverse.) At this larger temperature difference and number of samples, the DSMC flow field is recognizable and corresponds well with those reported in the cited works. The OSIP-DSMC exhibited a very different distribution, with the flow occurring principally near the axis—at the interior edge of the vanes (see Figure 6-8). The flow around the extreme edges is quite small. Furthermore the pressure difference, which was present at earlier stages in the simulation has reversed—with a lower pressure on the hot side of the vanes. It appears that, as was the case with the Split Box problem, that the radiometer has uncovered another aspect of the method that may be improved. This will be addressed in future work. One possible explanation may be that the heat flux vector may not be the ideal choice for determining the local coordinate system.

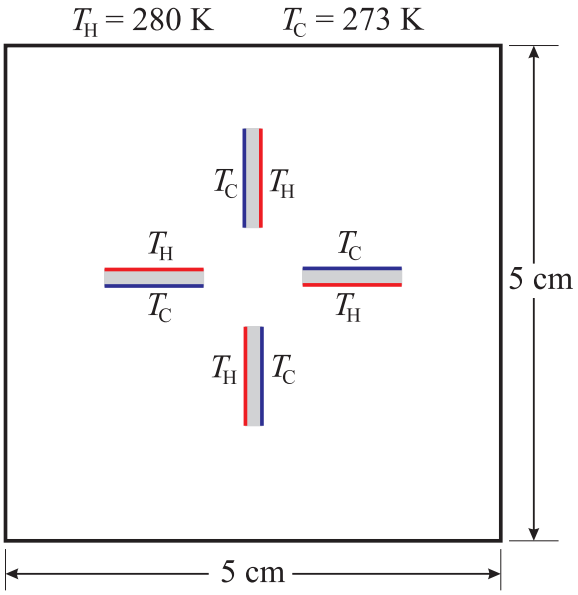

Figure 6-6: Schematic diagram of radiometer simulation domain

6.3 *Temperature Discontinuity: Thermal Cavity*

As a final exercise, consider a variation on the Split Box that consists of a closed square region. The temperature on three of the sides are equal (in this case T_c = 200 K) and the fourth has a temperature twice a great. The simulation was performed for two initial pressures: 1 atm. and 0.1 atm. The geometry is 1 µm × 1 µm with the hot wall being on the left side. Only the lower half of the system is modeled using a 40 × 20 array of cells. The velocity distributions are presented in Figure 6-9. The DSMC velocity for the 1 atm. simulation (see Figure 6-9(a)) is beginning to exhibit a flow pattern after 12600 samples, while the OSIP-DSMC has already full developed. For the case of 0.1 atm. no organized flow was apparent in the DSMC.

6.4 *Summary*

Although these were only briefly discussed at this point, these problems illustrate a variety of thermally driven flows and demonstrate the difficulties involved in using the conventional

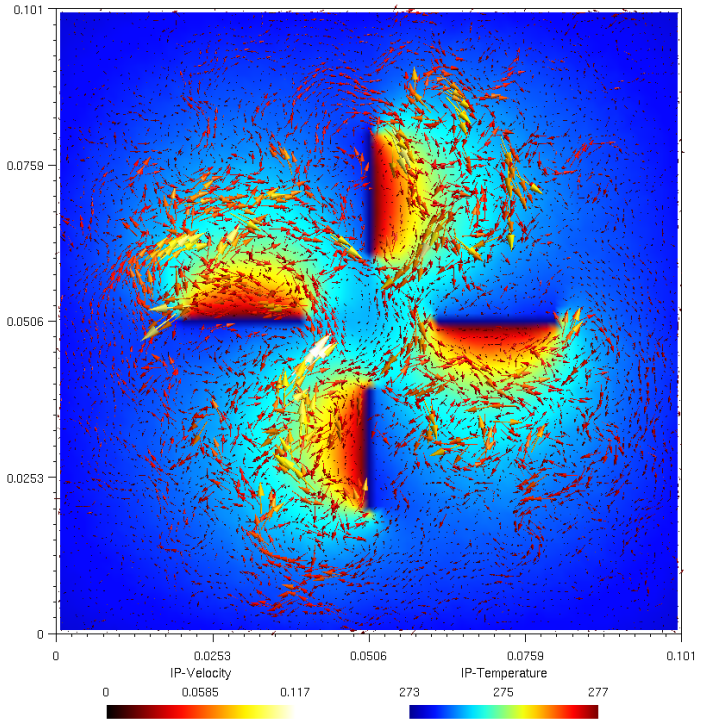

6-7(a): Velocity and Temperature Distributions

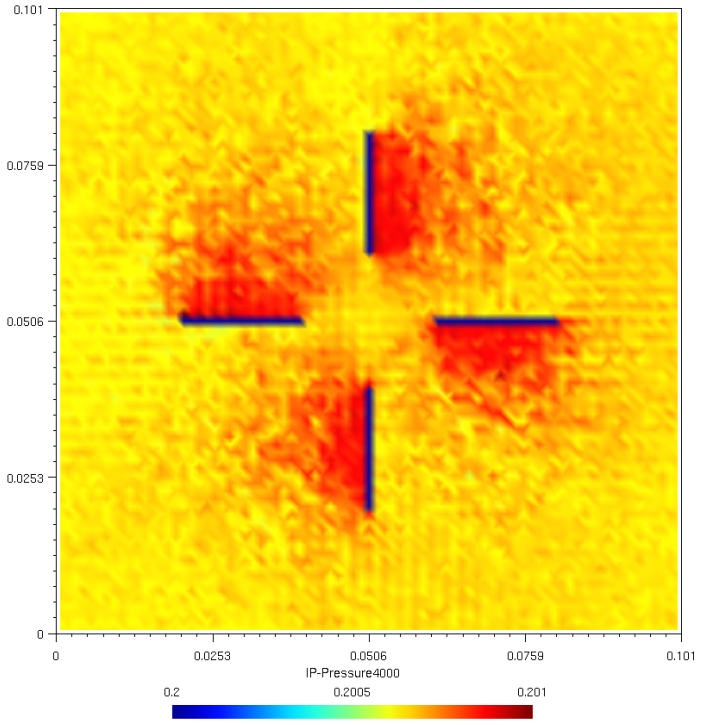

6-7(b): Pressure Distribution

Figure 6-7: Radiometer Simulation with 20 mm vanes and 7 K temperature difference

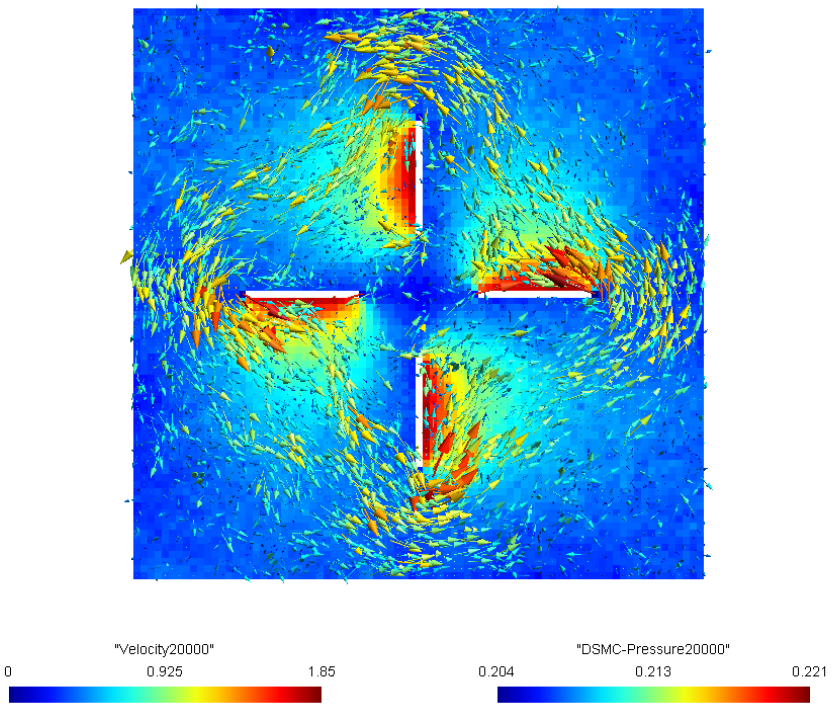

6-8(a): DSMC velocity distribution

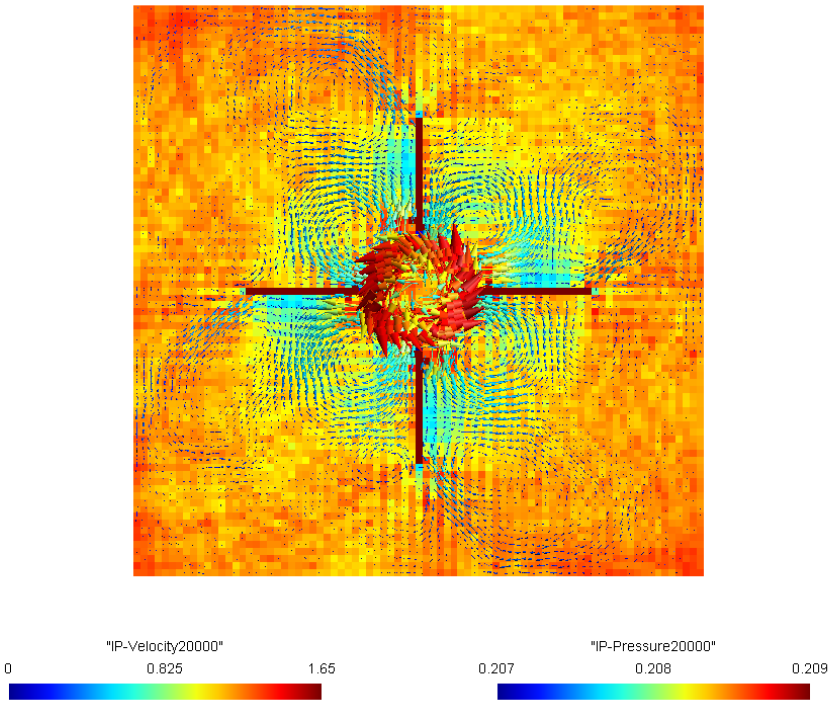

6-8(b): OSIP-DSMC velocity distribution

Figure 6-8: Radiometer simulation with 100 K temperature difference

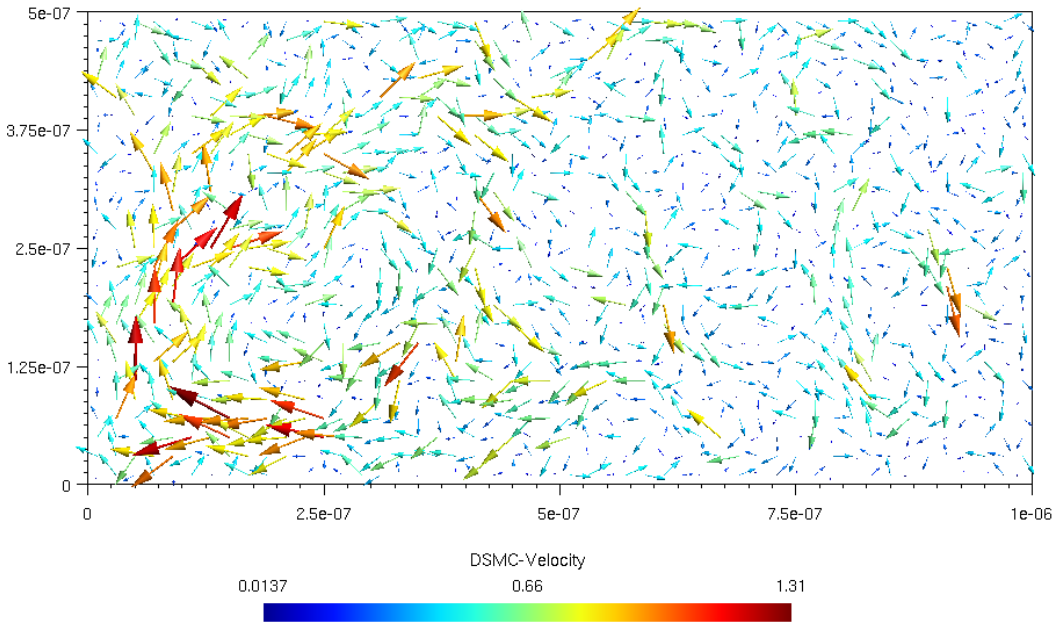

6-9(a): DSMC Velocity 1 atm

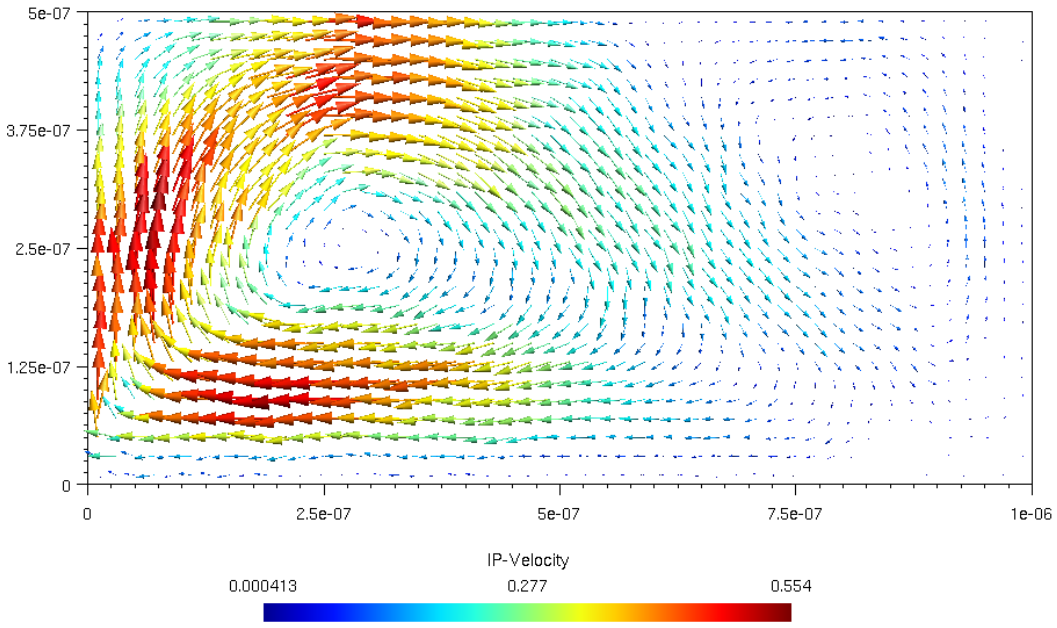

6-9(b): OSIP-DSMC Velocity 1 atm

Figure 6-9: Comparison of Velocity Fields for Thermal Cavities (1 µm × 1 µm, $T_1 = 400$ K and $T_2 = 200$ K)

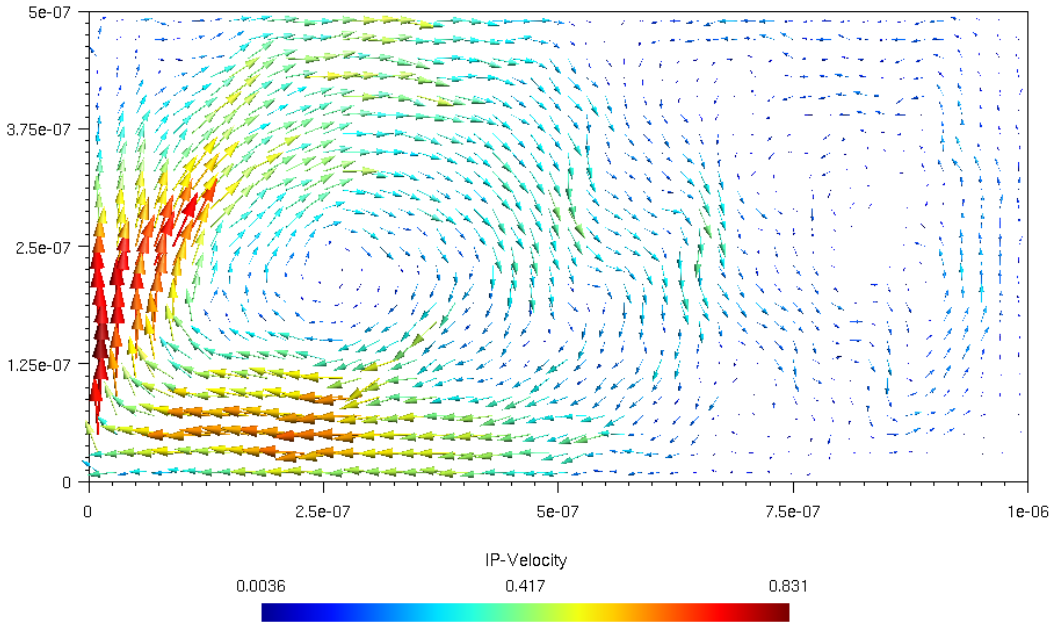

Figure 6-10: Velocity Fields for Thermal Cavities (1 μm × 1 μm, T_1 = 400 K and T_2 = 200 K, 0.1 atm.)

DSMC, as well as some weaknesses that will need to be addressed in the OSIP-DSMC. The OSIP-DSMC remains a significant advancement in the modeling of rarefied gases, as it efficiently models many low-speed flows while retaining certain flow characteristics lost by other methods.

CHAPTER VII

SUMMARY AND CONCLUSIONS

7.1 Summary

The continued progression toward the development of increasingly smaller micro- and nanoscale systems requires accurate and efficient modeling techniques. This is complicated by the effect of scaling, as physical phenomena may manifest differently or with different importance at various length scales. The kinetic theory of gas dynamics is useful in describing the behavior of rarefied flows, as may be present in macroscale flows at low pressures and micro- and nanoscale flows at moderate pressures. However, numerical methods, such as the DSMC, that are suitable for modeling general rarefied flow conditions and geometries tend to be computationally intensive. The main objective of this study was to develop efficient numerical modeling techniques for thermally driven rarefied gas phase flows. Initially the intended focus was to implement existing methods, as reported in the literature, and explore coupling techniques to develop suitable multiscale methods for thermally driven flows.

The IP-DSMC was an attractive method for modeling subcontinuum flows, as it greatly reduces the statistical scatter that complicates DSMC modeling of low-speed flows. However, upon implementing the method, it became apparent that it was inadequate for the desired goals of this research. The focus of this study shifted to enhancing the IP-DSMC and has resulted in the formal derivation of the Octant Splitting IP-DSMC. The prior state-of-the-art Flux Splitting IP-DSMC method of Sun and Boyd [101] provided a formal basis for the treatment of fluxal transport, or correlation coefficients. Information Preserving DSMC methods seek to reduce statistical scatter by preserving macroscopic quantities associated

with the underlying behavior of the real gas, particularly velocity components and temperature. As such, the preserved velocities tend to be smoothed, with much of the random kinetic energy converted to preserved thermal energy. Velocity modalities, as may arise in many non-equilibrium flows, are thus destroyed by the method, although temperature modalities may remain. The Flux Splitting correlation coefficients do capture the effect of the thermal energy on the normal components of momentum (as a pressure effect), but are incapable of extracting shear components. Thus information regarding shear components of momentum in a modal system tend to be converted to thermal energy and are lost with regards to momentum transport.

The Octant Splitting Method provides a means of recapturing normal and shear components of momentum from a non-equilibrium flow. Furthermore, with the correct choice of natural coordinates, it appears to be an accurate and efficient method suitable for modeling general geometries and flows. The theoretical basis of the method is enhanced by the fact that it degenerates gracefully to recover lower order Quadrant Splitting, Flux Splitting, and Local Thermal Equilibrium methods, either by choice of the analyst or naturally in response to the current flow conditions. This allows the method to operate seamlessly over a wide range of flow conditions, equilibrium and non-equilibrium. The method has been applied to a number of non-equilibrium thermally driven flows, including: thermal transpiration, thermal discontinuities, Knudsen force cantilever, and the Crookes radiometer.

Preliminary studies early in this research led to the development of a kinetic theory based macromodel. This model was applied to the TSAFM system and used to map out the operational space of two TSAFM designs. This work confirmed the suspicion that subcontinuum heat transfer significant affects on the behavior of TSAFM systems, and should be included in future design and analysis efforts. Once the OSIP-DSMC was complete, a coupled BEM/OSIP-DSMC model of a 2D TSAFM cantilever cross section was constructed using the Alternating Schwarz coupling method. The results of this simulation provide insight into the magnitude of the Knudsen force effect on the TSAFM system and uncovered

a flaw in the macromodel that was readily fixed. This correction allows the macromodel to provide a very good approximation of the total heat transfer, without the expense of the full 2D coupled simulation.

7.2 Impact

The investigation of efficient numerical methods has led to a number of significant contributions which include:

- First and foremost, the careful derivation and implementation of the Octant Splitting IP-DSMC is the most significant contribution. This method enables the simulating a variety of flow conditions, but most notably low-speed thermally driven flows
- The derivation of improved theory-based sampling techniques for the stress tensor and heat flux that are consistent with the kinetic theory and the numerical method to provide a full set of preserved macroscopic quantities.
- The development of an efficient macromodel that is valid over the entire Knudsen range describing the heat transfer from a heated cantilever to a surface and the surrounding atmosphere.
- The development of a multiscale simulation technique coupling the new OSIP-DSMC and a BEM solver, which appears to be the first use of the BEM in a multiscale rarefied gas simulation technique.
- An investigation of TSAFM operation including: system and sensitivity characterization that accounts for subcontinuum heat transfer and a detailed 2D multiscale model based on the OSIP-DSMC that provides insight into the effect of the thermal flows induced by the TSAFM operation

7.3 Recommendations for Future Work

The work in the present study should be extended through additional research to address a number of limitations and to explore further enhancements and applications:

- A careful study of all aspects of the OSIP-DSMC method should be undertaken to identify formal criteria for aspects that remain *ad hoc* including: the collision model, weighting of correlation coefficients, and treatment of boundary conditions in the IP updates

- The OSIP-DSMC should be extended to include other gas species and mixtures. Currently the OSIP-DSMC has only been used to model Argon, although it should be extensible to other gas species and even mixtures

- Additional simulations should be performed to further validate the method, in particular to identify the cause of the non-physical behavior observed in the radiometer simulations

- A thorough study of the Knudsen force should be performed, evaluating the effects of ambient pressure, temperature difference, beam geometry, and gap height. This will be of use to a large number of researchers involved MEMS and Scanning Probe Microscopy technologies.

- As a practical measure, the GT-DSMC code base should be updated to include the ability to use non-uniform, non-structured meshes, as this would allow greater flexibility in modeling

- The issues affecting stability should be explored mathematically and practically to provide guidelines and stability criteria for the method, and perhaps further improvements

REFERENCES

[1] Aktas, O. and Aluru, N. R., "A combined continuum/DSMC technique for multiscale analysis of microfluidic filters," *Journal of Computational Physics*, vol. 178, pp. 342–372, 2002.

[2] Aktas, O., Aluru, N. R., and Ravaioli, U., "Application of a parallel DSMC technique to predict flow characteristics in microfluidic filters," *Journal of MicroElectroMechanical Systems*, vol. 10, no. 4, pp. 538–549, 2001.

[3] Alexander, F., Garcia, A., and Alder, B., "Direct simulation Monte Carlo for thin-film bearings," *Physics of Fluids*, vol. 6, no. 12, pp. 3854–3860, 1994.

[4] Alexeenko, A. A., Gimelshein, S. F., Muntz, E. P., and Ketsdever, A. D., "Modeling of thermal transpiration flows for Knudsen compressor optimization," in *43rd AIAA Aerospace Sciences Meeting and Exhibit*, (Reno, Nevada), 2005.

[5] Annis, B. K., "Thermal creep in gases," *Journal of Chemical Physics*, vol. 57, no. 7, pp. 2898–2905, 1972.

[6] Aoki, K., Sone, Y., and Waniguchi, Y., "A rarefied gas flow induced by a temperature field: Numerical analysis of the flow between two coaxial elliptic cylinders with different uniform temperatures," *Computers and Mathematics with Applications*, vol. 35, no. 1/2, pp. 15–28, 1998.

[7] Aoki, K., Takata, S., Hidefumi, A., and Golse, F., "A rarefied gas flow caused by a discontinuous wall temperature," *Physics of Fluids*, vol. 13, no. 9, pp. 2645–2661, 2001.

[8] Ashegi, M., King, W. P., Chui, B. W., Kenny, T. W., and Goodson, K. E. in *Proceedings of Transducers '99 Technical Digest*, vol. 1, p. 1840, 1999.

[9] Babovsky, H. and Illner, R., "A convergence proof for Nanbu's simulation method for the full boltzmann equation," *SIAM Journal on Numerical Analysis*, vol. 26, pp. 45–65.

[10] Banerjee, P. K., *The Boundary Element Methods in Engineering*. London: McGraw-Hill, 1994.

[11] Bennet, M. J. and Tompkins, F. C., "Thermal transpiration: Application of liang's equation," *Transactions of the Farraday Society*, vol. 53, pp. 185–192, 1957.

[12] Bhatnagar, P. L., Gross, E. P., and Krook, M., "A model for collision processes in gases. i. small amplitude processes in charged and neutral one-component systems," *Physical Review*, vol. 94, no. 3, pp. 511–525, 1954.

[13] Binnig, G., Despont, M., Drechsler, U., Haberle, W., Lutwyche, M., Vettiger, P., Mamin, H. J., Chui, B. W., and Kenny, T. W., "Ultrahigh-density atomic force microscopy data storage with erase capability," *Applied Physics Letters*, vol. 74, no. 9, pp. 1329–1331, 1999.

[14] Binnig, G., Quate, C. F., and Gerber, C., "Atomic force microscope," *Physical Review Letters*, vol. 56, pp. 930–933, 1986.

[15] Binnig, G. and Rohrer, H., "Scanning tunneling microscopy–from birth to adolescence," *Reviews of Modern Physics*, vol. 59, pp. 615–625, 1987.

[16] Bird, G. A., "Approach to translational equilibrium in a rigid sphere gas," *Physics of Fluids*, vol. 6, p. 1518, 1963.

[17] Bird, G. A., *Molecular Gas Dynamics and the Direct Simulation of Gas Flows*. Clarendon Press; Oxford University Press, 1994.

[18] Bird, G. A., "Forty years of DSMC, and now?," in *Rarefied Gas Dynamics: 22nd International Symposium* (Gallis, T. J. B. and A., M., eds.), Rarefied Gas Dynamics, pp. 372–380, American Institute of Physics, 2001.

[19] Borisov, S. and Sazhin, O., "Thermal transpiration phenomenon study by Monte Carlo method with the use of different gas-surface scattering kernels," in *Direct Simulation Monte Carlo: Theory, Methods & Applications*, (Sante Fe, NM), p. 1, 2005.

[20] Bourgat, J.-F., Le Tallec, P., and Tidriri, M., "Coupling boltzmann and Navier-Stokes equations by friction," *Journal of Computational Physics*, vol. 127, no. 2, pp. 227–245, 1996.

[21] Boyd, I. D. and Sun, Q., "Particle simulation of micro-scale gas flows," in *39th AIAA Aerospace Sciences Meeting & Exhibit*, (Reno, NV), pp. A01–16691 1–7, 2001.

[22] Cai, C., Boyd, I. D., Fan, J., and Candler, G. V., "Direct simulation methods for low-speed microchannel flows," *Journal of Thermophysics and Heat Transfer*, vol. 14, no. 3, pp. 368–378, 2000.

[23] Carslaw, H. S. and Jaeger, J. C., *Conduction of heat in solids*. Oxford: Clarendon Press, 2 ed.

[24] Cercignani, C., *The Boltzmann Equation and Its Applications*. New York: Springer-Verlag, 1988.

[25] Chan, W. K. and Sun, Y., "Analytical modeling of ultra-thin-film bearings," *Journal of Micromechanics and Microengineering*, vol. 13, pp. 463–473, 2003.

[26] Chui, Benjamin, W., Asheghi, M., Ju, Y. S., Goodson, K. E., Kenny, T. W., and Mamin, H. J., "Intrinsic-carrier thermal runaway in silicon microcantilevers," *Microscale Thermophysical Engineering*, vol. 3, pp. 217–224, 1999.

[27] Chui, Benjamin, W., Stowe, T. D., Ju, Y. S., Goodson, K. E., Kenny, T. W., Mamin, H. J., Terris, B. D., Ried, R. P., and Rugar, D., "Low-stiffness silicon cantilevers with integrated heaters and piezoresistive sensors for high-density afm thermomechanical data storage," *Journal of MicroElectroMechanical Systems*, vol. 7, no. 1, pp. 69–78, 1998.

[28] Delgado-Buscalioni, R. and Coveney, P. V., "Continuum-particle hybrid coupling for mass, momentum, and energy transfers in unsteady fluid flow," *Physical Review E*, vol. 67, pp. 046704–1–13, 2003.

[29] Denpoh, K., "Modeling of rarefied gas heat conductions between wafer and susceptor," *IEEE Transactions on Semiconductor Manufacturing*, vol. 11, no. 1, pp. 25–29, 1998.

[30] E, W. and Engquist, B., "The heterogeneous multiscale methods," *Comm. Math Sci.*, vol. 1, no. 1, pp. 87–132, 2003.

[31] Fan, J. and Shen, C., "Statistical simulation of low-speed unidirectional flows in transition regime," in *Proceedings of the 21th International Symposium on Rarefied Gas Dynamics* (Brum, R. e. a., ed.), (Marseille, France), pp. 245–252, 1999.

[32] Fan, J. and Shen, C., "Statistical simulation of low-speed rarefied gas flows," *Journal of Computational Physics*, vol. 167, pp. 393–412, 2001.

[33] Fan, Q., Xue, H., and Shu, C., "DSMC simulations of gaseous flows in microchannels," in *5th ASME/JSME Joint Thermal Engineering Conference*, vol. AJTE99-6519, (San Diego, California), pp. 1–7, 1999.

[34] Flekkoy, E. G., Wagner, G., and Feder, J., "Hybrid model for combined particle and continuum dynamics," *Europhysics Letters*, vol. 52, no. 3, pp. 271–276, 2000.

[35] Frechette, L. G., Jacobson, S. A., Breuer, K. S., Ehrich, F. F., Ghodssi, R., Khanna, R., Chee, W. W., Xin, Z., Schmidt, M. A., and Epstein, A. H., "High-speed microfabricated silicon turbomachinery and fluid film bearings," *Journal of MicroElectroMechanical Systems*, vol. 14, no. 1, pp. 141–152, 2005.

[36] Fu, C. J. and Zhang, Z. M., "Nanoscale radiative heat transfer for silicon at different doping levels," *International Journal of Heat and Mass Transfer*, vol. 49, pp. 1703–1718, 2006.

[37] Garcia, A. L., "Generation of the chapman-enskog distribution," *Journal of Computational Physics*, vol. 140, pp. 66–70, 1998.

[38] Garcia, A. L., Bell, J. B., Crutchfield, W. Y., and Alder, B. J., "Adaptive mesh and algorithm refinement using direct simulation Monte Carlo," *Journal of Computational Physics*, vol. 154, pp. 134–155, 1999.

[39] Garcia, A. L. and Wagner, W., "The limiting kinetic equation of the consistent boltzmann algorithm for dense gases," *Journal of Statistical Physics*, vol. 101, pp. 1065–1086, 2000.

[40] Gombosi, T. I., *Gaskinetic Theory*. Cambridge University Press, 1994.

[41] Hadjiconstantinou, N. and Simek, O., "Constant-wall-temperature Nusselt number in micro and nano-channels," *Transactions of the ASME. Journal of Heat Transfer*, vol. 124, no. 2, pp. 356–64, 2002.

[42] Hadjiconstantinou, N. G., "Comments on Cercignani's second-order slip coefficient," *Physics of Fluids*, vol. 15, no. 8, pp. 2352–2354, 2003.

[43] Hadjiconstantinou, N. G. and Garcia, A. L., "Statistical error in particle simulations of low mach number flows," in *First MIT Conference on Computational Fluid and Solid Mechanics*, pp. 853–856, Elsevier, 2001.

[44] Harley, J. A. and Kenny, T. W., "High-sensitivity piezoresistive cantilevers under 1000 Angstrom thick," *Applied Physics Letters*, vol. 75, pp. 289–291, 1999.

[45] Hash, D. B. and Hassan, H. A., "Assessment of schemes for coupling Monte Carlo and Navier-Stokes solution methods," *Journal of Thermophysics and Heat Transfer*, vol. 10, no. 2, pp. 242–249, 1996.

[46] IBM Reseach, Zurich, "milli_SEM.tif." Accessed June 20, 2006. Available from `http://domino.research.ibm.com/comm/pr.nsf/pages/rsc.millipede.html`.

[47] Incropera, F. P. and DeWitt, D. P., *Fundamentals of Heat and Mass Transfer*. Wiley, 4th ed., 1996.

[48] Jaeger, R. C., *Introduction to Microelectronic Fabrication*. Upper Saddle River, NJ: Prentice Hall, 2 ed.

[49] Karniadakis, G. E. and Beskok, A., *Microflows*. Springer Verlag, second ed., 2001.

[50] Kennard, E. H., *Kinetic Theory of Gases, With an Introduction to Statistical Mechanics*. McGraw-Hill, 1st ed., 1938.

[51] Kevrekidis, I. G., Gear, C. W., Hyman, J. M., Kevrekidis, P. G., Runborg, O., and Theodoropoulos, C., "Equation-free, coarse-grained multiscale computation: enabling microscopic simulators to perform system-level analysis," *Communications in Mathematical Sciences*, vol. 1, no. 4, pp. 715–762, 2003.

[52] King, W. P., Kenny, T. W., Goodson, K. E., Cross, G. L. W., Despont, M., Durig, U., Rothuizen, H., Binnig, G., and Vettiger, P., "Design of atomic force microscope cantilevers for combined thermomechanical writing and reading in array operation," *Journal of Microelectromechanical Systems*, vol. 11, pp. 765–774, 2002.

[53] King, W. P., Kenny, T. W., and Goodson, K. E., "Comparison of piezoresistive and thermal detection approaches to atomic force microscopy topography measurement," in *IMECE 2002*, (IMECE2002-33295), pp. 1–6, ASME, 2002.

[54] Kittel, C., *Introduction to Solid State Physics*. New York: Wiley, 7th ed., 1996.

[55] Kogan, M., Galkin, V., and Fridlender, O., "Stresses produced in gasses by temperature and concentration inhomogeneities. new types of free convection," *Soviet Physics Uspekhi*, vol. 19, pp. 420–438, 1976.

[56] Koura, K. and Matsumoto, H., "Variable soft sphere molecular model for air species," *Physics of Fluids A (Fluid Dynamics)*, vol. 4, no. 5, p. 1083, 1992.

[57] Le Tallec, P. and Mallinger, F., "Coupling boltzmann and Navier-Stokes equations by half fluxes," *Journal of Computational Physics*, vol. 136, no. 1, pp. 51–67, 1997.

[58] Leonard, B. P., "A stable and accurate convective modeling procedure based on quadratic upstream interpolation," *Computer Methods in Applied Mechanics and Engineering*, vol. 19, no. 1, pp. 58–98.

[59] Lereu, A. L., Passian, A., Warmack, R. J., Ferrell, T. L., and Thundat, T., "Effect of thermal variations on the Knudsen forces in the transitional regime," *Applied Physics Letters*, vol. 84, no. 6, pp. 1013–1015, 2004.

[60] Lien, F. S. and Leschziner, M. A., "Upstream monotonic interpolation for scalar transport with application in complex turbulent flows," *International Journal of Numerical Methods in Fluids*, vol. 19, no. 6, pp. 527–548, 1994.

[61] Loeb, *Rarefied Gas Dynamics*. Dover Classics, 1937.

[62] Lu, Z., "Experimental and numerical study of the optimal operation pressure within Crookes radiometer," *Journal of Vacuum Science and Technology A*, vol. 23, no. 6, pp. 1531–1534, 2005.

[63] Luo, L.-S., "Theory of the lattice Boltzmann method: Lattice Boltzmann models for nonideal gases," *Physical Review E*, vol. 62, no. 4, pp. 4982–4996, 2000.

[64] Majumdar, A., "Scanning thermal microscopy," *Annual Review of Material Science*, vol. 29, pp. 505–585, 1999.

[65] Martin, Y., Williams, C. C., and Wickramasinghe, H. K., "Atomic force microscope–force mapping and profiling on a sub 100-Angstrom scale.," *Journal of Applied Physics*, vol. 61, pp. 4723–4729, 1987.

[66] Masters, N. D., Ye, W., and King, W. P., "Improved modeling of non-continuum heat transfer during topographical imaging with a heated atomic force microscope cantilver," in *IMECE '04*, (Anaheim, California), ASME, 2004.

[67] Masters, N. D., Ye, W., and King, W. P., "The impact of subcontinuum gas conduction on topography measurement sensitivity using heated atomic force microscope cantilevers," *Physics of Fluids*, vol. 17, no. 100615, pp. 1–8, 2005.

[68] Matsumoto, M. and Nishimura, T., "Mersenne twister: a 623-dimensionally equidistributed uniform pseudo-random number generator," *ACM Transactions on Modeling and Computer Simulation*, vol. 8, no. 1, pp. 3–30, 1998.

[69] McNamara, S. and Gianchandani, Y. B., "On-chip vacuum generated by a micromachined Knudsen pump," *Journal of MicroElectroMechanical Systems*, vol. 14, no. 4, pp. 741–746, 2005.

[70] Mulet, J.-P., Joulain, K., Carminati, R., and Greffet, J.-J., "Enhanced radiative heat transfer at nanometric distances," *Microscale Thermophysical Engineering*, vol. 6, pp. 209–222, 2002.

[71] Müller, M. and Herrmann, H. J., "DSMC – a stochastic algorithm for granular matter," *Physics of Dry Granular Media*, 1998.

[72] Nabors, K. and White, J., "Fastcap: a multipole accelerated 3-d capacitance extraction program," *IEEE Transactions on Computer-Aided Design of Integrated Circuits and Systems*, vol. 10, no. 11, pp. 1447–1459, 1991.

[73] Nanbu, K., "Direct simulation scheme derived from the boltzmann equation. i. multicomponent gases," *Journal of The Physical Society of Japan*, vol. 45, pp. 2042–2049.

[74] Nance, R. P., Hash, D. B., and Hassan, H. A., "Role of boundary conditions in Monte Carlo simulations of microelectromechanical systems," *Journal of Thermophysics and Heat Transfer*, vol. 12, no. 3, pp. 447–449, 1998.

[75] Nishizawa, S. and Hirata, M., "DSMC analysis of thermal transpiration of capacitance diaphragm gauge," *Vacuum 7th European Vacuum Meeting/3rd European Topical Conference on Hard Coatings, 17-20 Sept. 2001*, vol. 67, no. 3-4, pp. 301–306, 2001.

[76] Ochoa, F., Eastwood, C., Ronney, P., and Dunn, B., "Thermal transpiration based microscale propulsion and power generation devices," in *7th International Microgravity Combustion Workshop*, (Cleveland, OH), p. 4, 2003.

[77] O'Connell, S. T. and Thompson, P. A., "Molecular dynamics-continuum hybrid computations: A tool for studying complex fluid flows," *Physical Review E*, vol. 52, pp. 5792–5795, 1995.

[78] Ohsawa, T. and Ohwada, T., "Deterministic hybrid computation of rarefied gas flows," in *Rarefied Gas Dynamics International Symposium* (Ketsdever, A. D. and Muntz, E. P., eds.), pp. 931–938, 2003.

[79] Ohwada, T., Sone, Y., and Aoki, K., "Numerical analysis of the posielle and thermal transpiration between tho parallel plates on the basis of the boltzman equation for hard-sphere molecules," *Physics of Fluids A (Fluid Dynamics)*, vol. 1, no. 12, pp. 2042–2049, 1989.

[80] Oran, E. S., Oh, C. K., and Cybyk, B. Z., "Direct simulation Monte Carlo: Recent advances and applications," *Annual Review of Fluid Mechanics*, vol. 30, pp. 403–441, 1998.

[81] Ota, M., Nakao, T., and Sakamoto, M., "Numerical simulation of molecular motion around laser microengine blades," *Mathematics and Computers in Simulation*, vol. 55, pp. 223–230, 2001.

[82] Pan, L. S., Liu, G. R., Khoo, B. C., and Song, B., "A modified direct simulation Monte Carlo method for low-speed microflows," *Journal of Micromechanics and Microengineering*, vol. 10, pp. 21–27, 2000.

[83] Pan, L. S., Ng, T. Y., Xu, D., and Lam, K. Y., "Molecular block model direct simulation Monte Carlo method for low velocity microgas flows," *Journal of Micromechanics and Microengineering*, vol. 11, pp. 181–188, 2001.

[84] Passian, A., Warmack, R. J., Ferrell, T. L., and Thundat, T., "Thermal transpiration at the microscale: A Crookes cantilever," *Physical Review Letters*, vol. 90, no. 12, pp. 124503–1–4, 2003.

[85] Passian, A., Warmack, R. J., Wig, A., Farahi, R. H., Meriaudeau, F., Ferrell, T. L., and Thundat, T., "Observation of Knudsen effect with microcantilevers," *Ultramicroscopy*, vol. 97, pp. 401–406, 2003.

[86] Passian, A., Wig, A., Meriaudeau, F., Ferrell, T. L., and Thundat, T., "Knudsen forces on microcantilevers," *Journal of Applied Physics*, vol. 92, no. 10, pp. 6326–6333, 2002.

[87] Phillips, J. and White, J., "A precorrected-FFT method for electrostatic analysis of complicated 3-D structures," *IEEE Transactions on Computer-Aided Design of Integrated Circuits and Systems*, vol. 16, no. 10, pp. 1059–1072, 1997.

[88] Piekos, E. S. and Breuer, K. S., "Numerical modeling of micromechanical devices using the direct simulation Monte Carlo method," *Journal of Fluids Engineering, Transactions of the ASME*, vol. 118, no. 3, pp. 464–468, 1996.

[89] Rudd, R. E. and Broughton, J. Q., "Concurrent coupling of length scales in solid state systems," *Physica Status Solidi B*, vol. 217, no. 1, pp. 251–91, 2000.

[90] Scandurra, M., "Enhanced radiometric forces," *ArXiv Physics e-prints*, Feb. 2004.

[91] Sharipov, F., "Rarefied gas flow through a long tube at any temperature ratio," *Journal of Vacuum Science and Technology A*, vol. 14, no. 4, pp. 2627–2635, 1996.

[92] Sharipov, F., "Non-isothermal gas flow through rectangular microchannels," *Journal of Micromechanics and Microengineering*, vol. 9, no. 4, pp. 394–401, 1999.

[93] Sharipov, F. and Seleznev, V., "Data on internal rarefied gas flows," *Journal of Chemical Reference Data*, vol. 27, no. 3, pp. 657–706, 1998.

[94] Shen, C., Jiang, J. Z., and Fan, J., "Information preservation method for the case of temperature variation," in *Rarefied Gas Dynamics: 22nd International Symposium* (Bartel, T. J. and Gallis, M. A., eds.), pp. 185–192, American Institute of Physics, 2001.

[95] Shenoy, V. B., Miller, R., Tadmor, E. B., Phillips, R., and Ortiz, M., "Quasicontinuum models of interfacial structure and deformation," *Physical Review Letters*, vol. 80, no. 4, pp. 742–745, 1998.

[96] Shi, F., Ramesh, P., and Mukherjee, S., "On the application of 2D potential theory to electrostatic simulation," *Communications in Numerical Methods in Engineering*, vol. 11, pp. 691–701, 1995.

[97] Sone, Y. and Yoshimoto, M., "Demonstration of a rarefied gas flow induced near the edge of a uniformly heated plate," *Physics of Fluids*, vol. 9, no. 11, pp. 3530–3534, 1997.

[98] Sone, Y., "Flows induced by temperature fields in a rarefied gas and their ghost effect on the behavior of a gas in the continuum limit," *Annual Review of Fluid Mechanics*, vol. 32, pp. 779–811, 2000.

[99] Sun, Q., *Information Preservation Methods for Modeling Micro-Scale Gas Flows*. Ph.d., University of Michigan, 2003.

[100] Sun, Q. and Boyd, I. D., "A direct simulation method for subsonic microscale gas flows," *Journal of Computational Physics*, vol. 179, pp. 400–425, 2002.

[101] Sun, Q. and Boyd, I. D., "Theoretical development of the information preserving method for strongly nonequilibrium gas flows," in *38th AIAA Thermophysics Conference*, (Toronto, Ontario, Canada), pp. AIAA–2005–4828 1–10, AIAA, 2005.

[102] Sun, Q., Boyd, I. D., and Candler, G. V., "A hybrid continuum / particle approach for micro-scale gas flows," in *Rarefied Gas Dynamics International Symposium* (Ketsdever, A. D. and Muntz, E. P., eds.), pp. 752–759, American Institute of Physics, 2003.

[103] Vargo, S. E., Muntz, E. P., Shiflett, G. R., and Tang, W. C., "Knudsen compressor as a micro- and macroscale vacuum pump without moving parts or fluids," *Journal of Vacuum Science and Technology A*, vol. 17, no. 4, pp. 2308–2313, 1999.

[104] Vargo, S. E. and Muntz, E. P., "Initial results from the first mems fabricated thermal transpiration-driven vacuum pump," in *Rarefied Gas Dynamics: 22nd International Symposium* (Bartel, T. J. and Gallis, M. A., eds.), pp. 502–509, American Institute of Physics, 2001.

[105] Vettiger, P., Cross, G., Despont, M., Drechsler, U., Dürig, U., Gotsmann, B., Häberle, W., Lantz, M., Rothuizen, H., Stutz, R., and Binnig, G., "The "millipede"—nanotechnology entering data storage," *IEEE Transactions on Nanotechnology*, vol. 1, no. 1, pp. 39–55, 2002.

[106] Vettiger, P., Despont, M., Drechsler, U., Dürig, U., Häberle, W., Lutwyche, M. I., Rothuizen, H., Stutz, R., Widmer, R., and Binnig, G. K., "The 'millipede'–more than one thousand tips for future afm data storage," *IBM Journal of Research and Development*, vol. 44, no. 3, pp. 323–340, 2000.

[107] Wang, W.-L. and Boyd, I. D., "Hybrid dsmc-cfd simulations of hypersonic flow over sharp and blunted bodies," in *36th AIAA Thermophysics Conference*, (Orlando, FL), pp. AIAA 2003–3644 1–13, American Institute of Aeronautics and Astronautics, 2003.

[108] Wang, W.-L. and Boyd, I. D., "A new energy flux model in the DSMC-IP method for nonequilibrium flows," in *36th AIAA Thermophysics Conference*, (Orlando, Florida), pp. AIAA 2003–3774 1–8, AIAA, 2003.

[109] Welander, P., "On the temperature jump in a rarefied gas," *Arkiv för Fysik*, vol. 7, pp. 507–553, 1954.

[110] Wijesinghe, H. S. and Hadjiconstantinou, N. G., "A hybrid continuum-atomistic scheme for viscous, incompressible gaseous flow," in *Rarefied Gas Dynamics International Symposium* (Ketsdever, A. D. and Muntz, E. P., eds.), pp. 907–914, American Institute of Physics, 2003.

[111] Wijesinghe, H. S., Hornung, R., Garcia, A. L., and Hadjiconstantinou, N. G., "Three-dimensional hybrid continuum-atomistic simulations for multiscale hydrodynamics," *Journal of Fluids Engineering*, vol. in review, 2004.

[112] Wijesinghe, H. S. and Hadjiconstantinou, N. G., "A discussion of hybrid atomistic-continuum methods for multiscale hydrodynamics," *International Journal for Multscale Computational Engineering*, vol. in review, 2004.

[113] Wilder, K., Quate, C. F., Adderton, D., Bernstein, R., and Elings, V., "Noncontact nanolithography using the atomic force microscope," *Applied Physics Letters*, vol. 73, pp. 2527–2529, 1998.

[114] Wu, J.-S., Lee, F., and Wong, S.-C., "Pressure boundary treatment in micromechanical devices using the direct simulation Monte Carlo method," *JSME International Series B*, vol. 44, no. 3, pp. 439–450, 2001.

[115] Wu, J.-S., Lee, W.-S., Lee, F., and Wong, S.-C., "Pressure boundary treatment in internal gas flows at subsonic speed using the DSMC method," in *Rarefied Gas Dynamics: 22nd International Symposium* (Bartel, T. J. and Gallis, M. A., eds.), pp. 408–406, American Institute of Physics, 2001.

[116] Wu, J.-S. and Tseng, K.-C., "Analysis of micro-scale gas flows with pressure boundaries using direct simulation Monte Carlo method," *Computers & Fluids*, vol. 30, no. 6, pp. 711–35, 2001.

[117] Zhigilei, L. V., "Computational model for multiscale simulation of laser ablation," in *Material Research Society Symposium*, vol. 677, pp. AA2.1.1–11, 2001.

[118] Zhigilei, L. V. and Dongare, A. M., "Multiscale modeling of laser ablation: Applications to nanotechnology," *CMES*, vol. 3, no. 5, pp. 539–555, 2002.

VITA

Nathan D. Masters was born on March 5, 1973 in Flagstaff, Arizona. He was raised in West Jordan, UT. After graduating from High School, he began his undergraduate studies in Mechanical Engineering at Brigham Young University. After one year of studies he left school to serve a two year mission for his church in Bordeaux, France. Nathan's undergraduate studies resumed at BYU in 1994 resulting in a Bachelor's of Science degree in 1998. He stayed at BYU for graduate work with Dr. Larry L. Howell investigating MEMS and microscale compliant mechanisms. During his Master's studies he was named an Honorable Mention for the National Science Foundation Graduate Research Fellowship and was offered and accepted a one year contractor position at Sandia National Laboratories doing MEMS design and analysis. Returning to BYU in 2000, he finished his Master's of Science degree in 2001. Immediately thereafter, Nathan began his Ph.D. studies at Georgia Institute of Technology.